A model of electroweakly interacting non-abelian vector dark matter

(電弱相互作用を行うベクトル暗黒物質模型の構築)

Kohei Matsushita
松下　康平

Theoretical Elementary Particle Physics Group,
Department of Physics, Nagoya University

February 8, 2021

Abstract

We propose an electroweakly interacting spin-1 dark matter (DM) model. The electroweak gauge symmetry, $\mathrm{SU}(2)_L \times \mathrm{U}(1)_Y$, is extended into $\mathrm{SU}(2)_0 \times \mathrm{SU}(2)_1 \times \mathrm{SU}(2)_2 \times \mathrm{U}(1)_Y$. A discrete symmetry exchanging $\mathrm{SU}(2)_0$ and $\mathrm{SU}(2)_2$ is imposed. This discrete symmetry stabilizes the DM candidate. The spin-1 DM particle (V^0) and its $\mathrm{SU}(2)_L$ partners ($V^\pm$) interact with the Standard Model (SM) electroweak gauge bosons without any suppression factors. Consequently, pairs of DM particles efficiently annihilate into the SM particles in the early universe, and the measured value of the DM energy density is easily realized by the thermal freeze-out mechanism. The model also predicts a heavy vector triplet ($W'^\pm$ and Z') in the visible sector. They contribute to the DM annihilation processes. The mass ratio of Z' and V^0 determines values of various couplings, and constraints on W' and Z' restrict regions of the parameter space that are viable for DM physics. We investigate the constraints from perturbative unitarity of scalar and gauge couplings, the Higgs signal strength, W' search at the LHC, DM direct detection experiments, and indirect detection experiments. We found that our DM can explain the right amount of the DM relic abundance for 3 TeV $\lesssim m_{V^0} \lesssim$ 27.5 TeV.

Contents

1 Introduction **4**

2 The Standard Model of particle physics **6**
2.1 SM gauge symmetry and particle contents 6
2.1.1 Electroweak symmetry breaking 8
2.1.2 fermion masses and CKM matrix 11
2.2 Beyond the SM 12
2.2.1 The problems in the SM 12

3 Dark Matter **14**
3.1 Indirect evidence of dark matter 14
3.2 WIMP -thermal freeze-out mechanism- 17
3.3 Relic density 18
3.4 Direct Detection 21
3.5 Indirect Detection 22
3.6 Status of WIMP models 24
3.6.1 Singlet real scalar dark matter 24
3.6.2 EWIMP model 26

4 Model **28**
4.1 Bosonic sector 30
4.2 Gauge sector 31
4.3 Physical scalars 32
4.4 Model parameters 33

5 Constraints **37**
5.1 Perturbative unitarity 37
5.2 The mass ratio of Z' and V 38
5.3 W' and Z' searches at the LHC 40
5.4 Electroweak precision measurements 40
5.5 Higgs signal strength 41

6 DM phenomenology **42**
6.1 Mass difference and its implication for collider physics 42
6.2 Direct detection 43

6.3 Relic abundance . . . 45
6.3.1 heavy h' ($m_{h'} = 1.4 m_V$) . . . 45
6.3.2 light h' ($m_{h'} = 4$ TeV) . . . 47
6.4 Combined results . . . 47
6.4.1 heavy h' ($m_{h'} = 1.4 m_V$) . . . 48
6.4.2 light h' ($m_{h'} = 4$ TeV) . . . 50
6.5 Indirect detection . . . 51
6.5.1 Constraints on $\langle \sigma v \rangle_{\gamma\gamma}$ . . . 52
6.5.2 Prospects on the line cross section . . . 53

7 Conclusions **55**

A our model **58**
A.1 Some details in the gauge sectors . . . 58
A.2 Would-be NG bosons . . . 60
A.3 Fermi constant . . . 61
A.4 $V^- V^+ \to \gamma\gamma$ annihilation cross section . . . 62

Chapter 1

Introduction

Dark matter (DM) is a necessary entity in explaining the results of the various astrophysical observations. We know that DM accounts for about 27% of the total energy in the universe today [1]. However, its true nature is still unknown. Since the Standard Model (SM) of elementary particle physics does not have a candidate for DM, it is necessary to extend the model if we assume that DM is an elementary particle. The Weakly Interacting Massive Particle (WIMP) model has been intensively studied because it can easily explain the amount of DM in the present universe through the thermal freeze-out mechanism [2]. However, the WIMP models are very strongly constrained by direct detection experiments. The latest upper bound on the DM-nucleon scattering cross section is given by the XENON1T experiment [3]. In particular, models in which DM particles are annihilated by the Higgs-mediated or Z boson-mediated interaction can be easily explored in the direct detection experiments and many parameter regions are already restricted.

The electroweakly interacting massive particle (EWIMP) model can evade the constraints by the direct detection experiments since the correct amount of the DM energy density can be explained by the electroweak interaction rather than by the DM-Higgs coupling or the DM-Z coupling. The pure Wino DM, $\mathrm{SU}(2)_L$ triplet fermion in the supersymmetric models is one of the famous EWIMP models [4]. Many EWIMP models for the spin-0 and spin-1/2 DM have been proposed.

In this thesis, we propose a renormalizable model of spin-1 EWIMP that does not require Z and Higgs couplings to a DM particle to obtain the correct amount of the DM density by the freeze-out mechanism.[1] We extend the electroweak gauge symmetry in the SM, $\mathrm{SU}(2)_L \times \mathrm{U}(1)_Y$, into $\mathrm{SU}(2)_0 \times \mathrm{SU}(2)_1 \times \mathrm{SU}(2)_2 \times \mathrm{U}(1)_Y$ and impose that the model is symmetric under exchanging of $\mathrm{SU}(2)_0$ and $\mathrm{SU}(2)_2$. This symmetry predicts a stable $\mathrm{SU}(2)_L$ triplet vector boson, V^0 and $V^\pm$. After the symmetry breaking, the charged vector boson, $V^\pm$, gets slightly heavier than the neutral one, V^0, and thus V^0 is a DM candidate in our model. The vector DM in our model can directly couple to the SM weak gauge bosons and efficiently annihilate in the early universe even without the DM-Higgs coupling. The V^0-V^0-Z coupling is automatically forbidden by the gauge symmetry. Therefore, the model easily evades the constraint from the XENON1T experiment and has a large region of viable parameter space.

[1] Non-renormalizable models for the electroweakly interacting spin-1 DM are discussed in [5, 6].

There are many spin-1 DM models, but they are originated from a U(1) gauge symmetry [7–17] or an SU(2) gauge symmetry that is isolated from the SM electroweak sector [18–27]. Therefore, they rely on the scalar exchanges that require the mixing between the SM Higgs and new scalar particles to obtain the measured value of the DM energy density. The scalar mixing, however, is constrained from the direct detection experiments. On the other hand, our model does not require the scalar mixing for the DM energy density. This is a different feature of our model from the other spin-1 DM models. Another aspect of our model is that new spin-1 particles are predicted in the visible sector as well as the dark sector. Those new spin-1 particles in the visible sector are regarded as W' and Z'. They play an important role in the DM annihilation processes. Moreover, the fermion sector of our model is as simple as in the SM. We do not need to introduce new fermions into the model to obtain the realistic mass spectra for the SM fermions.[2]

We organize the rest of this thesis as follows. First of all, we review the Standard Model of particle physics and dark matter in Chapters. 2 and 3, respectively. In Chapter. 4, we describe our model. Some technical details are discussed in Appendices. In Chapter. 5, we discuss constraints on the model from perturbative unitarity, the mass ratio of Z' and V^0, W' and Z' searches at the LHC, electroweak precision measurements, and the Higgs coupling measurements at the LHC. After constraining the model parameters, we discuss the phenomenology of DM in Chapter. 6. We start by discussing the mass difference between $V^\pm$ and V^0. As discussed later, $V^\pm$ is one of the targets for long-lived particle searches at the LHC. After that, we discuss the thermal relic abundance in this model. We also address the constraint from the direct detection experiment. We show that the viable mass range of V^0 as a thermal relic is 3 TeV $\lesssim m_{V^0} \lesssim$ 27.5 TeV. Finally, we consider the limit from the indirect detection of the γ-ray from the Galactic center of the Milky Way galaxy. This bound looks very stringent, however not believable today because of the uncertainties of the dark matter density profiles. Even so, a large mass region in our model can be searched by the indirect detection experiments. Chapter 7 is devoted to our conclusions.

[2]Non-abelian vector DM with an extended fermion sector are discussed in [28–31].

Chapter 2

The Standard Model of particle physics

The Standard Model (SM) of particle physics includes all discovered elementary particles until today and can explain almost all of the results of various experiments. In this chapter, we briefly review the SM and the reasons why many particle physicists consider the extension of this very successful model.

2.1 SM gauge symmetry and particle contents

The gauge symmetry of the SM is $\mathrm{SU}(3)_C \times \mathrm{SU}(2)_L \times \mathrm{U}(1)_Y$. $\mathrm{SU}(3)_c$ describes the strong interaction. $\mathrm{SU}(2)_L \times \mathrm{U}(1)_Y$ is the electroweak symmetry and spontaneously broken to $\mathrm{U}(1)_{\mathrm{EM}}$. The gauge bosons of the symmetries are G^A_μ, W^a_μ, B_μ, respectively. The other particles of the SM, fermions and the Higgs boson, and their charges under the gauge symmetry are summarized in Table 1 There are three generations of fermions in the SM.

field	spin	$\mathrm{SU}(3)_c$	$\mathrm{SU}(2)_L$	$\mathrm{U}(1)_Y$
q^i_L	$\frac{1}{2}$	3	2	$\frac{1}{6}$
u^i_R	$\frac{1}{2}$	3	1	$\frac{2}{3}$
d^i_R	$\frac{1}{2}$	3	1	$-\frac{1}{3}$
ℓ^i_L	$\frac{1}{2}$	1	2	$-\frac{1}{2}$
e^i_R	$\frac{1}{2}$	1	1	-1
H	0	1	2	$\frac{1}{2}$

Table 1: The matter and Higgs fields and their gauge charges in the SM. i(=1,2,3) is the indices of the generations.

The left-handed fermions are doublets under $\mathrm{SU}(2)_L$,

$$q_L^1 = \begin{pmatrix} u_L \\ d_L \end{pmatrix}, \quad q_L^2 = \begin{pmatrix} c_L \\ s_L \end{pmatrix}, \quad q_L^3 = \begin{pmatrix} t_L \\ b_L \end{pmatrix}, \tag{2.1}$$

$$\ell_L^1 = \begin{pmatrix} \nu_e \\ e_L \end{pmatrix}, \quad \ell_L^2 = \begin{pmatrix} \nu_\mu \\ \mu_L \end{pmatrix}, \quad \ell_L^3 = \begin{pmatrix} \nu_\tau \\ \tau_L \end{pmatrix}. \tag{2.2}$$

However the right-handed fermions are singlets under $\mathrm{SU}(2)_L$.

$$u_R^1 = u_R, \quad u_R^2 = c_R, \quad u_R^3 = t_R, \tag{2.3}$$

$$d_R^1 = d_R, \quad d_R^2 = s_R, \quad d_R^3 = b_R, \tag{2.4}$$

$$e_R^1 = e_R, \quad e_R^2 = \mu_R, \quad e_R^3 = \tau_R. \tag{2.5}$$

The right-handed neutrinos are not included in the SM. The Higgs boson is a doublet under $\mathrm{SU}(2)_L$. The component fields are shown in the next subsection.

The Lagrangian of the SM can be divided into four parts as follows.

$$\mathcal{L} = \mathcal{L}_{\text{gauge}} + \mathcal{L}_{\text{fermion}} + \mathcal{L}_{\text{Higgs}} + \mathcal{L}_{\text{Yukawa}}. \tag{2.6}$$

The gauge part of the SM Lagrangian, $\mathcal{L}_{\text{gauge}}$ contains kinetic terms of $\mathrm{SU}(3)_C$, $\mathrm{SU}(2)_L$ and $\mathrm{U}(1)_Y$ gauge bosons. They are given by

$$\mathcal{L}_{\text{gauge}} = -\sum_{A=1}^{8} \frac{1}{4} G_{\mu\nu}^A G^{A\mu\nu} - \sum_{a=1}^{3} \frac{1}{4} W_{\mu\nu}^a W^{a\mu\nu} - \frac{1}{4} B_{\mu\nu} B^{\mu\nu}. \tag{2.7}$$

where $G_{\mu\nu}^A, W_{\mu\nu}^a$ and $B_{\mu\nu}$ are the field strengths of $\mathrm{SU}(3)_C$, $\mathrm{SU}(2)_L$ and $\mathrm{U}(1)_Y$ gauge bosons, respectively,

$$G_{\mu\nu}^A = \partial_\mu G_\nu^A - \partial_\nu G_\mu^A + g_s f^{ABC} G_\mu^B G_\nu^C, \tag{2.8}$$

$$W_{\mu\nu}^a = \partial_\mu W_\nu^a - \partial_\nu W_\mu^a + g \epsilon^{abc} W_\mu^b W_\nu^c, \tag{2.9}$$

$$B_{\mu\nu} = \partial_\mu B_\nu - \partial_\nu B_\mu. \tag{2.10}$$

f^{ABC} and ϵ^{abc} are the structure constants of $\mathrm{SU}(3)_C$ and $\mathrm{SU}(2)_L$, respectively.

The fermion part, $\mathcal{L}_{\text{fermion}}$, is given by

$$\mathcal{L}_{\text{fermion}} = \sum_{\psi} \bar{\psi} i \not{D} \psi. \tag{2.11}$$

Here the covariant derivative for the particle which has a hyper-charge Y is

$$D_\mu = \partial_\mu - i g_s T_s^A G_\mu^A - i g T^a W_\mu^a - i g_Y Y B_\mu, \tag{2.12}$$

where T_s^A and T^a are $\mathrm{SU}(3)_c$ and $\mathrm{SU}(2)_L$ generators.

The fermion (Dirac) mass terms are prohibited by the gauge symmetries because the left-handed and right-handed particles are charged under the different symmetries. However, after the symmetry breaking, the mass terms come from the Yukawa part,

$$\mathcal{L}_{\text{Yukawa}} = -y_u^{ij} \bar{q}_L^i \tilde{H} u_R^j - y_d^{ij} \bar{q}_L^i H d_R^j - y_e^{ij} \bar{\ell}_L^i H e_R^j + (h.c.). \tag{2.13}$$

Here y_u^{ij}, y_d^{ij} and y_e^{ij} are 3×3 complex matrices, called "Yukawa matirix" and $\tilde{H}$ is defined as

$$\tilde{H} = \epsilon H^*, \quad \epsilon = \begin{pmatrix} 0 & 1 \\ -1 & 0 \end{pmatrix}. \tag{2.14}$$

In the SM, there are no right-handed neutrinos so that we can not write Yukawa interaction terms for them.

The Higgs part, $\mathcal{L}_{\text{Higgs}}$, contains the kinetic term of the Higgs boson and the potential,

$$\mathcal{L}_{\text{Higgs}} = (D_\mu H)^\dagger D^\mu H - V, \tag{2.15}$$

where the Higgs potential, V, is given by

$$V = m^2 H^\dagger H + \lambda (H^\dagger H)^2. \tag{2.16}$$

The 3-point interaction is prohibited because the Higgs boson is a doublet under $\mathrm{SU}(2)_L$. The structure of this potential causes symmetry breaking as we will show the details next subsection.

2.1.1 Electroweak symmetry breaking

The electroweak symmetry, $\mathrm{SU}(2)_L\times\mathrm{U}(1)_Y$, is spontaneously broken by the vacuum expectation value (VEV), v of the Higgs field, H.

$$\langle H \rangle = \begin{pmatrix} 0 \\ \frac{v}{\sqrt{2}} \end{pmatrix}. \tag{2.17}$$

This VEV is related to the Higgs potential parameters with the following stationary condition.

$$m^2 = -\lambda v^2. \tag{2.18}$$

Although both $SU(2)_L$ and $U(1)_Y$ are broken because of this VEV, the mixed U(1) symmetry, $\mathrm{U}(1)_{\text{EM}}$, remains. The unbroken generator, $Q \equiv T^3 + Y$, corresponds to the electric charge of the particle. The Higgs field has four degrees of freedom. Since there is only one unbroken generator, three of them are eaten by gauge bosons, so these are would-be Nambu-Goldstone (NG) bosons, π^0 and $\pi^\pm$. The component fields of the Higgs are given as

$$H = \begin{pmatrix} i\pi^+ \\ \frac{v+h-i\pi^0}{\sqrt{2}} \end{pmatrix}. \tag{2.19}$$

In the unitarity gauge, the NG bosons disappear in the Lagrangian. Hence the Higgs potential is rewritten as

$$V = -\frac{1}{4}\lambda v^4 + \frac{1}{2}(2\lambda v^2)h^2 + \lambda v h^3 + \frac{1}{4}\lambda h^4. \tag{2.20}$$

Then, the mass of the physical Higgs particle, h, is given by

$$m_h^2 = 2\lambda v^2. \tag{2.21}$$

There is a three-point interaction in this potential since the $\mathrm{SU}(2)_L$ symmetry is broken.

After the symmetry breaking, the gauge bosons also have mass terms coming from the kinetic term of the Higgs field. Substituting the VEV of H to the covariant derivative of H, we get

$$D_\mu \langle H \rangle = -\frac{iv}{2\sqrt{2}} \begin{pmatrix} g(W_\mu^1 - iW_\mu^2) \\ -gW_\mu^3 + g'B_\mu \end{pmatrix}. \tag{2.22}$$

Then,

$$(D_\mu \langle H \rangle)^\dagger D_\mu \langle H \rangle = \frac{1}{8}v^2 g^2 (W_\mu^1 - iW_\mu^2)(W^{1\mu} + iW^{2\mu}) + \frac{1}{8}v^2(-gW_\mu^3 + g'B_\mu)^2. \tag{2.23}$$

The eigenstate and the mass of charged gauge boson, $W^\pm$, is given by

$$W^\pm = \frac{W_\mu^1 \mp W_\mu^2}{\sqrt{2}}, \tag{2.24}$$

$$m_W = \frac{1}{2}gv. \tag{2.25}$$

The mass terms of neutral gauge bosons are given by

$$-\frac{1}{2}(W_\mu^3, B_\mu)\mathcal{M} \begin{pmatrix} W^{3\mu} \\ B^\mu \end{pmatrix}, \tag{2.26}$$

where the mass matrix, $\mathcal{M}$, is

$$\mathcal{M} = \frac{1}{4} \begin{pmatrix} g^2v^2 & -gg'v^2 \\ -gg'v^2 & g'^2v^2 \end{pmatrix}. \tag{2.27}$$

The diagonalization matrix is defined as

$$\begin{pmatrix} Z_\mu \\ A_\mu \end{pmatrix} = \begin{pmatrix} \cos\theta_W & -\sin\theta_W \\ \sin\theta_W & \cos\theta_W \end{pmatrix} \begin{pmatrix} W_\mu^3 \\ B_\mu \end{pmatrix}, \tag{2.28}$$

where the mixing angle, θ_W, is called "weak mixing angle" or "Weinberg angle". This mixing angle is related to the gauge couplings by the following relations.

$$\cos\theta_W = \frac{g}{\sqrt{g^2 + g'^2}}, \tag{2.29}$$

$$\sin\theta_W = \frac{g'}{\sqrt{g^2 + g'^2}}. \tag{2.30}$$

The masses of these eigenstates are given by

$$m_Z = \frac{1}{2}\sqrt{g^2 + g'^2}v, \tag{2.31}$$

$$m_A = 0. \tag{2.32}$$

Particle	Mass
h	125.10 ± 0.14 GeV
W	80.379 ± 0.012 GeV
Z	91.1876 ± 0.0021 GeV

Table 2: The mass spectrum of gauge bosons and Higgs boson [32].

The massless gauge boson is photon and the massive neutral gauge boson is Z-boson. The experimental values of gauge boson masses and Higgs boson mass are shown in Table 2

Using the mass eigenstates of the gauge bosons, the covariant derivative for $\mathrm{SU}(2)_L \times \mathrm{U}(1)_Y$ can be rewritten as

$$D_\mu = \partial_\mu - i\frac{g}{\sqrt{2}}(W_\mu^+ T^+ + W_\mu^- T^-) - i\frac{g}{\cos\theta_W} Z_\mu (T^3 - \sin^2\theta_W Q) - ieA_\mu Q, \tag{2.33}$$

where $T^\pm \equiv T^1 \pm iT^2$ and $Q = T^3 + Y$ is the electric charge of particles. The coupling, e, is the electron charge and defined as

$$e \equiv \frac{gg'}{\sqrt{g^2 + g'^2}}. \tag{2.34}$$

Then, we can rewrite fermion part as

$$\mathcal{L}_{\text{fermion}} = \sum_\psi \bar{\psi} i \not{\partial} \psi + \frac{g}{\sqrt{2}}(W_\mu^+ J_W^{\mu+} + W_\mu^- J_W^{\mu-}) + \frac{g}{\cos\theta_W} Z_\mu J_Z^\mu + eA_\mu J_{\text{EM}}^\mu, \tag{2.35}$$

where

$$J_W^{\mu+} = \bar{\nu}_L \gamma^\mu e_L + \bar{u}_L \gamma^\mu d_L, \tag{2.36}$$

$$J_W^{\mu-} = \bar{e}_L \gamma^\mu \nu_L + \bar{d}_L \gamma^\mu u_L, \tag{2.37}$$

$$\begin{aligned} J_Z^\mu = {} & \bar{\nu}_L \gamma^\mu (\frac{1}{2}) \nu_L + \bar{e}_L \gamma^\mu (-\frac{1}{2} + \sin^2\theta_W) e_L + \bar{e}_R \gamma^\mu (\sin^2\theta_W) e_R \\ & + \bar{u}_L \gamma^\mu (+\frac{1}{2} - \frac{2}{3}\sin^2\theta_W) u_L + \bar{u}_R \gamma^\mu (-\frac{2}{3}\sin^2\theta_W) u_R \\ & + \bar{d}_L \gamma^\mu (-\frac{1}{2} + \frac{1}{3}\sin^2\theta_W) d_L + \bar{d}_R \gamma^\mu (+\frac{1}{3}\sin^2\theta_W) d_R, \end{aligned} \tag{2.38}$$

$$\begin{aligned} J_{\text{EM}}^\mu = {} & \bar{e}_L \gamma^\mu (-1) e_L + \bar{u}_L \gamma^\mu (+\frac{2}{3}) u_L + \bar{d}_L \gamma^\mu (-\frac{1}{3}) d_L \\ & + \bar{e}_R \gamma^\mu (-1) e_R + \bar{u}_R \gamma^\mu (+\frac{2}{3}) u_R + \bar{d}_R \gamma^\mu (-\frac{1}{3}) d_R. \end{aligned} \tag{2.39}$$

The charged currents, $J_W^{\mu\pm}$, mix the different flavors of fermions, so called "flavor changing" current. The other currents are neutral and flavor conserved.

2.1.2 fermion masses and CKM matrix

After the symmetry breaking, fermions also obtain masses from the Yukawa terms. For example, mass terms of the up-type quarks are given by

$$\begin{aligned} -y_u^{ij}\bar{q}_L^i\langle\tilde{H}\rangle u_R^j + (h.c.) &= -\frac{v}{\sqrt{2}}y_u^{ij}\bar{u}_L^i u_R^j + (h.c.) \\ &= -\bar{u}_L^i\mathcal{M}_u^{ij}u_R^j + (h.c.), \end{aligned} \tag{2.40}$$

where y_u^{ij} is a complex 3×3 matrix and we define a mass matrix, $\mathcal{M}_u^{ij} \equiv y_u^{ij}v/\sqrt{2}$. We can get mass terms for down-type quarks and charged leptons in the same way.

$$-\sum_{f=u,d,e}\bar{f}_L^i\mathcal{M}_f^{ij}f_R^j + (h.c.). \tag{2.41}$$

To diagonalize these mass matrices, we use two unitary matrices, U_L^f and U_R^f. Then, the mass eigenstates of fermions are given by

$$(f_L^{mass})^i = (U_L^{f\dagger})^{ij}f_L^j, \tag{2.42}$$

$$(f_R^{mass})^i = (U_R^{f\dagger})^{ij}f_R^j. \tag{2.43}$$

Using these matrices, we get

$$\begin{aligned} -\sum_f \bar{f}_L^i\mathcal{M}_f^{ij}f_R^j + (h.c.) &= -(\bar{f}_L^{mass})^l(U_L^{f\dagger})^{li}\mathcal{M}_f^{ij}(U_R^f)^{jk}(f_R^{mass})^k + (h.c.) \\ &= -(U_L^{f\dagger}\mathcal{M}_f U_R^f)^{lk}(\bar{f}_L^{mass})^l(f_R^{mass})^k + (h.c.), \end{aligned} \tag{2.44}$$

where

$$\begin{aligned} U_L^{f\dagger}\mathcal{M}_f U_R^f &= \frac{v}{\sqrt{2}}U_L^{f\dagger}y_f U_R^f \\ &= \begin{cases} diag(m_u, m_c, m_t) & f = u, \\ diag(m_d, m_s, m_b) & f = d, \\ diag(m_e, m_\mu, m_\tau) & f = e. \end{cases} \end{aligned} \tag{2.45}$$

The neutrinos do not have mass terms because the right-handed neutrinos are not included in the SM. This is one of the problems in the SM as we will discuss in the next section.

The fermion mass values obtained from the experiments are summarized in Table 3. The heaviest fermion in the SM is the top quark, $m_t \simeq 172$ GeV and the lightest fermion is the electron (except for neutrinos), $m_e \simeq 0.5$ MeV. Hence the Yukawa interaction varies in scale by six orders of magnitude from the top quark to the electron. If we try to introduce neutrino masses, things get more serious as we will show later.

Since the neutral currents via Z-boson and photon are proportional to $\bar{\psi}_{L,R}\gamma^\mu\psi_{L,R}$ as in Eqs. (2.38) and (2.39), thus the diagonalization matrices, $U_{L,R}^f$ are canceled. However

Particle	Mass
u	$2.16^{+0.49}_{-0.26}$ MeV
c	1.27 ± 0.02 GeV
t (Pole)	172.4 ± 0.7 GeV
d	$4.67^{+0.48}_{-0.17}$ MeV
s	93^{+11}_{-5} MeV
b	$4.18^{+0.03}_{-0.02}$ GeV
e	$0.5109989461 \pm 0.0000000031$ MeV
μ	$105.6583745 \pm 0.0000024$ MeV
τ	1776.86 ± 0.12 MeV

Table 3: The SM fermion mass spectrum [32]

the charged currents, Eqs. (2.36) and (2.37), are proportional to $\bar{u}_L \gamma^\mu d_L$, then the product of diagonalization matrices is remained.

$$\bar{u}_L^i \gamma^\mu d_L^i = (\bar{u}_L^{mass})^k \gamma^\mu (U_L^{u\dagger})^{ki} (U_L^d)^{il} (d_L^{mass})^l. \tag{2.46}$$

We define the Cabbibo-Kobayashi-Maskawa matrix [33, 34],

$$V_{\rm CKM} \equiv U_L^{u\dagger} U_L^d = \begin{pmatrix} V_{ud} & V_{us} & V_{ub} \\ V_{cd} & V_{cs} & V_{cb} \\ V_{td} & V_{ts} & V_{tb} \end{pmatrix}. \tag{2.47}$$

This 3×3 unitary matrix has nine free parameters. Three of them are mixing angles and the others are phases. Utilizing the phase rotation of six quark fields, we can eliminate five phases. So the remained free parameters are three angles and one phase. The experimental results [32] for the magnitudes of the CKM elements are

$$|(V_{\rm CKM})_{ij}| = \begin{pmatrix} 0.97401 \pm 0.00011 & 0.22650 \pm 0.00048 & 0.00361^{+0.00011}_{-0.00009} \\ 0.22636 \pm 0.00048 & 0.97320 \pm 0.00011 & 0.04053^{+0.00083}_{-0.00061} \\ 0.00854^{+0.00023}_{-0.00016} & 0.03978^{+0.00082}_{-0.00060} & 0.999172^{+0.000024}_{-0.000035} \end{pmatrix}. \tag{2.48}$$

This matrix shows the off-diagonal elements are much smaller than the diagonal elements. Thus the flavor changing process via $W^\pm$ is suppressed in the SM.

2.2 Beyond the SM

2.2.1 The problems in the SM

- Strong CP problem
  We can write the CP violating gauge invariant term as follows.

$$\Delta \mathcal{L}_\theta = \frac{\theta g_s^2}{64\pi^2} \epsilon^{\mu\nu\rho\sigma} G^A_{\mu\nu} G^A_{\rho\sigma}, \tag{2.49}$$

where θ is the coupling of this term. It is reasonable to assume that $\theta \sim \mathcal{O}(1)$. This term has a contribution to the neutron electric dipole moment. The experiment gives the very small upper bound on the coupling, $\theta < 10^{-11}$ [35]. Why it takes such a tiny value is known as "The Strong CP Problem".

- No mass terms of the neutrino species
  Neutrino oscillations imply that neutrinos are massive. However, there are no neutrino mass terms in the SM. This is a Standard Model problem that has to be solved. Although their absolute masses are not known today, the values of the two mass-square differences are known [36].

$$\Delta m^2_{21} \simeq 7.6 \times 10^{-5}\mathrm{eV}^2, \tag{2.50}$$

$$|\Delta m^2_{31}| \simeq 2.5 \times 10^{-3}\mathrm{eV}^2. \tag{2.51}$$

  where $\Delta m^2_{ij} = m^2_i - m^2_j$ and indices show the generations. These limitations are derived from observations of solar and atmospheric neutrinos. These results mean that two of three generations are massive at least. However, there are still two possibilities for the order of mass. (Normal ordering : $m_3 > m_2 > m_1$ or Inverted ordering : $m_2 > m_1 > m_3$)
  From the cosmological observations, we obtain the upper bound on the sum of their masses [1],

$$\sum m_\nu < 0.11\mathrm{eV}. \tag{2.52}$$

  So the masses of neutrinos are about 0.01 eV. The simplest solution is to introduce the right-handed neutrinos to the SM. Then we can write the Yukawa terms for neutrinos and obtain masses from the VEV of the Higgs boson. However, the required magnitudes of Yukawa couplings for neutrino masses are about 10^{-13}. These are too small compared to the Yukawa interaction of the top quark, $y_t \sim 1$. This is a further problem for the mass of neutrinos.

- No dark matter candidate
  There is a lot of evidence that dark matter exists, but there are no candidate particles in the SM. It remains possible that dark matter is not an elementary particle, but it can be successfully explained by extending the SM. We will focus on this topic in Chapter. 3.

As described above, there are many points that should be improved in the SM, and many extended models have been proposed to date.

Chapter 3

Dark Matter

In this thesis, we extend the SM to explain the existence of dark matter. This chapter is devoted to this topic.

3.1 Indirect evidence of dark matter

There are some of indirect evidence of the existence of dark matter.

- Galaxy rotation curve
  The rotation velocity of stars in a spiral galaxy can be directly observed and also predicted by using the observed distribution of the visible matters. The rotation velocity of the star at r, the distance from the center of the galaxy, is given by

$$v(r) = \sqrt{\frac{G_N M(r)}{r}}, \tag{3.1}$$

  where $G_N (= 6.67430 \times 10^{-11}\ \mathrm{m^3\ kg^{-1}\ s^{-2}}$ [32]) is the Newtonian constant of gravitation. $M(r)$ is defined as

$$M(r) \equiv \int_0^r 4\pi r'^2 \rho(r') dr', \tag{3.2}$$

  where $\rho(r')$ is the visible matter density. Here ρ is assumed to be spherically symmetric. For the large r region, the density, ρ, can be neglected and $M(r) \simeq M_{\mathrm{total}}(\mathrm{Constant})$. Then we get

$$v(r) \simeq \sqrt{\frac{G_N M_{\mathrm{total}}}{r}} \propto \frac{1}{\sqrt{r}}. \tag{3.3}$$

  If nothing exists outside of the visible matter, we can see that the rotation speed decreases by $1/\sqrt{r}$ in the region far from the center.

  For example, Fig.1 shows the rotation curve of the Triangulum Galaxy (M33) [37]. The observed values (points) are different from the estimated values (dashed line) from the visible disk. The rotation velocity is nearly constant for the region where visible matter contributions are small. This suggests an invisible presence, dark matter. To date, numerous galaxy rotation curves have been observed [38–41].

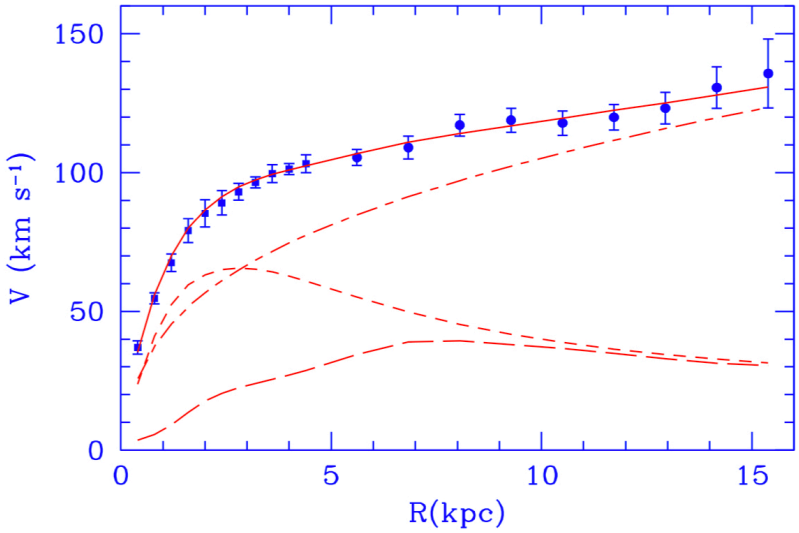

Figure 1: The rotation curve (points) of the Triangulum Galaxy. The horizontal axis shows the distance from the center of the galaxy. The long dashed line and short dashed line represent the contributions from the gas and stellar disk. The dashed-dotted line shows the dark matter contribution. Figure taken from [37]

- Large structure of the universe
  The formation of large-scale structure in the universe has been analyzed using N-body simulations. It is known that simulations using the ΛCDM model, which assumes collisionless and non-relativistic dark matter, can reproduce the observed large-scale structure of the universe well [42–44]. In addition to suggesting the existence of dark matter, it is also clear that dark matter should be non-relativistic during the time of structure formation.

- Cosmic microwave background (CMB)
  The CMB is electromagnetic radiation that was emitted after the end of recombination in the history of the universe. It contains a lot of important information since it is the oldest electromagnetic radiation that can be observed today. The CMB has the same spectrum as that of black body radiation with a temperature of about 2.7 K, and is approximately isotropic, but contains small anisotropies, which can be precisely measured and analyzed to determine cosmological parameters.

  From the observation of the CMB, we can get to know the components of energy in the universe. The Planck collaboration give the pricise values [1]. Baryonic matter accounts for about 5% and the dark matter accounts for about 27% of the total energy of the universe. Thus the dark matter contribution is not negligible.

- Bullet cluster
  The object discovered by the X-ray telescope, 1E0657-558, is a system after the collision of two clusters and is called the Bullet cluster [45]. When the two clusters pass each other, the gas, which is interstellar material, collides and slows down, so

it still remains in the central part of the system. On the other hand, gravitational lensing shows that most of the mass passes by almost without collision, and is completely separated from the gas distribution. Since most of the baryonic mass is gas, if there were no dark matter, it would not be separated in this way, and this is taken as evidence for the existence of dark matter.

All of the above pieces of evidence were found in observations involving gravitational interaction. Except for these, we currently have very little information about dark matter. Some properties which we know today are the followings.

- electrically neutral
  Strictly speaking, tiny charged dark matter is allowed. The upper bound on the electrical charge of dark matter which has mass, $m_{\rm DM}$, is $10^{-14}\ m_{\rm DM}/({\rm GeV}\cdot e)$ [46].

- Non-relativistic (cold dark matter)
  Non-relativistic dark matter is desirable in terms of the large structure formation of the universe.

- stable (long-lived)
  At least, the dark matter is long-lived as long as the universe age.

- the energy density of dark matter, relic abundance
  From the current results of Planck Collaboration [1], dark matter makes up about 27% of the total energy in the universe.

- No direct evidence in the observations and experiments so far
  This means that DM models must be hidden from these observations and experiments. For example, the dark matter direct detection, which we will review in Sec.3.4, strongly constrains the model parameters. These constraints make the model building very difficult today.

We focus on the elementary particle for the candidate of the dark matter in the following sections. However, we do not know the spin, the mass, and the interaction with the SM particles so that various models are possible.

DM candidate in SM?

A dark matter candidate should satisfy the above properties. Then, is there a dark matter candidate in the SM? Neutrinos are only dark matter candidates in the SM because they are stable, massive, electrically neutral, and have the weak interaction. However, there are two main reasons why neutrinos are not dark matter.

- Structure formation
  Neutrinos are relativistic in the early universe so that not favored.

- They can not explain the whole relic abundance.
  We know that the amount of neutrinos remaining in the current universe is less than 10% of the required amount of dark matter since the masses of them are considered to be extremely light.

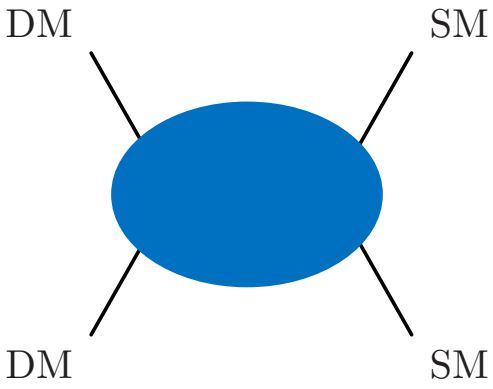

Figure 2: The annihilation process of WIMPs from left to right.

Therefore we consider the extension of the SM to explain the existence of dark matter.

3.2 WIMP -thermal freeze-out mechanism-

To reproduce the observed relic abundance the thermal freeze-out mechanism has been favored for a long time. Models that use this mechanism are called WIMP (Weakly interacting massive particle) models. Our model is also based on this idea. We briefly review WIMP models here.

Discrete symmetries such as Z_2 symmetry are often used to stabilize dark matter in many dark matter models, not just the WIMP models. The dark matter particle is assigned -1 charge, so it is called an odd particle under this symmetry. On the other hand, SM particles are assigned $+1$ charge, so they are called even particles. This discrete symmetry prohibits interactions that contain an odd number of dark matter particles. Then, it is impossible for a dark matter particle to decay only to the SM particles. Hence the dark matter in these models is stable.

In WIMP models we assume that the dark matter has the mass and a weakly interaction to the SM particles. Then dark matter and SM particles are in the same thermal bath in the early universe. As the universe expanding and the temperature decreasing, dark matter becomes non-relativistic. Then the dark matter particles are pair annihilated to the SM particles. The energy density of dark matter is exponentially decreasing. In sooner or later, the dark matter particles will not be able to be pair annihilated so that the energy density per comoving volume is fixed. This mechanism is called the thermal freeze-out mechanism. The value of the pair annihilation cross section determines the energy density of dark matter in this mechanism. We will show the details of this mechanism using the Boltzmann equation in Sec.3.3.

WIMPs have an annihilation cross section of a reasonable size, which means that another view of the same process can be searched in various observations. Fig.2 schematically shows the annihilation process of WIMPs from left to right. This process can be searched by the indirect detection experiments. If you look at this figure from top to bottom, this diagram shows the WIMP-SM particles scattering process that can be observed by the direct detection experiments. If you look at this from right to left, this shows the

WIMPs production process that can occur in the particle colliders like LHC. There are various experiments and observations which explore dark matter. However, there is no signal, unfortunately. We will show the results of each experiment in Sec.3.4 and 3.5.

3.3 Relic density

To calculate the energy density of dark matter we must deal with non-equilibrium thermodynamics. The Boltzmann equation which describes the change in the particle number density of the particle of interest, the dark matter is given by

$$\frac{dn}{dt} = -3Hn - \langle \sigma_{\text{eff}} v \rangle (n^2 - n_{\text{eq}}^2). \tag{3.4}$$

where n is the number density of dark matter, t is the time, H is the Hubble parameter. n_{eq} is the equilibrium number density of the dark matter. $\langle \sigma_{\text{eff}} v \rangle$ is the thermal average of the effective annihilation cross section. The first term on the right-hand side represents the contribution of density dilution due to the expansion of the universe and the second term shows the contribution of the dark matter annihilation.

If there are some odd particles in the model, we must include their contributions. The thermal average of the effective annihilation cross section,$\langle \sigma_{\text{eff}} v \rangle$ is defined by

$$\langle \sigma_{\text{eff}} v \rangle \equiv \sum_{i,j} \frac{\langle \sigma_{ij} v_{ij} \rangle n_{i,\text{eq}} n_{j,\text{eq}}}{n_{\text{eq}}^2}, \tag{3.5}$$

where $\langle \sigma_{ij} v_{ij} \rangle$ is the thermally averaged annihilation cross section which include all odd particles processes. Odd particles finally decay into the dark matter particle so that their number density should be considered in the calculation of relic abundance of dark matter. These processes are called "co-annihilation" [47]. Since the dark matter candidate should be lighter than the other odd particles in a model, these odd particles are non-relativistic. Thus if their masses are much heavier than the dark matter, their number density is exponentially small, so the co-annihilation process that includes these particles is negligible. Therefore the mass difference between the dark matter particle and their partner is essential for the co-annihilation.

Since the contribution of density dilution due to the expansion of the universe is not an intrinsic part of what we want to know, such as the decrease in the number of particles depending on the annihilation process, we will rewrite it as an amount per unit volume by dividing it by the entropy, s,

$$Y \equiv \frac{n}{s}. \tag{3.6}$$

The entropy of the universe is given by

$$s = \frac{2\pi^2}{45} g_{*s} T^3, \tag{3.7}$$

where T is the temperature of the universe and

$$g_{*s} = \sum_{i=\text{bosons}} g_i \left(\frac{T_i}{T}\right)^3 + \sum_{j=\text{fermions}} g_j \left(\frac{T_j}{T}\right)^3. \tag{3.8}$$

T_i is the temperature of the particle i and g_i is the number of degrees of freedom of the particle i. Also we introduce the dimensionless parameter, $x \equiv m/T$. Then we can rewrite the Boltzmann equation(3.4) as follows.

$$\frac{dY}{dx} = -\frac{s\langle\sigma_{\text{eff}}v\rangle}{xH(x)}(Y^2 - Y_{eq}^2). \tag{3.9}$$

This equation can not be solved analytically. So we calculate numerically and obtain the current value, Y_0. Then, the energy density of the dark matter is given by

$$\rho_{\text{DM}} = m_{\text{DM}} n_{\text{DM}} = m_{\text{DM}} s_0 Y_0, \tag{3.10}$$

where m_{DM} is the mass of the dark matter and s_0 is the current value of the entropy. Dividing this value by the critical density, $\rho_{\text{crit}} = 3H_0^2/8\pi G$, we get the dimensionless value,

$$\Omega_{\text{DM}} \equiv \frac{\rho_{\text{DM}}}{\rho_{\text{crit}}}. \tag{3.11}$$

The observed value of $H_0 = 67.66 \pm 0.42$ km/s/Mpc is given by [1]. Before the Planck measurements, this value contained the large uncertainty. So we consider $H_0 = h \times 100$ km/s/Mpc and use Ωh^2 as the value of the relic abundance. The current experimental value of the dark matter relic abundance is given by the Planck collaboration [1].

$$\Omega h^2 = 0.120 \pm 0.001. \tag{3.12}$$

To understand the behavior of the thermal freeze-out mechanism, we assume that the freeze-out suddenly happens for simplicity. Then we can define the freeze-out temperature, T_f, as follows.

$$n_f \langle\sigma_{\text{eff}}v\rangle_{T_f} = H(T_f), \tag{3.13}$$

where n_f and $\langle\sigma_{\text{eff}}v\rangle_{T_f}$ is the number density and the effective annihilation cross section at the freeze-out.

Under this assumption, we find the relation between the current energy density and the energy density at the freeze-out temperature.

$$n_0 \simeq \frac{s_0}{s_f} n_f, \tag{3.14}$$

where s_0 and s_f are the entropy at the present temperature and the freeze-out temperature, respectively. The energy density at the freeze-out temperature is equal to the energy density in the thermal equilibrium. Then we get

$$n_f \simeq g \frac{m_{\text{DM}}^3}{(2\pi)^{3/2}} x_f^{-3/2} e^{-x_f}. \tag{3.15}$$

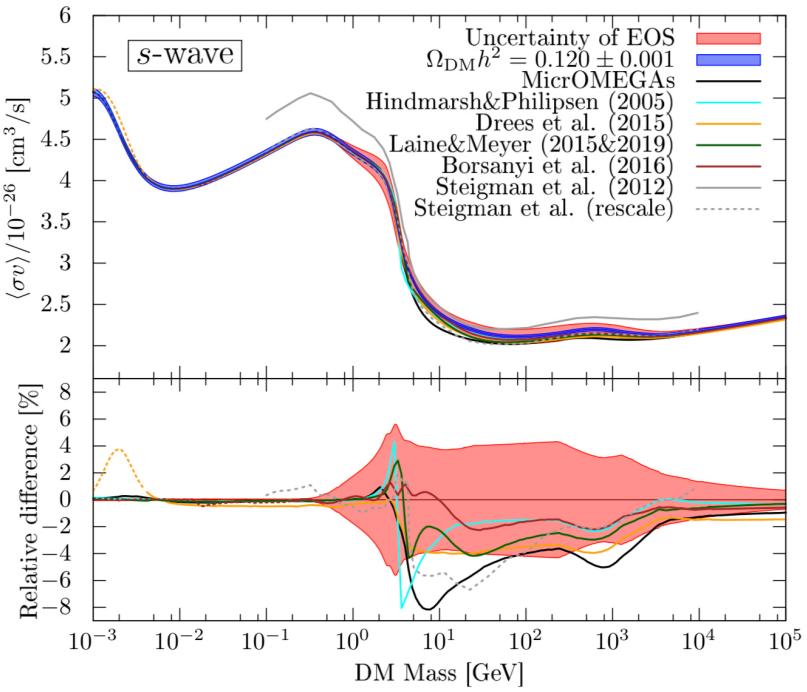

Figure 3: The required values of the thermally averaged cross section to obtain the observed relic abundance. Figure taken from [48].

where g is the number of degrees of freedom for dark matter. Therefore we obtain

$$\begin{aligned}\Omega h^2 =& \frac{m_{\rm DM} n_0}{\rho_{\rm crit}} h^2 \\ \simeq& \frac{g}{(2\pi)^{3/2}} \frac{g_{*s}(T_0)}{g_{*s}(T_f)} \frac{T_0^3 m_{\rm DM}}{\rho_{\rm crit}/h^2} x_f^{3/2} e^{-x_f}. \end{aligned} \tag{3.16}$$

Here we consider WIMP, so the dark matter has a weakly interaction. Then $\langle\sigma v\rangle$ is about 10^{-26} cm^3/s. Substituting this value to Eqs.(3.13) and (3.16), we get $x_f \sim 25$ and the relic abundance, $\Omega h^2 \sim 0.1$. Therefore if the dark matter has the weak interaction, the relic abundance of dark matter can be easily explained. The precise values of the required annihilation cross section for the WIMP mass are numerically calculated in [48] and shown by Fig.3. For 10 GeV$\lesssim m_{\rm DM} \lesssim$ 100 TeV , $\langle\sigma v\rangle \sim 2 \times 10^{-26}$ cm^3/s can reproduce the observed value of relic abundance in WIMP models.

In this derivation, there are many parameters which have much different mass scale each other. However, it is really interesting that eventually, we need a cross section of about the weak interaction to obtain the observed relic abundance. So sometimes it is called "the WIMP miracle". Even though numerous WIMP models have been studied over the years, no dark matter signal has yet been discovered. From the next section, we explain what observations and experiments have been carried out in the exploration of dark matter.

3.4 Direct Detection

The Earth is in the Milky Way Galaxy which is considered to be a dark matter rich object. So dark matter particles can be scattered with matters around us. Today the XENON collaboration [3] gives the strongest constraint on the scattering cross section. Other plans are underway to observe this scattering, including the LZ (LUX ZEPLIN) [49], the PandaX-4T [50], and the DarkSide-20k [51].

The direct detection experiments observe the reaction rate of the interaction between the nucleus at the laboratory and the dark matter around the Earth.

$$R = \frac{\sigma \rho_{\rm DM}(r_\odot) v_{\rm DM} F_\xi}{m_{\rm DM} M_A}. \tag{3.17}$$

The left-hand side is the reaction rate, R, that is observable. M_A is the mass of the nucleus and F_ξ is the form factor of the nucleus. These parameters are determined by the target nucleus. $\rho_{\rm DM}$ is the mass density of the dark matter around the Earth and $v_{\rm DM}$ is the velocity of the dark matter. The numerical values used by the XENON collaboration are

$$\rho_{\rm DM}(r_\odot) \sim 0.3 \text{ GeV/cm}^3, \tag{3.18}$$

$$v_{\rm DM} \sim 220 \text{ km/s}, \tag{3.19}$$

where $r_\odot \sim 8.5$ kpc is the distance from the Sun to the Galactic center. Estimated values for $\rho_{\rm DM}(r_\odot)$ are summarized in [52]. The results are highly variable. The dark matter velocity distribution around us is determined by using data from the Apache Point Observatory Galactic Evolution Experiment (APOGEE) in [53],

$$v_{\rm DM} \sim 218 \pm 6 \text{ km/s}. \tag{3.20}$$

This value is consistent with the Milky Way-like galaxy simulations [54]. The unknown parameters are the nucleus-DM cross section, σ,and the dark matter mass, $m_{\rm DM}$. These parameters depend on the dark matter model.

In the vector dark matter model, the nucleus-DM cross section is given by [55]

$$\sigma = \frac{1}{\pi}\left(\frac{M_A}{M_A + m_{\rm DM}}\right)^2 \left[|n_p f_p + n_n f_n|^2 + \frac{8}{3}\frac{J+1}{J}|a_p\langle S_p\rangle + a_n\langle S_n\rangle|^2\right]. \tag{3.21}$$

n_p and n_n are the number of protons and neutrons in the target nucleus, respectively. J is the total spin of the nucleus and $\langle S_N\rangle$ $(N = p, n)$ are the expectation values of the total spin of protons and neutrons in the nucleus. f_N is the spin-independent effective coupling and a_N is the spin-dependent effective coupling. These effective couplings for our model will be calculated in Sec.6.2.

The spin-independent dark matter-nucleus cross section is proportional to the number of protons or neutrons, so enhanced by the atomic number. The constraint on the spin-independent cross section is stronger than the spin-dependent one. Fig.4 shows the current results of the XENON1T experiment. For TeV scale dark matter, the upper bound of the dark matter nucleon cross section is $\sigma \sim 10^{-45}[\text{cm}^2]$. Many of the WIMP models are constrained by this bound.

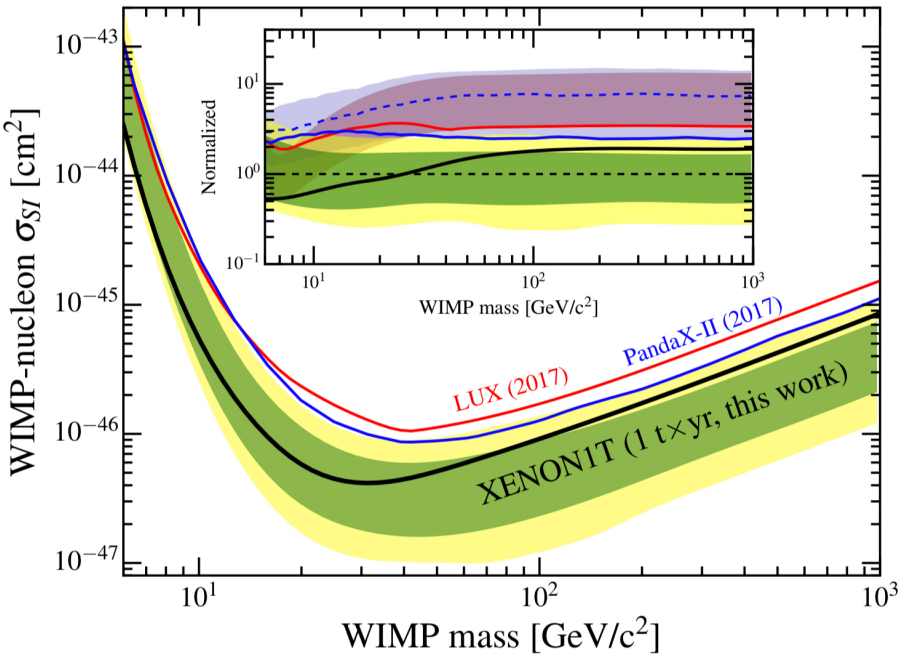

Figure 4: Current bounds on the spin-independent WIMP-nucleon cross section. Figure taken from [3].

3.5 Indirect Detection

The indirect detection experiments search for the γ-ray, cosmic ray, and neutrinos from dark matter rich regions. Here we focus on the γ-ray search. For example, the Galactic center of the Milky Way galaxy is one of the attractive objects. The H.E.S.S. (High Energy Stereoscopic System) Collaboration uses the Imaging Atmospheric Cherenkov Telescopes at the Earth and the LAT (Large Area Telescope) Collaboration uses the Fermi Gamma-ray Space Telescope. The former constrains on the relatively heavy dark matter, while the latter constrains on the lighter dark matter, as we will show later.

Dark matter is considered to be electrically neutral, so the dark matter pair annihilation into two photons that can be searched by the indirect detection experiments is prohibited at the tree-level. However, it is known that such a process can be enhanced by the "Sommerfeld effect" when the dark matter particle has the electroweak interaction, such as pure Wino dark matter in the Supersymmetric Standard Model. Therefore these results can be a stringent limit on such dark matter models.

The differential γ-ray flux per unit energy produced by the annihilation of dark matters in a solid angle $\Delta\Omega$ is given by

$$\frac{d\Phi}{dE_\gamma} = \frac{\langle\sigma v\rangle}{8\pi m_{\rm DM}^2}\frac{dN_\gamma}{dE_\gamma} \times J(\Delta\Omega), \tag{3.22}$$

where $\langle\sigma v\rangle$ is the velocity-averaged annihilation cross section. $m_{\rm DM}$ is the dark matter mass. N_γ is the number of photons per annihilation and $dN_\gamma/dE_\gamma = 2\delta(E_\gamma - m_{\rm DM})$ for

Profiles	Einasto	NFW
$\rho_s(\mathrm{GeVcm}^{-3})$	0.079	0.307
$r_s(\mathrm{kpc})$	20.0	21.0
α_s	0.17	/

Table 4: profile parameters used in [61]

the annihilation into 2 photons. J is called "J-factor" and given by

$$J(\Delta\Omega) = \int_{\Delta\Omega} d\Omega \int ds\ \rho^2_{\mathrm{DM}}, \tag{3.23}$$

where ρ_{DM} is the density of the dark matter and s is the distance from the Earth to the annihilation point. The integration is done for the region of interest (ROI). The J-factor is determined by the dark matter density profile for an observed object. For instance, the J-factor for an object of uniform density ρ with radius r, located d ($d \gg r$) away from the Earth, is expressed as

$$J \simeq \frac{4\pi r^3 \rho^2}{3d^2}. \tag{3.24}$$

Thus the most promising objects for indirect detection are those with high dark matter density ($J \propto \rho^2$), large volumes ($J \propto V$), and close to the Earth ($J \propto d^{-2}$). A good example is the center of the Milky Way Galaxy. We will focus on this in the following.

Although the Galactic center is a fascinating object, there is a very large indeterminacy in the dark matter density profile. The profile can only be estimated from N-body simulations. For example, the Navarro, Frenk, and White (NFW) profile [56] and the Einasto profile [57] are respectively given by

$$\rho_{\mathrm{NFW}}(r) = \rho_s \left(\frac{r}{r_s} \left(1 + \frac{r}{r_s} \right)^2 \right)^{-1}, \tag{3.25}$$

$$\rho_{\mathrm{Einasto}}(r) = \rho_s \exp\left[-\frac{2}{\alpha_s} \left(\left(\frac{r}{r_s} \right)^{\alpha_s} - 1 \right) \right], \tag{3.26}$$

where r is the distance from the Galactic center and the numerical values often used for the other parameters are shown in Table 4. Fig. 5 shows the density distributions using these parameters. ρ_s, α_s and r_s are numerically determined to satisfy the measured values like the local dark matter density around us, $\rho_{DM}(r_\odot) \sim 0.39$ GeV/cm^3. This value, $\rho_{DM}(r_\odot)$ is different from the value used by the XENON collaboration, however a more accurate one obtained by using a Bayesian analysis [58]. For the NFW profile,

$$\rho_{\mathrm{DM}}(r_\odot) = 0.389 \pm 0.025\ \mathrm{GeV\ cm}^{-3}, \tag{3.27}$$

and for the Einasto profile,

$$\rho_{\mathrm{DM}}(r_\odot) = 0.385 \pm 0.027\ \mathrm{GeV\ cm}^{-3}. \tag{3.28}$$

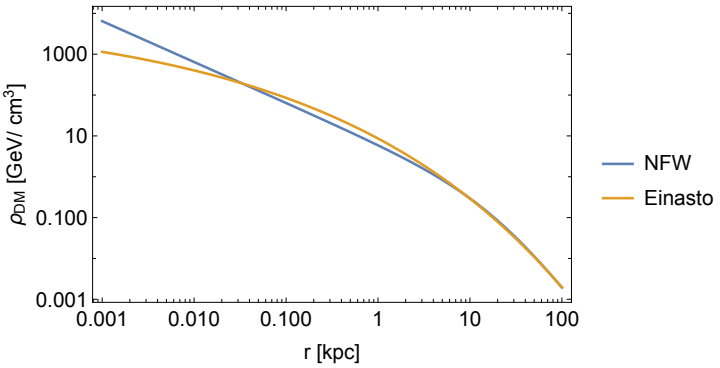

Figure 5: The density profile around the Galactic center as a function of the radius from the center.

The distance from the Sun to the Galactic center, $r_\odot$, also include ambiguities. In this analysis, $r_\odot = 8.33 \pm 0.35$ kpc in [59] is used, although the recent study [60] find $r_\odot = 8.127 \pm 0.031$ kpc.

Fig.6 shows the current constraints on the velocity averaged dark matter annihilation cross section to 2 photons from the H.E.S.S. [61] and fermi-LAT [62]. They observed the γ-ray flux from the Galactic center of the Milky Way Galaxy. For TeV scale dark matter, they give the upper limit on the annihilation cross section, $\langle \sigma v \rangle_{\gamma\gamma} \lesssim 10^{-27}$ cm^3/s. As you can see, these constraints depend on the dark matter density profiles. In this analysis, they consider only the cuspy profile for the dark matter density at the center that is consistent with the N-body simulations [63]. However, some observations show that the dark matter density near the center is constant [64–68]. They claimed that if the dark matter distribution at the center is the kpc-sized cored profile, the H.E.S.S. bounds can be altered by 2-3 orders of magnitude. It must be noted that the use of this bound involves great indeterminacy.

3.6 Status of WIMP models

Since the amount of the WIMP relic abundance is determined by the size of the annihilation cross section, the interaction with the SM particles is important. Therefore, WIMP models are often classified according to their interaction with the SM particles. The Higgs boson mediated models are called Higgs portal models, and various types of models have been proposed because they are relatively easy to construct. However, these models are strongly restricted in the parameter range from the direct detection experiments. Let us first examine these situations using the simplest model, the singlet scalar dark matter model [69–71].

3.6.1 Singlet real scalar dark matter

This model is very simple. The dark matter particle, S, is spin-0 and a singlet under the SM gauge symmetry. The Z_2 symmetry is imposed to stabilize the dark matter, so this

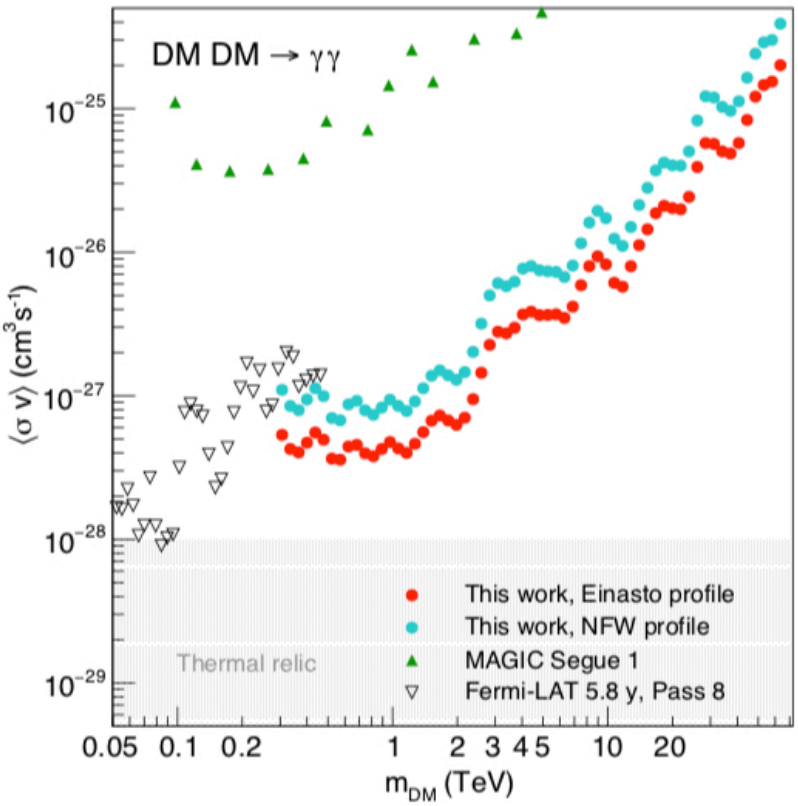

Figure 6: Current bounds on the velocity averaged dark matter annihilation cross section to 2 photons. The red (blue) points show the bounds for the Einasto (NFW) profile from the H.E.S.S. collaboration [61]. The white triangles show the bounds from the Fermi-LAT [62]. The figure is taken from [61]

model is invariant under $S \to -S$. Then, the Lagrangian is given by

$$\mathcal{L} = \mathcal{L}_{\rm SM} + \frac{1}{2}\partial_\mu S \partial^\mu S - V_S, \tag{3.29}$$

where

$$V_S = \frac{1}{2}m_{S0}^2 S^2 + \lambda_{HS} S^2 H^\dagger H + \lambda_S S^4. \tag{3.30}$$

After the electroweak symmetry breaking, the SM Higgs, H, has the VEV, v. Then, the potential in the unitarity gauge is rewritten as

$$V_S = \frac{1}{2}m_S^2 S^2 + \lambda_{HS} v S^2 h + \frac{1}{2}\lambda_{HS} h^2 S^2 + \lambda_S S^4, \tag{3.31}$$

where the mass of S is given by

$$m_S^2 = m_{S0}^2 + \lambda_{HS} v^2. \tag{3.32}$$

Through the interaction of the second term, the dark matter annihilates into the SM particles. So λ_{HS} is relevant to the value of relic abundance. A larger λ_{HS} results in a

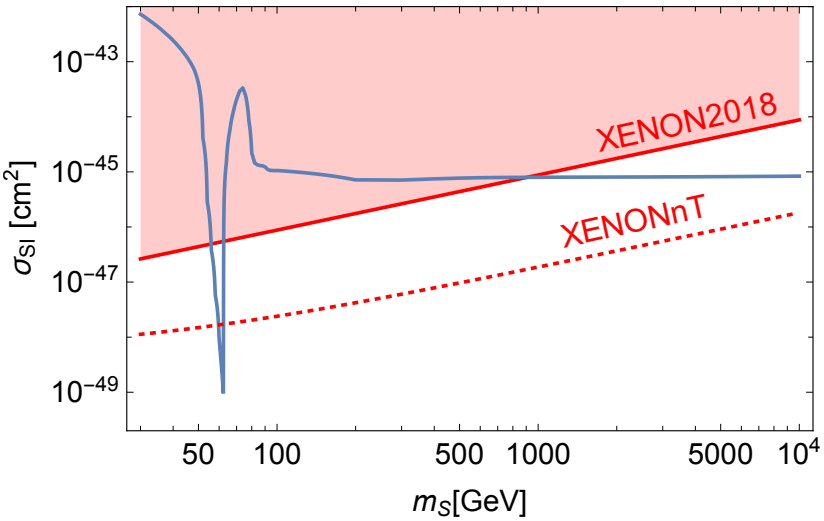

Figure 7: The blue line shows the spin-independent dark matter nucleon cross section as a function of the mass of the dark matter, m_S. λ_{HS} is determined to obtain $\Omega h^2 = 0.12$. The red shaded regions are excluded by the XENON1T experiment [3]. The red dotted line show the prospect of the XENONnT experiment [72].

larger annihilation cross section and therefore a smaller amount of the relic abundance, while a smaller λ_{HS} results in a larger amount of the relic abundance. We can choose the value of λ_{HS} to reproduce the observed dark matter energy density.

The h-S-S coupling also contributes to the spin-independent dark matter-nucleon cross section that is searched by the direct detection experiments. Fig.7 shows the spin-independent dark matter-nucleon cross section. λ_{HS} is determined to obtain the observed relic abundance. Except for the resonance region ($m_S \sim m_h/2$), $m_S < 900$ GeV region is already excluded. The heavy mass region is allowed, however, will be searched up to 10 TeV by the XENONnT experiment [72].

Higgs portal models and Z portal models for spin-0,1/2,1 dark matter are studied in [73, 74] and most parameter region is excluded for both cases by the direct detection experiments. To avoid this bound, there are ways to add particles to the model. Some of these models are summarized in [74]. Since the relic density decreases via processes mediated by added particles, the correct amount of the relic density can be explained even if the contribution of the processes constrained by the direct detection experiments is small.

3.6.2 EWIMP model

From the results of the previous sub-section, we found that it is difficult for the Higgs portal (and Z portal) models to avoid the direct detection bounds. These models rely on the Higgs mediated processes to reproduce the relic density, however, the same diagrams contribute to the spin-independent dark matter-nucleon cross section. Therefore the challenge is how to build a model that is not already limited by the direct detection experiments.

One solution is the electroweakly interacting massive particle (EWIMP). EWIMP is a multiplet under the $SU(2)_L$ symmetry and depends on the electroweak interaction to reproduce the observed value of the relic abundance. The EWIMP model can be considered for the combination of the representation of $SU(2)_L$, the magnitude of the Hypercharge, Y, and the spin of dark matter. The famous one is the pure Wino dark matter in the supersymmetric model. Wino is a $SU(2)_L$ triplet fermion, so does not have direct interaction with the Higgs doublets. Hence the Wino-nucleon scattering is induced by the loop diagrams. The spin-independent cross section is calculated up to the next-to-leading order in $\alpha_s (= g_s^2/4\pi)$ in [75], $\sigma_{\rm SI} \simeq 2.3 \times 10^{-47}$ cm^2. Thus this model can not be excluded easily by the direct detection experiments.

EWIMP is a multiplet under the $SU(2)_L$ symmetry, and hence there are partner particles. Their masses are nearly degenerate with the mass of dark matter so that the co annihilation processes are important for the relic density. Moreover, if their masses are much heavier than the electroweak gauge bosons, $W^\pm$ and Z, the EWIMP annihilation is enhanced by the Sommerfeld effect. Although it is difficult to explore EWIMP models by the direct detection experiments, this model can be probed by the indirect detection experiments due to the enhanced annihilation processes into photons. The prediction of the relic abundance can be altered by this effect. For the pure Wino, this effect reduces the relic abundance by about 50% [4] and $m_{\rm DM} \sim 3$ TeV is required for the observed energy density. The Sommerfeld effect can be the main feature of this type of model.

Many EWIMP models have been proposed. EWIMP models for spin-0 and spin-1/2 are summarized in [76]. In [77], various bounds are considered for the cases of $Y \neq 0$ fermion EWIMP and most parameter region is already constrained for $Y = 3/2$. Some non-renormalizable spin-1 EWIMP models have been proposed [5, 6, 78], however, there is not much discussion about the case of a spin-1. So we focus on the renormalizable model of the vector EWIMP model. In the next chapter, we explain our model that has the electroweakly interacting vector dark matter candidate.

Chapter 4

Model

The gauge symmetry is $\mathrm{SU}(3)_c \times \mathrm{SU}(2)_0 \times \mathrm{SU}(2)_1 \times \mathrm{SU}(2)_2 \times \mathrm{U}(1)_Y$ in our Model. Here, $\mathrm{SU}(3)_c$ is for the QCD as in the same as the SM. The matter and Higgs fields are summarized in Table 5.[1] In this section, we focus on the extended electroweak gauge sector, namely $\mathrm{SU}(2)_0 \times \mathrm{SU}(2)_1 \times \mathrm{SU}(2)_2 \times \mathrm{U}(1)_Y$. We denote the gauge fields of them as $W^a_{0\mu}$, $W^a_{1\mu}$, $W^a_{2\mu}$, and B_μ, respectively, where $a = 1, 2, 3$. Their gauge couplings are g_0, g_1, g_2, and g', respectively. The gauge transformation of two Higgs fields, Φ_1 and Φ_2 , are given by

$$\Phi_1 \to U_0 \Phi_1 U_1^\dagger, \tag{4.1}$$

$$\Phi_2 \to U_2 \Phi_2 U_1^\dagger, \tag{4.2}$$

where U_j's are two-by-two unitary matrices of the $\mathrm{SU}(2)_j$ gauge transformation. To reduce the number of degrees of freedom, we impose

$$\Phi_j = -\epsilon \Phi_j^* \epsilon, \quad \text{where} \quad \epsilon = \begin{pmatrix} 0 & 1 \\ -1 & 0 \end{pmatrix}. \tag{4.3}$$

Before imposing this constraint, Φ_1 and Φ_2 contain four complex degrees of freedom (eight real degrees of freedom), respectively. After imposing this constraint, each field has four real degrees of freedom as shown later in Eq. (4.14). This constraint has nothing to do with the dark matter stability.

We impose the following discrete symmetry.

$$q_L \to q_L, \quad u_R \to u_R, \quad d_R \to d_R, \tag{4.4}$$

$$\ell_L \to \ell_L, \quad e_R \to e_R, \tag{4.5}$$

$$H \to H, \quad \Phi_1 \to \Phi_2, \quad \Phi_2 \to \Phi_1, \tag{4.6}$$

$$W^a_{0\mu} \to W^a_{2\mu}, \quad W^a_{1\mu} \to W^a_{1\mu}, \quad W^a_{2\mu} \to W^a_{0\mu}. \tag{4.7}$$

This discrete symmetry is equivalent to the exchange of $\mathrm{SU}(2)_0$ and $\mathrm{SU}(2)_2$. It requires $g_0 = g_2$. The symmetry works as a Z_2 symmetry that is utilized in many dark matter

[1] A model with a similar gauge group is studied in [79] but with different matter contents and with different gauge charge assignments.

field	spin	$SU(3)_c$	$SU(2)_0$	$SU(2)_1$	$SU(2)_2$	$U(1)_Y$
q_L	$\frac{1}{2}$	3	1	2	1	$\frac{1}{6}$
u_R	$\frac{1}{2}$	3	1	1	1	$\frac{2}{3}$
d_R	$\frac{1}{2}$	3	1	1	1	-$\frac{1}{3}$
ℓ_L	$\frac{1}{2}$	1	1	2	1	-$\frac{1}{2}$
e_R	$\frac{1}{2}$	1	1	1	1	-1
H	0	1	1	2	1	$\frac{1}{2}$
Φ_1	0	1	2	2	1	0
Φ_2	0	1	1	2	2	0

Table 5: The matter and Higgs fields and their gauge charges in the model. The generation indices for the matter fields are implicit.

models. Linear combinations $(W^a_{0\mu} - W^a_{2\mu})/\sqrt{2}$ are odd under the symmetry. They are mass eigenstates as we will see below, and one of them is a DM candidate. On the other hand, the other linear combinations of the gauge fields are even under the symmetry. Similarly, linear combinations of Φ_1 and Φ_2 divide scalar fields into the odd and even sectors. All the SM particles are even under the discrete symmetry.

The discrete symmetry under exchanging $SU(2)_0$ and $SU(2)_2$ is inspired by the deconstruction [80, 81] of models in extra dimension on S^1/Z_2. Using the deconstruction approach, such models are expressed by moose diagrams [82]. The Z_2 symmetry is realized by identifying two sites. Some models with the gauge symmetry $G = SU(2)_0 \times SU(2)_1 \times \cdots \times SU(2)_{2N}$ with identifying $SU(2)_j$ and $SU(2)_{2N-j}$ are equivalent to the models in extra dimension on S^1/Z_2 upto $2N$ Kaluza-Klein (KK) modes. The SU(2) sector in our model corresponds to the case for $N = 1$. The similar approach was taken in studying a U(1) vector dark matter model [10].

Under this setup, we can write the Yukawa interaction terms as

$$-y_u \bar{q}_L \tilde{H} u_R - y_d \bar{q}_L H d_R - y_e \bar{\ell}_L H e_R + (h.c.), \tag{4.8}$$

where $\tilde{H} = \epsilon H^*$. The gauge symmetry forbids Φ_1 and Φ_2 to couple to the fermions, and only H is the relevant Higgs field for the Yukawa interaction terms. This Yukawa sector is as simple as one in the SM, and we do not need to extend the fermion sector. This is a reason why we add two extra SU(2) gauge symmetries into the SM. If we added only one extra SU(2), there would be two possibilities. One possibility is that the extra SU(2) is isolated and does not mix with the $SU(2)_L$ gauge field. In this case, the dark SU(2) gauge bosons do not couple to the SM weak gauge bosons, and the model is the Higgs portal type. This is not our concern. The other possibility is to mix the extra SU(2) gauge field with the SU(2) gauge field in the SM. It is expected by the mixing that the dark SU(2) gauge bosons couple to the SM weak gauge bosons. In this case, however, we need an exchanging symmetry under these two SU(2) gauge field to stabilize the dark matter. Since the SM left-handed fermions feel $SU(2)_L$ gauge symmetry, the symmetry exchanging the two SU(2) fields requires two types of the fermions; one is the

doublet fields under an SU(2), the others are doublet under the other SU(2). Some linear combinations of them are the SM left-handed fermions, and the other linear combinations are extra fermions. Therefore, if we add only one extra SU(2), then the symmetry to stabilize the dark matter requires to double the fermion fields compared to the SM. On the other hand, by considering two extra SU(2) gauge symmetries, we can realize the simple Yukawa interaction terms without extending the fermion sector as in Eq. (4.8). This is a distinctive feature of this model from other SU(2) dark matter models.

4.1 Bosonic sector

We briefly describe the electroweak sector and the related scalar sector. More details are discussed in Appendices. The Lagrangian for those two sectors is given by

$$\begin{aligned}\mathcal{L} \supset & -\frac{1}{4}B_{\mu\nu}B^{\mu\nu} - \sum_{j=0}^{2}\sum_{a=1}^{3}\frac{1}{4}W_{j\mu\nu}^{a}W_{j}^{a\mu\nu} \\ & + D_\mu H^\dagger D^\mu H + \frac{1}{2}\mathrm{tr}D_\mu\Phi_1^\dagger D^\mu\Phi_1 + \frac{1}{2}\mathrm{tr}D_\mu\Phi_2^\dagger D^\mu\Phi_2 \\ & - V_{\mathrm{scalar}}, \end{aligned} \tag{4.9}$$

where the covariant derivatives of Φ_j are given by

$$D_\mu\Phi_1 = \partial_\mu\Phi_1 - ig_0W_{0\mu}^{a}T^a\Phi_1 + ig_1\Phi_1W_{1\mu}^{a}T^a, \tag{4.10}$$

$$D_\mu\Phi_2 = \partial_\mu\Phi_2 - ig_0W_{2\mu}^{a}T^a\Phi_2 + ig_1\Phi_2W_{1\mu}^{a}T^a, \tag{4.11}$$

and the potential is given by

$$\begin{aligned}V_{\mathrm{scalar}} =& m^2H^\dagger H + m_\Phi^2\mathrm{tr}\left(\Phi_1^\dagger\Phi_1\right) + m_\Phi^2\mathrm{tr}\left(\Phi_2^\dagger\Phi_2\right) \\ & + \lambda(H^\dagger H)^2 + \lambda_\Phi\left(\mathrm{tr}\left(\Phi_1^\dagger\Phi_1\right)\right)^2 + \lambda_\Phi\left(\mathrm{tr}\left(\Phi_2^\dagger\Phi_2\right)\right)^2 \\ & + \lambda_{h\Phi}H^\dagger H\mathrm{tr}\left(\Phi_1^\dagger\Phi_1\right) + \lambda_{h\Phi}H^\dagger H\mathrm{tr}\left(\Phi_2^\dagger\Phi_2\right) + \lambda_{12}\mathrm{tr}\left(\Phi_1^\dagger\Phi_1\right)\mathrm{tr}\left(\Phi_2^\dagger\Phi_2\right). \end{aligned} \tag{4.12}$$

Some coupling constants in the Higgs potential are common because of the discrete symmetry. We assume that the Higgs fields obtain the following vacuum expectation values at the global minimum.

$$\langle H\rangle = \begin{pmatrix} 0 \\ \frac{v}{\sqrt{2}} \end{pmatrix}, \quad \langle\Phi_1\rangle = \langle\Phi_2\rangle = \frac{1}{\sqrt{2}}\begin{pmatrix} v_\Phi & 0 \\ 0 & v_\Phi \end{pmatrix}. \tag{4.13}$$

Three SU(2) symmetries are broken to one mixed SU(2) symmetry because of the VEV of Φ_j. This mixing makes our dark matter have the electroweak interaction. The remained SU(2) and $\mathrm{U}(1)_Y$ symmetries are broken to $\mathrm{U}(1)_{\mathrm{EM}}$ because of the VEV of H. This is similar to the electroweak symmetry breaking in the SM. The component fields of these Higgs fields at this vacuum are given by

$$H = \begin{pmatrix} i\pi_3^+ \\ \frac{v+\sigma_3-i\pi_3^0}{\sqrt{2}} \end{pmatrix}, \quad \Phi_j = \begin{pmatrix} \frac{v_\Phi+\sigma_j+i\pi_j^0}{\sqrt{2}} & i\pi_j^+ \\ i\pi_j^- & \frac{v_\Phi+\sigma_j-i\pi_j^0}{\sqrt{2}} \end{pmatrix}. \tag{4.14}$$

From the stationary condition, we find

$$m^2 = -\lambda v^2 - 2\lambda_{h\Phi} v_\Phi^2, \tag{4.15}$$

$$m_\Phi^2 = -\frac{\lambda_{h\Phi}}{2} v^2 - (\lambda_{12} + 2\lambda_\Phi) v_\Phi^2. \tag{4.16}$$

4.2 Gauge sector

After the electroweak symmetry breaking, the gauge boson mass terms come from the kinetic terms of Higgs bosons and are given by

$$\begin{pmatrix} W_{0\mu}^+ & W_{1\mu}^+ & W_{2\mu}^+ \end{pmatrix} \mathcal{M}_C^2 \begin{pmatrix} W_0^{-\mu} \\ W_1^{-\mu} \\ W_2^{-\mu} \end{pmatrix} + \frac{1}{2} \begin{pmatrix} W_{0\mu}^3 & W_{1\mu}^3 & W_{2\mu}^3 & B_\mu \end{pmatrix} \mathcal{M}_N^2 \begin{pmatrix} W_0^{3\mu} \\ W_1^{3\mu} \\ W_2^{3\mu} \\ B^\mu \end{pmatrix}, \tag{4.17}$$

where

$$\mathcal{M}_C^2 = \frac{1}{4} \begin{pmatrix} g_0^2 v_\Phi^2 & -g_0 g_1 v_\Phi^2 & 0 \\ -g_0 g_1 v_\Phi^2 & g_1^2 (v^2 + 2 v_\Phi^2) & -g_1 g_0 v_\Phi^2 \\ 0 & -g_1 g_0 v_\Phi^2 & g_0^2 v_\Phi^2 \end{pmatrix}, \tag{4.18}$$

$$\mathcal{M}_N^2 = \frac{1}{4} \begin{pmatrix} g_0^2 v_\Phi^2 & -g_0 g_1 v_\Phi^2 & 0 & 0 \\ -g_0 g_1 v_\Phi^2 & g_1^2 (v^2 + 2 v_\Phi^2) & -g_1 g_0 v_\Phi^2 & -g_1 g' v^2 \\ 0 & -g_1 g_0 v_\Phi^2 & g_0^2 v_\Phi^2 & 0 \\ 0 & -g_1 g' v^2 & 0 & g'^2 v^2 \end{pmatrix}. \tag{4.19}$$

After diagonalizing these mass matrices, we find the following mass eigenstates,

$$\gamma, W^\pm, Z,\ V^0, V^\pm,\ W'^\pm,\ Z', \tag{4.20}$$

where γ, $W^\pm$, and Z are identified as the SM electroweak gauge bosons. V^0 and $V^\pm$ are odd under the discrete symmetry and are given by

$$V^0 = \frac{W_{0\mu}^3 - W_{2\mu}^3}{\sqrt{2}}, \tag{4.21}$$

$$V^\pm = \frac{W_{0\mu}^\pm - W_{2\mu}^\pm}{\sqrt{2}}. \tag{4.22}$$

The details, such as linear combinations for other gauge fields, are discussed in Appendix A.1.

The masses of dark matter V^0 and its charged partner $V^\pm$ are given by

$$m_{V^\pm}^2 = m_{V^0}^2 = \frac{g_0^2 v_\Phi^2}{4} \equiv m_V^2, \tag{4.23}$$

at the tree level. At the loop level, the mass difference is generated, and $m_{V^\pm}$ becomes slightly heavier than m_{V^0} as we discuss in Sec. 6.1. Therefore, V^0 is a dark matter candidate in our model.

The other gauge boson masses are complicated as shown in Appendix.A.1. To understand the mass spectrum of these particles, we consider the limit of $v_\Phi \gg v$ which is required to obtain the observed relic abundance as we will discuss in Sec.6.3. In this limit, we get neutral gauge boson masses,

$$m_Z^2 \simeq \frac{1}{4}(g_W^2 + g'^2)v^2, \tag{4.24}$$

$$m_{Z'}^2 \simeq \frac{1}{4}(g_0^2 + 2g_1^2)v_\Phi^2, \tag{4.25}$$

and charged gauge boson masses,

$$m_W^2 \simeq \frac{1}{4}g_W^2 v^2, \tag{4.26}$$

$$m_{W'}^2 \simeq \frac{1}{4}(g_0^2 + 2g_1^2)v_\Phi^2, \tag{4.27}$$

where we introduce g_W as

$$g_W \equiv \left(\frac{2}{g_0^2} + \frac{1}{g_1^2}\right)^{-1/2} = \sqrt{\frac{g_0^2 g_1^2}{g_0^2 + 2g_1^2}}. \tag{4.28}$$

We find $g_W \simeq 0.65$ for $v_\Phi \gg v$ numerically, namely g_W is approximately the $\mathrm{SU}(2)_L$ gauge coupling in the SM. So we can obtain right masses for $W^\pm$ and Z bosons in this limit. The heavy gauge bosons, W' and Z' have nearly same masses, $m_{Z'} \simeq m_{W'}$, since they are components of the triplet under the mixed SU(2) symmetry. We also obtain the relations between V and Z' as

$$\frac{m_{Z'}^2}{m_V^2} \simeq 1 + \frac{2g_1^2}{g_0^2}. \tag{4.29}$$

so that $m_{Z'} > m_V$. Since Z' has a contribution from the $\mathrm{SU}(2)_1$ symmetry unlike V, Z' is heavier than V.

4.3 Physical scalars

There are 12 scalars in the model, and 9 of them are would-be NG bosons. The three remaining neutral scalars are physical, and their mass terms are given by

$$\mathcal{L} \supset \frac{1}{2}\begin{pmatrix}\sigma_3 & \sigma_1 & \sigma_2\end{pmatrix}\begin{pmatrix} 2\lambda v^2 & 2vv_\Phi\lambda_{h\Phi} & 2vv_\Phi\lambda_{h\Phi} \\ 2vv_\Phi\lambda_{h\Phi} & 8v_\Phi^2\lambda_\Phi & 4v_\Phi^2\lambda_{12} \\ 2vv_\Phi\lambda_{h\Phi} & 4v_\Phi^2\lambda_{12} & 8v_\Phi^2\lambda_\Phi \end{pmatrix}\begin{pmatrix}\sigma_3 \\ \sigma_1 \\ \sigma_2\end{pmatrix}. \tag{4.30}$$

After diagonalizing this mass matrix, we obtain the mass eigenstates, h, h', and h_D, where h_D is odd under the discrete symmetry.

$$\begin{pmatrix}\sigma_3 \\ \sigma_1 \\ \sigma_2\end{pmatrix} = \begin{pmatrix} \cos\phi_h & -\sin\phi_h & 0 \\ \frac{1}{\sqrt{2}}\sin\phi_h & \frac{1}{\sqrt{2}}\cos\phi_h & \frac{1}{\sqrt{2}} \\ \frac{1}{\sqrt{2}}\sin\phi_h & \frac{1}{\sqrt{2}}\cos\phi_h & -\frac{1}{\sqrt{2}} \end{pmatrix}\begin{pmatrix} h \\ h' \\ h_D \end{pmatrix}. \tag{4.31}$$

The masses of higgs,h, h', h_D are given by

$$m_{h_D}^2 = 4(2\lambda_\Phi - \lambda_{12})v_\Phi^2, \tag{4.32}$$

$$m_h^2 = \lambda v^2 + 2(\lambda_{12} + 2\lambda_\Phi)v_\Phi^2 - \sqrt{\lambda^2 v^4 - 4(-2\lambda_{h\Phi}^2 + \lambda(\lambda_{12} + 2\lambda_\Phi))v^2 v_\Phi^2 + 4(\lambda_{12} + 2\lambda_\Phi)^2 v_\Phi^2}, \tag{4.33}$$

$$m_{h'}^2 = \lambda v^2 + 2(\lambda_{12} + 2\lambda_\Phi)v_\Phi^2 + \sqrt{\lambda^2 v^4 - 4(-2\lambda_{h\Phi}^2 + \lambda(\lambda_{12} + 2\lambda_\Phi))v^2 v_\Phi^2 + 4(\lambda_{12} + 2\lambda_\Phi)^2 v_\Phi^2}. \tag{4.34}$$

Using the fact, $\lambda_{12} + 2\lambda_\Phi > 0$, for $v_\Phi \gg v$

$$m_h^2 = 2\left(\lambda - \frac{\lambda_{h\Phi}}{\lambda_{12} + 2\lambda_\Phi}\right)v^2 + \mathcal{O}\left(\frac{v^2}{v_\Phi^2}\right), \tag{4.35}$$

$$m_{h'}^2 = 4(2\lambda_\Phi + \lambda_{12})v_\Phi^2 + \frac{2\lambda_{h\Phi}^2}{\lambda_{12} + 2\lambda_\Phi}v^2 + \mathcal{O}\left(\frac{v^2}{v_\Phi^2}\right). \tag{4.36}$$

For the gauge sector, we obtain the condition, $m_{Z'} > m_V$. However we can't decide theoretically which mass is greater h_D or h'. [2] If we choose the mass eigenvalues and the mixing angle $(m_h, m_{h'}, m_{h_D}, \phi_h)$ as input parameters, then the quartic couplings in the Higgs potential are given by

$$\lambda = \frac{m_h^2 \cos^2\phi_h + m_{h'}^2 \sin^2\phi_h}{2v^2}, \tag{4.37}$$

$$\lambda_{h\Phi} = -\frac{\sin\phi_h \cos\phi_h}{2\sqrt{2}vv_\Phi}(m_{h'}^2 - m_h^2), \tag{4.38}$$

$$\lambda_\Phi = \frac{m_h^2 \sin^2\phi_h + m_{h'}^2 \cos^2\phi_h + m_{h_D}^2}{16v_\Phi^2}, \tag{4.39}$$

$$\lambda_{12} = \frac{m_h^2 \sin^2\phi_h + m_{h'}^2 \cos^2\phi_h - m_{h_D}^2}{8v_\Phi^2}. \tag{4.40}$$

The quartic coupling of H, λ tends to be large value because this is not supplessed by v_Φ unlike the others. For $m_{h'} \gg m_h$ and $\phi_h \sim \mathcal{O}(0.1)$, the perturbative unitarity is not satisfied as we will show below.

4.4 Model parameters

The Lagrangian in the electroweak sector contains the following parameters.

$$\left(g_0,\ g_1,\ g',\ m^2,\ m_\Phi^2,\ \lambda,\ \lambda_\Phi,\ \lambda_{h\Phi}, \lambda_{12}\right). \tag{4.41}$$

Instead of them, we can use the following parameters as inputs,

$$\left(e,\ m_Z,\ v,\ m_h,\ m_{Z'},\ m_V,\ m_{h'},\ m_{h_D}, \phi_h\right), \tag{4.42}$$

[2] In a rough discussion, the higgs sector has more free parameters than the gauge sector so that the conditions of masses are loosened.

where e is the QED coupling constant,

$$e = \left(\frac{1}{g_W^2} + \frac{1}{g'^2}\right)^{-1/2} = \frac{g_W^2 g'^2}{g_W^2 + g'^2}, \tag{4.43}$$

and v is related to the Fermi constant as

$$v = \left(\sqrt{2} G_F\right)^{-1/2}. \tag{4.44}$$

The first four parameters are already measured, and thus we have five free parameters in this model. The relation between the gauge couplings and the masses of the gauge bosons is discussed in Appendix A.1. The derivation of Eq. (4.44) is discussed in Appendix A.3.

Using g_W, $m_{Z'}$, and m_V, we can obtain g_0 and g_1 in the $v_\Phi \gg v$ limit as

$$g_0 \simeq \sqrt{2} g_W \frac{m_{Z'}}{m_V} \frac{1}{\sqrt{\frac{m_{Z'}^2}{m_V^2} - 1}}, \tag{4.45}$$

$$g_1 \simeq g_W \frac{m_{Z'}}{m_V}. \tag{4.46}$$

If the mass difference between m_V and $m_{Z'}$ is very small, g_0 become very large. Conversely, if the mass difference is very large, g_1 become large value. We will consider the perturbative unitarity conditions on these gauge couplings in the next section.

The gauge boson couplings to the fermions are given by

$$g_{W u_L d_L} = g_{W \ell_L \nu_L} (\equiv g_{W f_L f_L}) \simeq g_W, \tag{4.47}$$

$$g_{W' u_L d_L} = g_{W' \ell_L \nu_L} (\equiv g_{W' f_L f_L}) \simeq - g_W \sqrt{\frac{m_{Z'}^2}{m_V^2} - 1}, \tag{4.48}$$

$$g_{Z q_L q_L} = g_{Z \ell_L \ell_L} = g_{Z \nu_L \nu_L} \simeq \frac{e}{s_Z c_Z} \left(t^3 - s_Z^2 Q\right), \tag{4.49}$$

$$g_{Z' q_L q_L} = g_{Z' \nu_L \ell_L} = g_{Z' \nu_L \nu_L} \simeq - t^3 g_W \sqrt{\frac{m_{Z'}^2}{m_V^2} - 1}, \tag{4.50}$$

$$g_{Z q_R q_R} = g_{Z \ell_R \ell_R} = g_{Z \nu_R \nu_R} \simeq - \frac{e s_Z}{c_Z} Q, \tag{4.51}$$

$$g_{Z' q_R q_R} = g_{Z' \ell_R \ell_R} = g_{Z' \nu_R \nu_R} = \mathcal{O}\left(\frac{v^2}{v_\Phi^2}\right), \tag{4.52}$$

where $t^3 = \frac{1}{2}\left(-\frac{1}{2}\right)$ for up-type (down-type) fermions, Q is the QED charge of the fermions, $c_Z = \sqrt{1 - s_Z^2}$, and s_Z is given as a solution of

$$s_Z^2 c_Z^2 = \frac{v^2 e^2}{4 m_Z^2}. \tag{4.53}$$

We can see that the W' and Z' couplings to the SM fermions are controlled by the mass ratio of Z' and V. If $m_{Z'}$ and m_V are degenerated, then those couplings are suppressed

while g_0 becomes very large. Therefore, we expect that the values of W' and Z' couplings to the SM fermions are comparable to those of the W couplings in the region where perturbation works. We discuss this point further in Sec. 5.2.

Using g_W and the masses of the gauge bosons, we find that the triple gauge couplings are given by

$$g_{WWZ} \simeq g_{W'W'Z} \simeq g_{V^-V^+Z} \simeq g_W \frac{m_W}{m_Z} \simeq g_{WWZ}^{\rm SM}, \tag{4.54}$$

$$g_{WWZ'} \simeq g_W \frac{m_W^2}{m_{Z'}^2} \sqrt{\frac{m_{Z'}^2}{m_V^2} - 1}, \tag{4.55}$$

$$g_{WW'Z} \simeq g_W \frac{m_W m_Z}{m_{W'}^2} \sqrt{\frac{m_{Z'}^2}{m_V^2} - 1}, \tag{4.56}$$

$$g_{W'W'Z'} \simeq g_W \frac{1}{\sqrt{\frac{m_{Z'}^2}{m_V^2} - 1}} \left(2 - \frac{m_{Z'}^2}{m_V^2}\right), \tag{4.57}$$

$$g_{WW'Z'} = g_{W^+V^-V^0} = g_{W^-V^+V^0} \simeq g_W, \tag{4.58}$$

$$g_{V^-W'^+V^0} = g_{W'^-V^+V^0} \simeq g_{V^-V^+Z'} \simeq g_W \frac{1}{\sqrt{\frac{m_{Z'}^2}{m_V^2} - 1}}. \tag{4.59}$$

We emphasize that V^0 and $V^\pm$ couple to W and Z without any suppression factors, see Eqs. (4.54) and (4.58). Therefore, DM pairs can annihilate into the SM gauge bosons through these couplings, $g_{V^-V^+Z}$ and $g_{W^\pm V^\mp V^0}$. This is a distinctive feature of our vector DM model.

Couplings of physical scalar bosons to the gauge bosons are

$$g_{WWh} \simeq \frac{2m_W^2}{v} \cos\phi_h \simeq g_{WWh}^{\rm SM} \cos\phi_h, \tag{4.60}$$

$$g_{WW'h} \simeq \frac{2m_W^2}{v} \left(-\cos\phi_h \sqrt{\frac{m_{Z'}^2}{m_V^2} - 1} + \frac{m_W}{m_V} \frac{m_{Z'}}{m_V} \sin\phi_h \right), \tag{4.61}$$

$$g_{ZZh} \simeq \frac{2m_Z^2}{v} \cos\phi_h \simeq g_{ZZh}^{\rm SM} \cos\phi_h, \tag{4.62}$$

$$g_{ZZ'h} \simeq \frac{2m_W m_Z}{v} \left(-\cos\phi_h \sqrt{\frac{m_{Z'}^2}{m_V^2} - 1} + \frac{m_W}{m_V} \frac{m_{Z'}}{m_V} \sin\phi_h \right), \tag{4.63}$$

$$g_{V^0V^0h} \simeq g_{V^+V^-h} \simeq \frac{g_W m_{Z'}}{\sqrt{\frac{m_{Z'}^2}{m_V^2} - 1}} \sin\phi_h, \tag{4.64}$$

$$g_{V^0V^0h'} \simeq g_{V^+V^-h'} \simeq \frac{g_W m_{Z'}}{\sqrt{\frac{m_{Z'}^2}{m_V^2} - 1}} \cos\phi_h. \tag{4.65}$$

Note that g_{WWh} is the same as the SM prediction for $\cos\phi_h = 1$. This g_{WWh} coupling is already measured by the ATLAS and CMS experiments, and the measured value is

consistent with the SM value. Accordingly, we take small ϕ_h in the following analysis. For a small ϕ_h limit, the V^0 coupling to h is suppressed. However, as we mentioned already, the annihilation processes of DM pairs into the SM particles do not need to rely on the DM-Higgs coupling. Therefore, we can obtain the right amount of DM energy density even if we take small $|\phi_h|$.

Chapter 5

Constraints

5.1 Perturbative unitarity

We obtain the constraints on g_0, g_1, and scalar quartic couplings from the perturbative unitarity conditions for two-particle scattering processes in the high energy regime.

First, we consider two-to-two scalar bosons scattering processes in the high energy limit and derive the constraints on the scalar quartic couplings. In our derivation, we assume that these quartic couplings are much larger than the other couplings, such as gauge couplings. This model contains 12 scalars and there are 76 two scalar particle channels. We obtain the following conditions.

$$|\lambda| \leq 4\pi, \tag{5.1}$$
$$|\lambda_{h\Phi}| \leq 4\pi, \tag{5.2}$$
$$|\lambda_{\Phi}| \leq \pi, \tag{5.3}$$
$$|\lambda_{12}| \leq 2\pi, \tag{5.4}$$
$$|3\lambda_{\Phi} - \lambda_{12}| \leq \pi, \tag{5.5}$$
$$\left|3\lambda + 4(3\lambda_{\Phi} + \lambda_{12}) \pm \sqrt{\left(3\lambda - 4(3\lambda_{\Phi} + \lambda_{12})\right)^2 + 32\lambda_{h\Phi}^2}\right| \leq 8\pi. \tag{5.6}$$

As we discussed in Sec.4.3, λ can be larger than the other scalar quartic couplings. If we ignore them, we obtain the unitarity bound on λ from Eq.(5.6) with + sign.

$$|\lambda| \lesssim \frac{4\pi}{3}. \tag{5.7}$$

This is stronger than Eq.(5.1). λ depends on the $m_{h'}$ and ϕ_h, hence the values of λ in the $m_{h'}$-ϕ_h plane are shown in Fig.8. We find that large values of $m_{h'}$ and ϕ_h are constrained by the perturbative unitarity.

Second, we can derive the upper bounds on the gauge couplings from vector-vector to scalar-scalar scattering processes. In our model, one of g_0 and g_1 can be larger than the other in most of the region of the parameter space, and thus the result in Ref. [83] is

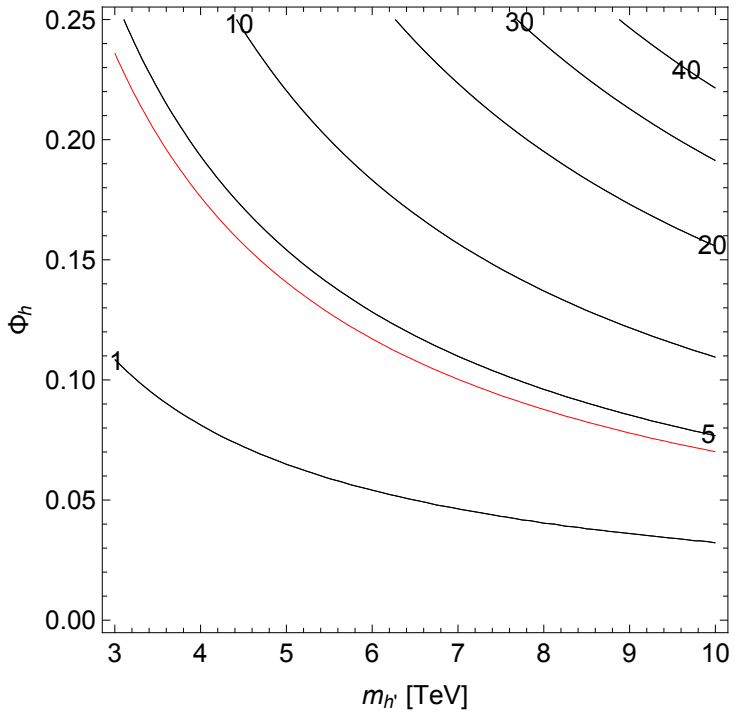

Figure 8: The contour show the value of λ in the $m_{h'}$-ϕ_h plane. Red line show the contour for $\lambda = 4\pi/3$.

applicable. We find that

$$g_j < \sqrt{\frac{16\pi}{\sqrt{6}}} \simeq 4.53. \quad (j = 0, 1) \tag{5.8}$$

The gauge couplings depend on the mass ratio of Z' and V, $m_{Z'}/m_V$, as in Eqs.(4.45) and (4.46). g_1 is proportional to this mass ratio. g_0 has a pole at $m_{Z'}/m_V = 1$ and nearly constant in the $m_{Z'}^2/m_V^2 \gg 1$ limit. Fig. 9 shows g_0 and g_1 plotted as a function of the mass ratio. We find that when the mass difference is very small($m_{Z'} < 1.02 m_V$), g_0 is non-perturbative. Conversely, when the mass difference is very large($m_{Z'} > 6.97 m_V$), g_1 is non-perturbative.

5.2 The mass ratio of Z' and V

We find in Sec. 4.4 that the mass ratio of Z' and V is important to determine the model parameters and couplings. Although the mass ratio is a free parameter, there is a viable range.

It can be seen from Eq. (4.45) that g_0 becomes very large for $m_{Z'} \sim m_V$, and we can not treat g_0 as a small perturbation. For $m_{Z'} \gg m_V$, we can see from Eqs. (4.46) and (4.48) that g_1 and $g_{W' f_L f_L}$ become large. This is also bad for the perturbative calculation. Moreover, the decay widths of W' and Z' become larger for the larger $g_{W' f_L f_L}$.

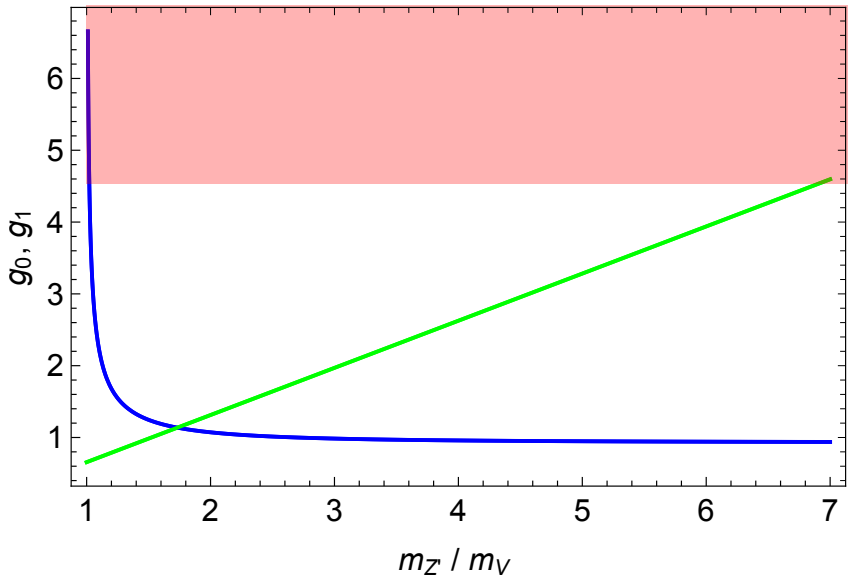

Figure 9: The blue (green) line shows the value of g_0 (g_1) as a function of the mass ratio, $m_{Z'}/m_V$. The red shaded region ($g_i > 4.53$) is constrained by the perturbative unitarity.

For $v_\Phi \gg v$ and $|\phi| \ll 1$, we find

$$\Gamma(W' \to f\bar{f}) \simeq \frac{N_c}{48\pi} m_{W'} g^2_{W f_L f_L} \left(\frac{m^2_{Z'}}{m^2_V} - 1 \right), \tag{5.9}$$

$$\Gamma(W' \to WZ) \simeq \frac{1}{192\pi} m_{W'} g^2_{W f_L f_L} \left(\frac{m^2_{Z'}}{m^2_V} - 1 \right), \tag{5.10}$$

$$\Gamma(W' \to Wh) \simeq \frac{1}{192\pi} m_{W'} g^2_{W f_L f_L} \left(\frac{m^2_{Z'}}{m^2_V} - 1 \right), \tag{5.11}$$

where $N_c = 3$ for quarks and 1 for leptons. Here we take $V_{CKM} = 1$ for simplicity. If W' cannot decay into the non-SM particles kinematically, then the total width of W' is given by

$$\Gamma_{W'} \simeq m_{W'} \frac{25}{96\pi} g^2_W \left(\frac{m^2_{Z'}}{m^2_V} - 1 \right). \tag{5.12}$$

We show some values of g_0, g_1, $\Gamma_{W'}/m_{W'}$, and $|g_{W' f_L f_L}/g_{W f_L f_L}|$ for given ratios of $m_{Z'}$ and m_V in Tab. 6. We find that we cannot treat g_0 as a small perturbation for $m_{Z'} \simeq m_V$. We obtain a lower bound on the ratio of masses of Z' and V as $m_{Z'}/m_V \gtrsim 1.02$ from the perturbativity condition for g_0 shown in Eq. (5.8). Similarly, the perturbativity for g_1 gives an upper bound on $m_{Z'}/m_V$. We find $m_{Z'}/m_V < 6.97$. The total width also gives an upper bound on $m_{Z'}/m_V$ because the total width is proportional to the imaginary part of the one-loop diagrams while the mass is at the tree level. Therefore, our calculation based on the perturbation is valid only for the region where $m_{W'} > \Gamma_{W'}$. This gives the upper bound on $m_{Z'}$ for a given value of m_V, and we find that $m_{Z'} < 5.45 m_V$. We also find that $\Gamma_{W'}/m_{W'} < 0.1$ is satisfied for $m_{W'} \lesssim 2 m_V$.

$m_{Z'}/m_V$	g_0	g_1	$\Gamma_{W'}/m_{W'}$	$\lvert g_{W'f_Lf_L}/g_{Wf_Lf_L}\rvert$
1.02	4.53	0.661	0.00148	0.207
1.05	3	0.680	0.00358	0.321
$\sqrt{2}$	1.30	0.916	0.0348	1
4.63	0.938	3	0.711	4.52
5.45	0.932	3.53	1	5.36
6.97	0.93	4.53	1.66	6.90

Table 6: The values of g_0, g_1, $\Gamma_{W'}/m_{W'}$, and $g_{W'f_Lf_L}/g_{Wf_Lf_L}$ given ratios of $m_{Z'}$ and m_V.

5.3 W' and Z' searches at the LHC

New heavy vector bosons are being searched by the ATLAS and CMS experiments. Our model predicts the heavy vector bosons, W' and Z', and they couple to the SM particles. The W' and Z' couplings to SM particles are determined by the ratio of $m_{Z'}$ and m_V as discussed in Sec. 4.4. The couplings to the fermions and the SM vector bosons can be as large as the $SU(2)_L$ gauge coupling in the SM, and the former is larger than the latter. Therefore, the main production process of W' and Z' at the LHC is $q\bar{q} \to W'/Z'$. The branching fraction to two fermions is larger than two bosons, see Eqs.(5.9)–(5.11). Therefore, the main search channel of W' and Z' are $pp \to W' \to \ell\nu$ and $pp \to Z' \to \ell\ell$. The former gives the stronger constraint on the mass of W', and we focus on that process here.

The ATLAS experiment searches the $pp \to W' \to \ell\nu$ process and finds the lower bound on $m_{W'}$ as 6 TeV for the Sequential Standard Model (SSM) [84].[1] The W' couplings to the SM fermions in our model are different from those in the SSM. We recast the bound and obtain the lower bound on $m_{W'}$ for a given coupling ratio of $g_{W'f_Lf_L}$ and $g_{Wf_Lf_L}$. The result is shown in Fig. 10. Here we assume that the K factor is 1.3. We find that $m_{W'} \gtrsim 7$ TeV for $g_{W'f_Lf_L}/g_{Wf_Lf_L} \gtrsim 1.42$. Since the ATLAS experiment does not give the bound for $m_{W'} > 7$ TeV, we cannot obtain the bound on $m_{W'}$ for $g_{W'f_Lf_L}/g_{Wf_Lf_L} \gtrsim 1.42$. Similarly, we also recast the prospect of W' search at the ATLAS experiment with 14 TeV with 3000 fb^{-1} [86]. Other channels give weaker bound than this $\ell\nu$ channel.

5.4 Electroweak precision measurements

For $m_{W'/Z'} \gg m_{W/Z}$ limit, it is easy to obtain the electroweak precision parameters, $\hat{S}$, $\hat{T}$, W, and Y, introduced in [87]. At the tree level, we find that

$$\begin{aligned} &\hat{S} = \hat{T} = Y = 0, \\ &W = \frac{2g_1^2}{g_0^2 + 2g_1^2}\frac{m_W^2}{m_{W'}^2}. \simeq \left(1 - \frac{m_V^2}{m_{Z'}^2}\right)\frac{m_W^2}{m_{W'}^2}. \end{aligned} \tag{5.13}$$

[1]The CMS experiment also searches the same channel but gives a weaker bound on $m_{W'}$, $m_{W'} > 5.2$ TeV [85].

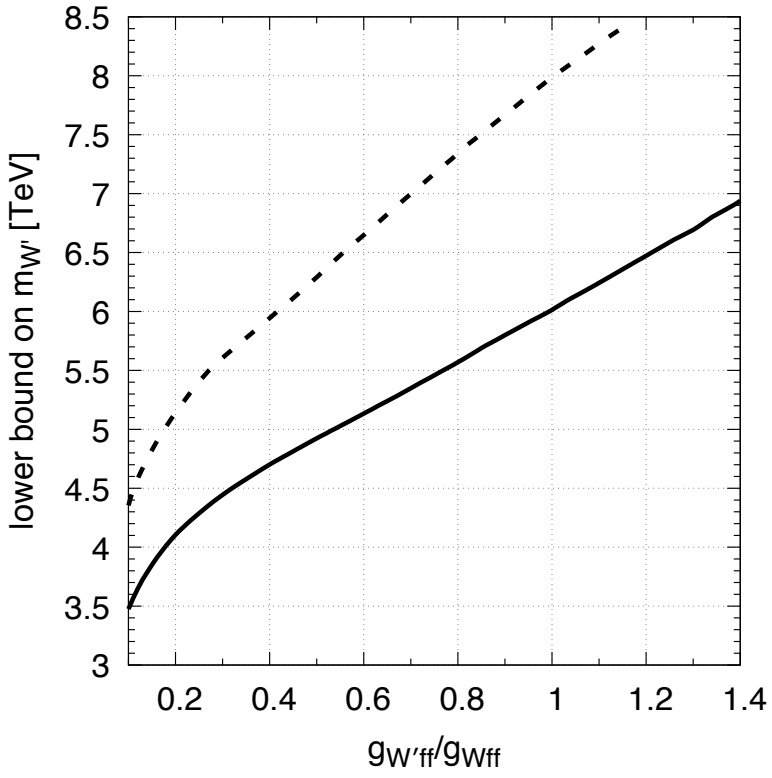

Figure 10: The solid curve shows the lower bound on $m_{W'}$ for a given $g_{W'f_Lf_L}$ coupling obtained by recasting the result in Ref. [84]. The dashed curve shows the prospect at the ATLAS experiment with 14 TeV with 3000 fb^{-1} [86].

The constraint is given as $W = (-0.3 \pm 0.6) \times 10^{-3}$. We find that this constraint is much weaker than the constraint from the W' search at the LHC experiment.

5.5 Higgs signal strength

Among the three scalar fields, only H contributes to the Yukawa interaction terms, and thus the h couplings to the fermions are equal to those in the SM times $\cos\phi_h$. As we have shown in Eq. (4.60), g_{WWh} for $v_\Phi \gg v$ is approximately given by the SM coupling times $\cos\phi_h$. Thus the Higgs signal strengths are given by

$$\kappa_F = \cos\phi_h, \quad \kappa_V \simeq \cos\phi_h. \tag{5.14}$$

We can constrain ϕ_h from the measurement of the Higgs couplings. We use the result from the ATLAS experiment [88],

$$\kappa_V = 1.05 \pm 0.04, \tag{5.15}$$

$$\kappa_F = 1.05 \pm 0.09, \tag{5.16}$$

with the linear correlation between them is observed as 44%, and obtain $|\phi_h| < 0.3$ in 2 σ level. We consider $0 \leq |\phi_h| < 0.3$ in the following discussions.

Chapter 6

DM phenomenology

6.1 Mass difference and its implication for collider physics

At the tree level, V^0 and $V^\pm$ have the same mass. However, the mass difference is generated at the loop level, and thus $V^\pm$ is slightly heavier than V^0. The mass difference is given by

$$\begin{aligned}\delta_{m_V} \equiv m_{V^\pm} - m_{V^0} =& \sqrt{m_V^2 + \Pi_{V^+V^-}(m_{V^\pm}^2)} - \sqrt{m_V^2 + \Pi_{V^0V^0}(m_{V^0}^2)} \\ \simeq& \frac{\Pi_{V^+V^-}(m_V^2) - \Pi_{V^0V^0}(m_V^2)}{2m_V},\end{aligned} \tag{6.1}$$

where $\Pi_{V^+V^-}$ and $\Pi_{V^0V^0}$ are the self-energies of $V^\pm$ and V^0, respectively. We calculate δ_{m_V} at the one-loop level by using `FormCalc` [89]. In $v_\Phi \gg v$ limit, we find

$$\delta_{m_V} \simeq \frac{m_W^3 G_F}{\sqrt{2}\pi}\left(1 - \frac{m_W}{m_Z}\right) \simeq 168 \text{ MeV}. \tag{6.2}$$

This result is consistent with the result in [90]. We have also checked it numerically by using `LoopTools` [89], without taking $v_\Phi \gg v$ limit.

This small mass difference is the same as the mass difference between the charged and neutral components of Wino ($\tilde{W}$) in the MSSM. Wino is $\mathrm{SU}(2)_L$ triplet fermions. The charged Wino decays into the neutral Wino, but its lifetime is long due to the small mass difference. Thus, Wino is being searched in the long-lived particle searches at the LHC. Our DM candidate, V^0, and its partner, $V^\pm$, has the same properties as the Wino. The decay rate of $V^\pm$ and the mass difference of $V^\pm$ and V^0 are exactly equal to those of Wino. Therefore, the long-lived particle search is also a useful tool to find $V^\pm$ in our model. The only difference of V from $\tilde{W}$ is the production rate of the charged particles. Figure 11 shows the production cross sections of $V^\pm$ and $\tilde{W}^\pm$ at the LHC with $\sqrt{s} = 13$ TeV. We find that the production cross section of $V^{\pm,0}$ depends on $m_{W'}$ and $m_{Z'}$ as well as m_V. It is also found that the production cross section of $V^{\pm,0}$ is smaller than the production cross section of Wino because of the interference between the diagrams exchanging W

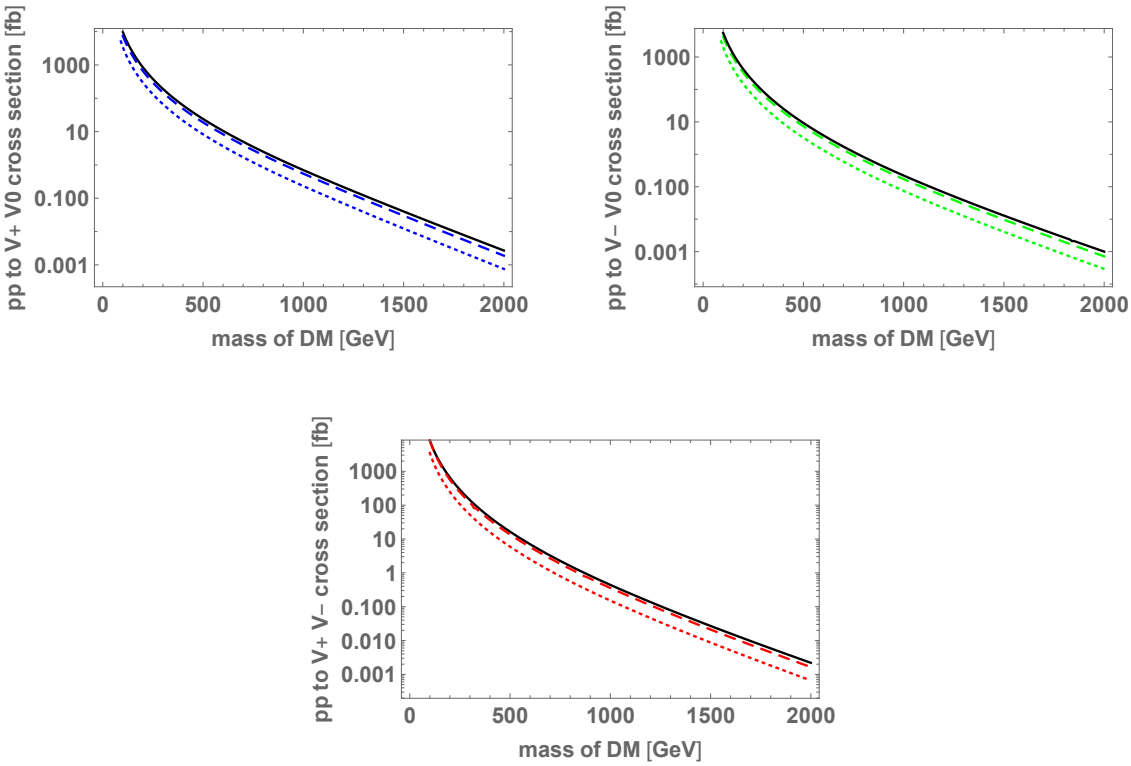

Figure 11: The production cross section of $V^{\pm}$ and $\tilde{W}^{\pm}$ from proton collisions at $\sqrt{s} = 13$ TeV. The left panel shows the cross section of $pp \to V^{+}V^{0}$, the right shows $pp \to V^{-}V^{0}$, and the bottom shows $pp \to V^{+}V^{-}$. In each figure, the black line shows the Wino production cross section and the dashed (dotted) line shows the $V^{\pm}$ for $m_{Z',W'} = 1.5m_V$ ($m_{Z',W'} = 1.3m_V$).

and W' (Z and Z') in the s-channel. Therefore, the constraint on m_V from the long-lived particle search is weaker than that on the Wino, $m_{\tilde{W}} \gtrsim 460$ GeV [91]. Once we require V^0 to explain the measured value of the DM energy density, then $m_V \gtrsim 3$ TeV is required as we will see in the following. Therefore, our model is consistent with the results of the long-lived search if the whole of DM in our universe is explained by V^0.

6.2 Direct detection

At the leading order, DM-nucleon scattering is mediated by two scalars, h and h', which are even under the discrete symmetry. Z boson mediated processes do not work at tree-level since the V^0-V^0-Z coupling is prohibited by the gauge symmetry. The spin-independent vector DM-nucleon scattering cross section is given by

$$\sigma_{\rm SI}^{N} = \frac{1}{\pi}\left(\frac{m_N}{m_N + m_V}\right)^2 |f_{NV}|^2, \tag{6.3}$$

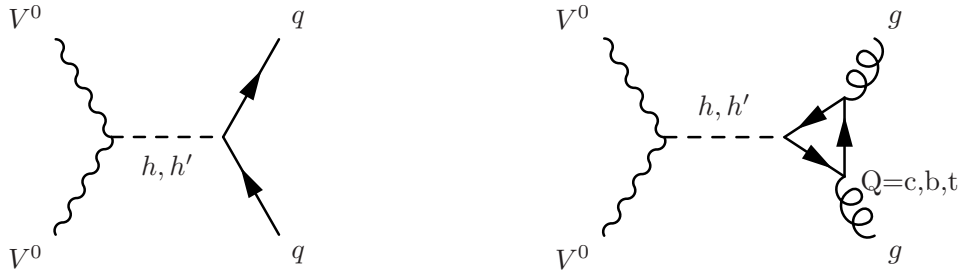

Figure 12: The leading diagrams mediated by h and h'.

where m_N is the nucleon mass ($N = p, n$) and f_{NV} is the effective coupling of DM-nucleon interactions.

Figure 12 shows the leading diagrams at the parton-level. The following Parton-level effective interactions are relevant to the DM-nucleon cross section,

$$\mathcal{L}^{\text{eff}} = \sum_{q=u,d,s} c_q V^{0\mu} V^0_\mu m_q \bar{q} q + \sum_{Q=c,b,t} c_Q V^{0\mu} V^0_\mu m_Q \bar{Q} Q, \tag{6.4}$$

where m_q and m_Q are light and heavy quark masses, respectively. The couplings, c_q and c_Q, in our model are

$$c_q = c_Q = \frac{m_V^2}{\sqrt{2} v v_\Phi} \sin\phi_h \cos\phi_h \left(\frac{1}{m_{h'}^2} - \frac{1}{m_h^2} \right). \tag{6.5}$$

To obtain the effective coupling of the DM-nucleon interactions, f_{NV}, we use the nucleon matrix elements,

$$\langle N | m_q \bar{q} q | N \rangle \equiv m_N f_{Tq}^{(N)}, \quad (q = u, d, s), \tag{6.6}$$

$$\langle N | \frac{\alpha_s}{\pi} G^a_{\mu\nu} G^{a\mu\nu} | N \rangle = -\frac{8}{9} m_N \left(1 - \sum_q f_{Tq}^{(N)} \right). \tag{6.7}$$

where $G^a_{\mu\nu}$ and α_s are the $\mathrm{SU}(3)_c$ field strength tensor and coupling constant, respectively. The numerical values of the mass fractions for the nucleon, $f_{Tq}^{(N)} (N = p, n)$, are obtained by lattice simulations, and we take the default values of `micrOMEGAs` [92].

$$\begin{aligned} f_{Tu}^p &= 0.0153, \ f_{Tu}^n = 0.011 \\ f_{Td}^p &= 0.0191, \ f_{Td}^n = 0.0273 \\ f_{Ts}^p &= f_{Ts}^n = 0.0447. \end{aligned} \tag{6.8}$$

For light quarks ($q = u, d, s$), we can obtain the contribution to the effective coupling f_{NV} using nucleon matrix elements of the mass operators. For the heavy quarks ($Q = c, b, t$), the leading contribution is loop diagrams (Fig. 12 right). The operator $m_Q \bar{Q} Q$ equals $-\frac{\alpha_s}{12\pi} G^a_{\mu\nu} G^{a\mu\nu}$ in the matrix element, so the matrix elements of the heavy quark mass operators are given by

$$\langle N | m_Q \bar{Q} Q | N \rangle = \frac{2}{27} m_N \left(1 - \sum_q f_{Tq}^{(N)} \right), \quad (Q = c, b, t). \tag{6.9}$$

Using these matrix elements, the effective coupling f_{NV} is given by

$$\begin{aligned}\frac{f_{NV}}{m_N} =& \sum_q c_q f_{Tq}^N + \frac{2}{27}\sum_Q c_Q(1-\sum_q f_{Tq}^N) \\ =& \frac{m_V^2}{\sqrt{2}vv_\Phi}\sin\phi_h\cos\phi_h\left(\frac{1}{m_{h'}^2}-\frac{1}{m_h^2}\right)\left(\frac{2}{9}+\frac{7}{9}\sum_q f_{Tq}^{(N)}\right). \end{aligned} \tag{6.10}$$

Finally, we obtain the spin-independent nucleon-vector DM cross section as follows.

$$\begin{aligned}\sigma_{\rm SI}^N =& \frac{1}{2\pi}\frac{m_N^4 m_V^4}{(m_N+m_V)^2}\frac{1}{v^2 v_\Phi^2}\sin^2\phi_h\cos^2\phi_h\left(\frac{1}{m_{h'}^2}-\frac{1}{m_h^2}\right)^2\left(\frac{2}{9}+\frac{7}{9}\sum_{q=u,d,s} f_{Tq}^N\right)^2 \\ \simeq& \frac{g_0^2}{32\pi v^2}\frac{m_N^4}{m_h^4}\sin^2(2\phi_h)\left(\frac{2}{9}+\frac{7}{9}\sum_{q=u,d,s} f_{Tq}^N\right)^2 \\ \simeq& 10^{-44}\times g_0^2\sin^2(2\phi_h)\ [\mathrm{cm}^2]. \end{aligned} \tag{6.11}$$

Here we assumed that $m_V \gg m_N$, and also $m_{h'} \gg m_h$ in the last two lines of Eq. (6.11). This cross section is proportional to $\sin^2(2\phi_h)$, and thus the large $|\phi_h|$ region is severely constrained from the direct detection experiments. The direct detection limit on the DM-nucleon cross section for TeV scale DM is around 10^{-45} cm^2 [3]. For $g_0 = 1$, we find $\phi_h \lesssim 0.15$. This upper bound can be stronger than the bound from the Higgs signal strength. If ϕ_h is smaller than ~ 0.01, the higher-order diagrams dominate in the DM-nucleon SI scattering process so that $\sigma_{\rm SI}^N \sim 10^{-47}$cm^2 [75, 93, 94].

6.3 Relic abundance

The model contains two DM candidates, V^0 and h_D. In this thesis, we treat V^0 as the DM candidate by assuming h_D is always heavier than V^0.

We calculate the thermal relic abundance of V^0 by using `micrOMEGAs` [92]. The model file is generated by `FeynRules` [95]. Since the mass difference of $V^\pm$ and V^0 is tiny, the coannihilation processes, which are automatically calculated in `micrOMEGAs`, are relevant. All the masses of the new particles are proportional to v_Φ, hence the large mass difference among the new particles requires large couplings. To avoid large couplings and to keep working within the perturbative regime, we keep the mass ratio of the new particles to the DM mass within $\mathcal{O}(1)$. However, the h' mass can be very light if $2\lambda_\Phi \sim -\lambda_{12}$. So we consider 2 cases, heavy and light h' in the following subsections.

6.3.1 heavy h' ($m_{h'} = 1.4m_V$)

Figure.13 shows the value of ϕ_h that is required to obtain the observed relic abundance in the m_V-$m_{Z'}$ plane. The other model parameters, $m_{h'}$ and m_{h_D}, are fixed as follows.

$$m_{h_D} = 1.2m_V, \quad m_{h'} = 1.4m_V. \tag{6.12}$$

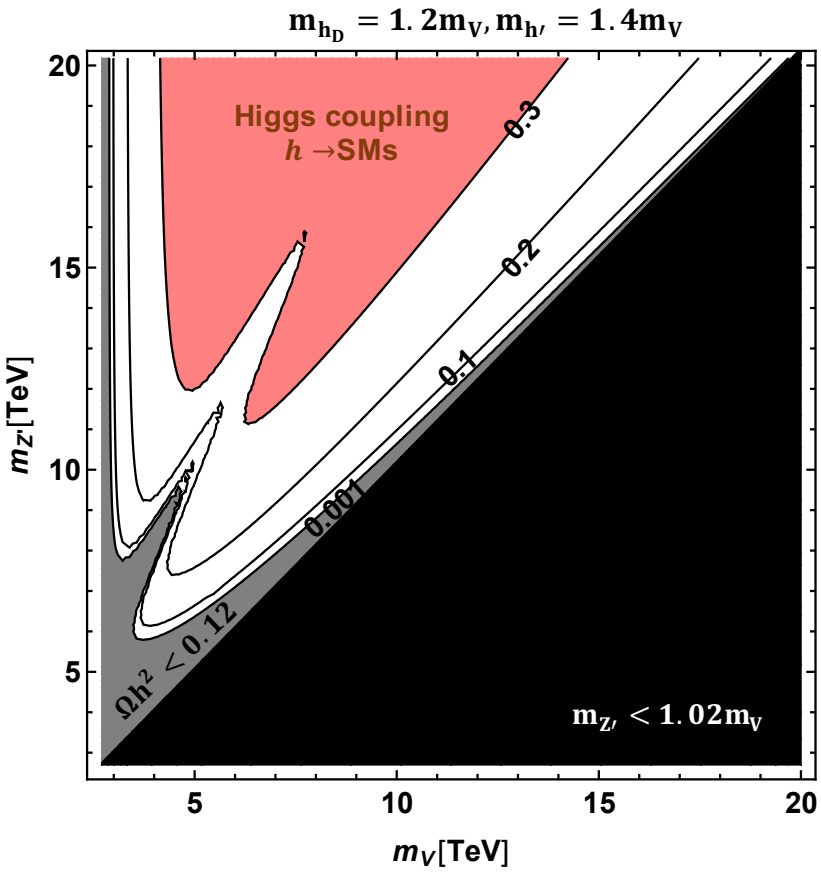

Figure 13: The contours show ϕ_h that reproduce the measured value of the DM relic abundance. Here, $m_{h_D} = 1.2\ m_V$ and $m_{h'} = 1.4\ m_V$. In the gray shaded region, this model cannot explain the whole abundance. The pink region ($\phi_h > 0.3$) is constrained by the measurement of the Higgs signal strength [88]. In the black shaded region, g_0 is beyond the perturbative unitarity bound.

For small ϕ_h, the contributions to the relic abundance from Higgs particles are negligible. In this region, our dark matter only depends on the gauge interaction to reproduce the observed relic density. So our model does not need to rely on the Higgs portal interaction.

For large ϕ_h, the electroweak interaction and the Higgs portal couplings contribute to the value of the relic abundance. As ϕ_h increases, the contribution of the Higgs portal couplings increases and the relic abundance decreases, so $m_{Z'}$ must increase accordingly to obtain the observed relic abundance. The larger ϕ_h requires the heavier $m_{Z'}$ to obtain the observed relic abundance. However, $\phi_h > 0.3$ regions are constrained by the Higgs signal strength as we discussed in Sec.5.5.

There are three regions in which this model can explain the whole relic density ; the light $m_{Z'}$ region ($m_{Z'} \lesssim 2m_V$), the V'-resonant region($m_{Z'} \simeq 2m_V$), and the heavy $m_{Z'}$ region ($m_{Z'} \gtrsim 2m_V$).

For the light $m_{Z'}$ region, pairs of the dark vector bosons mainly annihilate into visible

massive gauge bosons including $W'^{\pm}$ and Z'. The mass of Z' and W' must degenerate to the dark matter mass to decrease the relic abundance, especially when ϕ_h is small. In the V'-resonant region, which looks like a horn in the figure, the main (co)annihilation channel is $V^0V^{\pm} \to q\bar{q}$ via W' exchange in the s-channel. In the heavy $m_{Z'}$ region, pairs of the dark matter particles mainly annihilate into $W^{\pm}$ and Z because the processes with a $W'^{\pm}$ or a Z' in final states are kinematically forbidden. The masses of W' and Z' are much larger than the dark matter particles, and thus W' and Z' are almost decoupled from the annihilation processes.

For our model to account for the whole amount of DM the mass of V^0 must be roughly above 3 TeV. This lower limit is in the region of small ϕ_h and heavy $m_{Z'}$. This region is similar to the Wino DM model [4] and $\mathrm{SU}(2)_L$ triplet scalar DM models [90]. In those models, DM mainly annihilates into $W^{\pm}$ and Z, and the mass of the DM is fixed by requiring the thermal relic to explain the measured value of the DM energy density.

6.3.2 light h' ($m_{h'} = 4$ TeV)

If we consider the small h' region, we can easily avoid the bounds from perturbative unitarity of the Higgs quartic couplings for large ϕ_h values as we discussed in Sec.5.1. The main difference from the analysis using $m_{h'} = 1.4m_V$ is that the relic abundance does not depend on ϕ_h. In this region, λ is too small to contribute to the relic abundance, unlike the $m_{h'} = 1.4m_V$ analysis. The other contributions from the Higgs portal couplings are proportional to the following at the freeze-out temperature.

$$\frac{1}{4m_V^2 - m_h^2} - \frac{1}{4m_V^2 - m_{h'}^2}. \tag{6.13}$$

Thus, these contributions are canceled in $m_V \gg m_{h'}$ limit. Fig. 14 shows the value of ϕ_h that is required to reproduce the observed value of the relic abundance. The masses of h_D and h' are fixed as follows.

$$m_{h_D} = 1.2m_V, \quad m_{h'} = 4 \text{ TeV}. \tag{6.14}$$

As you can see, the overlap of the contour lines is greater than in the heavy h' case. Especially for $m_V \gtrsim 6$ TeV region, the contour lines are completely overlapped and consistent with the contour line when $\phi_h \simeq 0$ for $m_{h'} = 1.4m_V$. The required $m_{Z'}$ for a given value of m_V is determined regardless of the value of ϕ_h.

6.4 Combined results

In the previous section, we find three-parameter regions that can explain the whole relic abundance in our model in both $m_{h'}$ analyses. The V'-resonant region requires small fine-tuning $m_{Z'} \simeq 2m_V$, so we consider the other two scenarios, the light, and heavy $m_{Z'}$ regions, and show the results with the limitations that come from the experiments and observations.

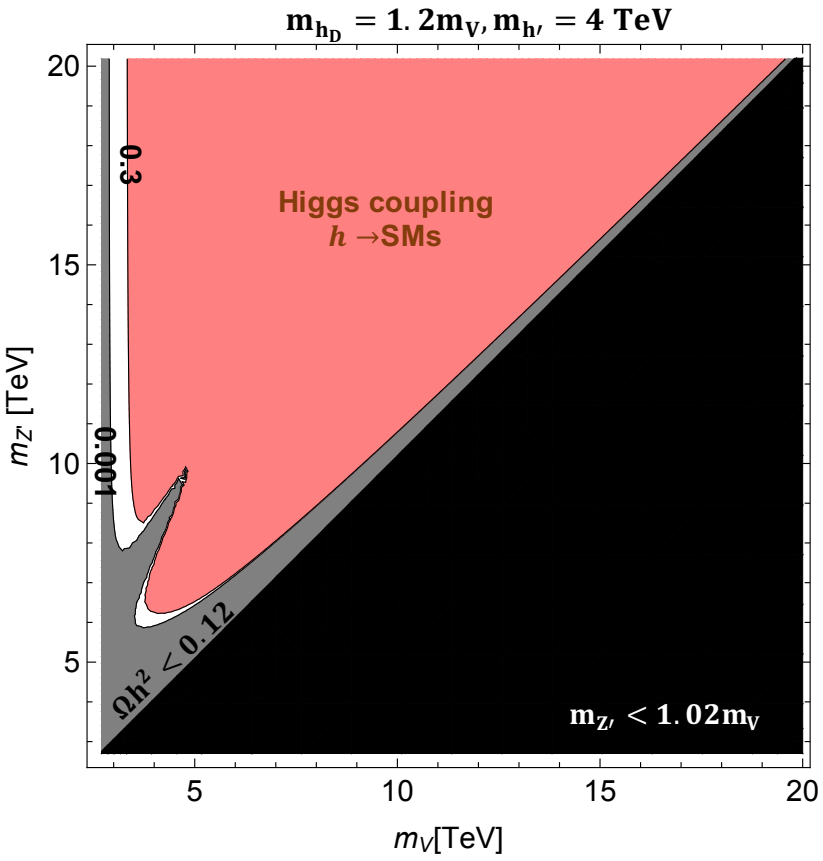

Figure 14: The contours show ϕ_h that reproduce the measured value of the DM relic abundance. Here, $m_{h_D} = 1.2\ m_V$ and $m_{h'}$ =4 TeV. In the gray shaded region, this model cannot explain the whole abundance. The pink region ($\phi_h > 0.3$) is constrained by the measurement of the Higgs signal strength [88]. The black shaded region is theoretically forbidden.

6.4.1 heavy h' ($m_{h'} = 1.4 m_V$)

Fig.15 shows the combined results. The left panel in Fig.15 shows the light $m_{Z'}$ region and the right panel shows the heavy $m_{Z'}$ region. For both cases, the XENON1T experiment [3] gives a stronger constraint than the Higgs signal strength($\phi < 0.3$). The strongest bound on ϕ_h comes from the perturbative unitarity of the Higgs quartic couplings that highly depends on the values of $m_{h'}$. If we consider the small $m_{h'}$ region, the perturbative unitarity bound can be weaker than the XENON1T experiment as we will show next sub-section.

In the top-left area of the left panel in Fig.15, the $SU(2)_1$ gauge coupling, g_1 is large. Therefore the decay rate of W' is beyond the perturbative. The upper limit on $m_{Z'}$ is around 16 TeV and the required and allowed dark matter mass is 2.9 TeV$\lesssim m_V \lesssim$ 3.2 TeV for this scenario.

For the heavy $m_{Z'}$ scenario, the W' search by the ATLAS experiment [84] gives the bound, $m_V \gtrsim 4.2$ TeV. The allowed region is a thin white area. Thus when the dark

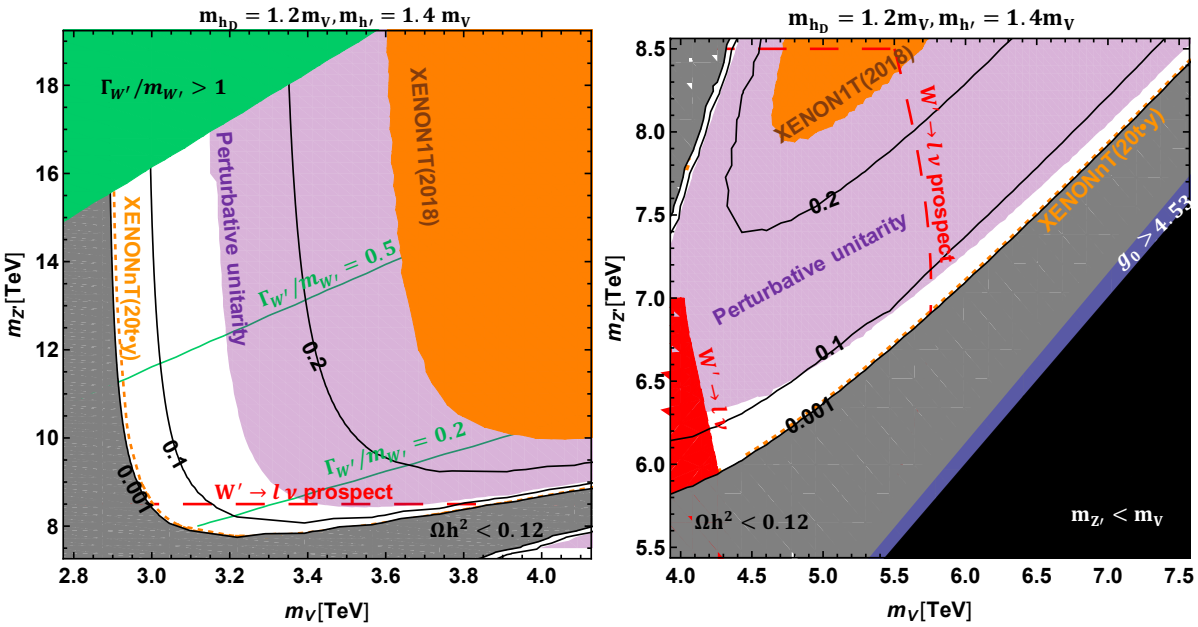

Figure 15: Combined results in the m_V-$m_{Z'}$ plane. The gray shaded region cannot explain the whole abundance and the black shaded region is theoretically forbidden. The orange region is already constrained by the XENON2018 and the dotted line shows the prospect by XENONnT (20 ton·year). In the purple region, some of the Higgs quartic couplings are non-perturbative. The red shaded region is constrained by ATLAS and the red dashed line shows the prospect. In the left panel, the green line shows the value of $\Gamma_{W'}/m_{W'}$, and $\Gamma_{W'} > m_{W'}$ in the green shaded region. In the right panel, g_0 is beyond the perturbative unitarity bound in the blue shaded region.

matter mass is determined, the mass of Z' is also roughly determined.

Most of the parameter space can be searched by the XENONnT experiment [72] for both scenarios. Also, we find the W' search at the HL-LHC [86] can explore $m_V \lesssim 5.8$ TeV and $m_{Z'} \lesssim 8.5$ TeV region. The W' search at the collider experiment is independent of ϕ_h. Therefore the XENONnT experiment and the HL-LHC are complementary to each other.

The smaller ϕ_h region is degenerate in Figs. 15. We magnify those regions in Fig. 16. The values of $m_{Z'}$ that are required to obtain the right amount of DM energy density are shown in the m_V-ϕ_h plane. The left panel shows the lighter m_V region. We find that the combination of the DM direct detection at the XENONnT experiment and the W' search at the HL-LHC is a powerful tool to seek this region. The former will give an upper bound on ϕ_h that is almost independent of m_V. The latter, on the other hand, is sensitive for 3 TeV $\lesssim m_V \lesssim$ 3.9 TeV. For the lighter m_V, $m_V \lesssim 3$ TeV, the W' decay width can be as large as m_V, but in most of the region it satisfies $0.1 < \Gamma_{W'}/m_{W'} < 0.2$. The right panel in Fig. 16 is for V that is heavier than 4 TeV. The direct detection experiment is important in this region as well to determine the value of ϕ_h. For $m_V \lesssim 6$ TeV, we can test this model from the W' search. We find that the perturbative unitarity of scalar quartic couplings gives the upper limit on m_V, $m_V \lesssim 19$ TeV.

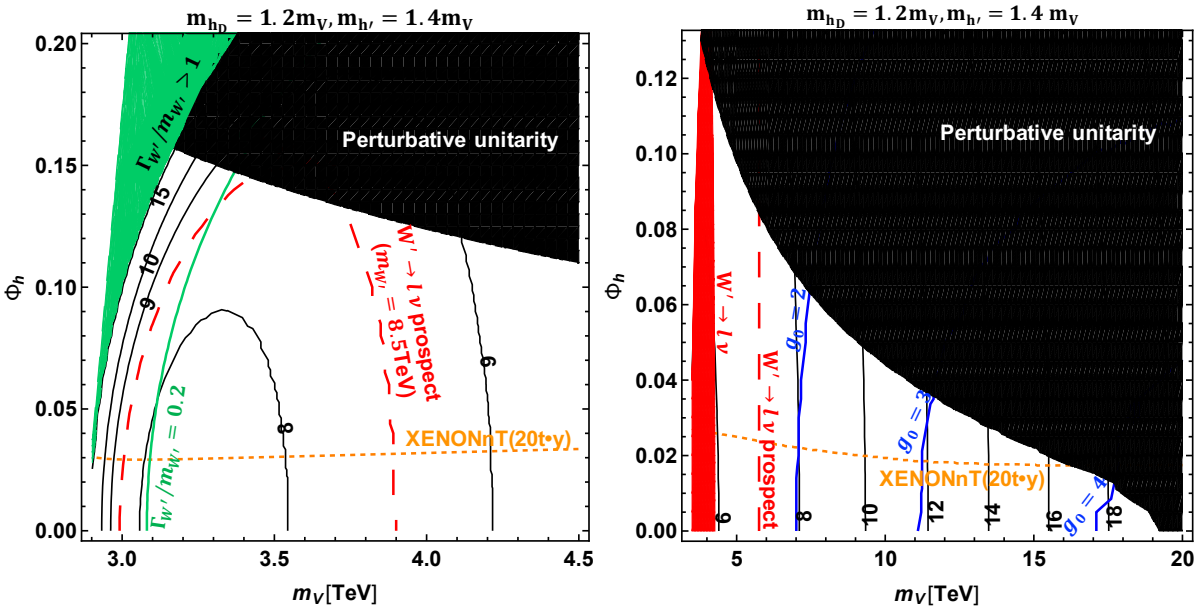

Figure 16: Combined results in the m_V-ϕ_h plane. The left (right) panel shows the case for $m_{Z'} > 2m_V$ ($m_{Z'} < 2m_V$). We determine $m_{Z'}$ to obtain the right amount of the DM relic abundance, and the values are shown by the black-solid contours in TeV unit. The orange dotted line shows the prospect of XENONnT [72]. The red dashed line shows the prospect of W' search [86]. In the left panel, the green line shows the value of $\Gamma_{W'}/m_{W'}$, and $\Gamma_{W'} > m_{W'}$ in the green shaded region. The red shaded region in the right panel is already constrained by the W' search [84]. The black shaded regions in both panels are excluded by the perturbative unitarity of the scalar quartic couplings. The blue-solid contours in the right panel show the value of g_0.

6.4.2 light h' ($m_{h'} = 4$ TeV)

The strongest constraint on ϕ_h comes from the perturbative unitarity of the Higgs quartic couplings in the above analysis. However, if $m_{h'}$ is light, we don't have to care about this constraint. In the heavy $m_{Z'}$ region, the allowed region simply expands, whereas when we investigate the light $m_{Z'}$ region, we can grasp a new feature of this model. Hence we focus on the light $m_{Z'}$ region.

Fig.17 shows the combined results for $m_{h'} = 4$ TeV. We choose the value of $m_{h'}$ so that the unitarity bound of scalar quartic couplings is small enough. In this case, the XENON1T gives the strongest constraint on the scalar mixing angle, $\phi_h \lesssim 0.15$. The allowed region is extended compared to the $m_{h'} = 1.4m_V$ case. Nevertheless, we find the upper limit on m_V, $m_V \lesssim 27.5$ TeV, by the perturbative unitarity of the $SU(2)_0$ gauge coupling. Thus the mass of our dark matter has the theoretical upper limit in both cases.

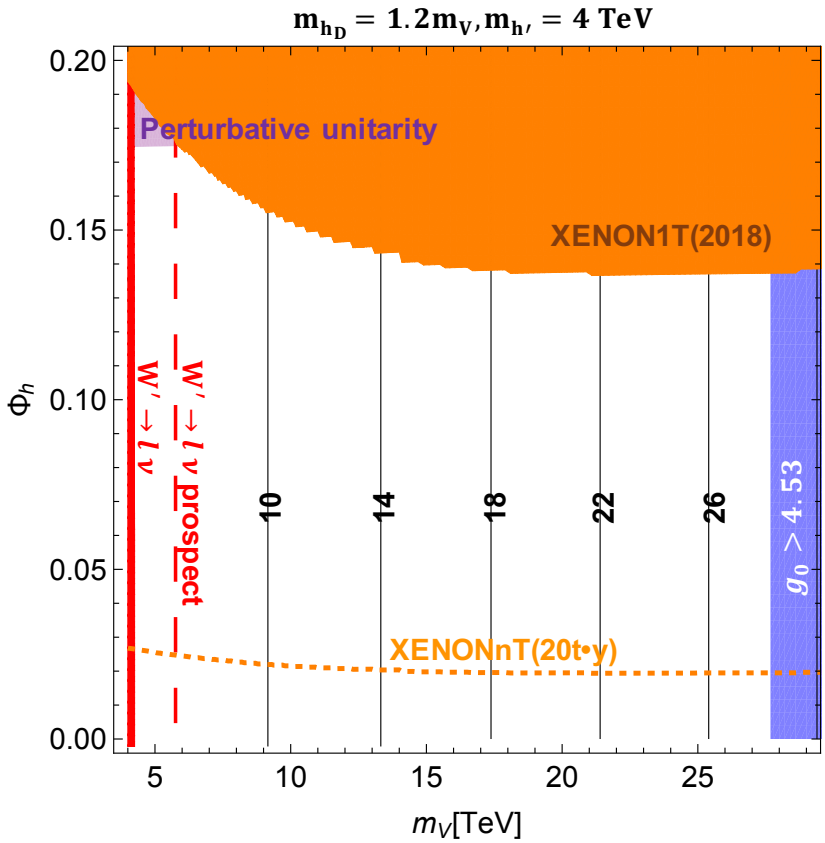

Figure 17: Combined results for $m_{h'}$ =4 TeV in the m_V-ϕ_h plane. The black contours show the values of $m_{Z'}$ in TeV unit to obtain the right amount of the DM relic abundance. The orange shaded region and red shaded region are already constrained by the XENON1T experiment [3] and the W' search [84], respectively. The orange dotted line shows the prospect of XENONnT [72]. The red dashed line shows the prospect of W' search [86]. The small purple shaded region at the top left is excluded by the perturbative unitarity of the scalar quartic couplings. In the blue shaded region, $SU(2)_0$ gauge coupling is non-perturbative.

6.5 Indirect detection

Since our dark matter has the electroweak interaction and is much heavier than the electroweak gauge bosons, the dark matter pair annihilation can be enhanced by the Sommerfeld effect [96–100]. The annihilation into photons can be searched by the indirect detection experiments.

The s-wave pair dark matter annihilation cross section with Sommerfeld enhancement is given by

$$\sigma v = 2 \times \sigma_{\rm tree} v \times |S|^2, \tag{6.15}$$

where the coefficient two is a necessary factor for the annihilation of identical particles and $|S|^2$ is called the enhancement factor. We should solve the Schroedinger equations

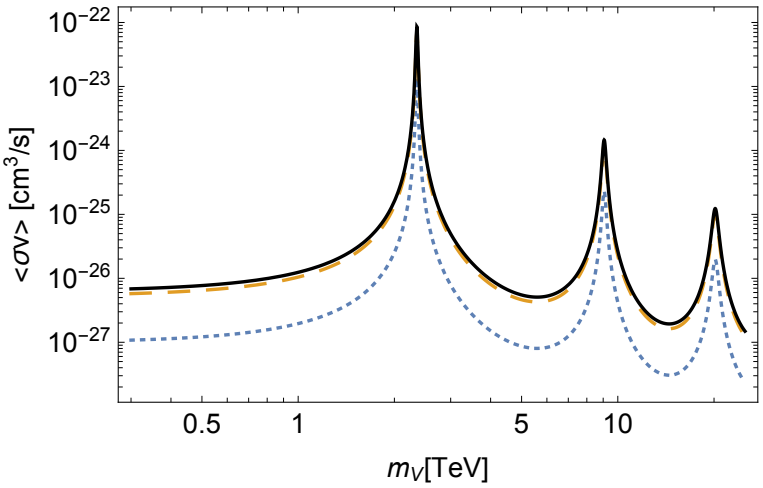

Figure 18: DM pair annihilation cross section into two photons times relative velocity with Sommerfeld enhancement. The dashed (dotted) line shows the total spin-2 (spin-0) annihilation. The plain line shows the sum of them.

to obtain this enhancement factor. If we focus on the small ϕ_h and the heavy Z' and W' region, contributions from Higgs particles and heavy gauge bosons are negligible so that the potential in the Schroedinger equation is the same as in the pure Wino dark matter case. Therefore the enhancement factors for our model are equal to one for the Wino. We can use results in [98]. The tree-level spin-averaged $V^-V^+ \to \gamma\gamma$ cross sections for each total spin $J = 0, 1, 2$ are given by

$$\sigma^{J=0} v_{\rm rel} = \frac{2}{3}\frac{\pi\alpha^2}{m_V^2}, \tag{6.16}$$

$$\sigma^{J=1} v_{\rm rel} = 0, \tag{6.17}$$

$$\sigma^{J=2} v_{\rm rel} = \frac{32}{9}\frac{\pi\alpha^2}{m_V^2}. \tag{6.18}$$

The derivation is shown in Appendix. A.4.

Fig.18 shows the $V^0V^0 \to \gamma\gamma$ cross section including the Sommerfeld effect. The enhancement factors are the same, so our dark matter and Wino have resonance regions in the same places. The total annihilation cross section in our model is nearly four times larger than one in the pure Wino model. Therefore the constraints on our dark matter mass from the indirect detection are expected to be stronger.

6.5.1 Constraints on $\langle\sigma v\rangle_{\gamma\gamma}$

The constraints on the velocity-weighted annihilation cross section into two photons from the H.E.S.S. experiment [61] are shown in Fig.19. The strength of the bounds varies depending on the profile we choose. The most aggressive limit comes from the Einasto profile. $m_V \lesssim 11.4$ TeV and 18.8 TeV $\lesssim m_V \lesssim 21.4$ TeV regions are already constrained. For the NFW profile, $m_V \lesssim 10.7$ TeV and 19.3 TeV $\lesssim m_V \lesssim 21$ TeV regions are constrained.

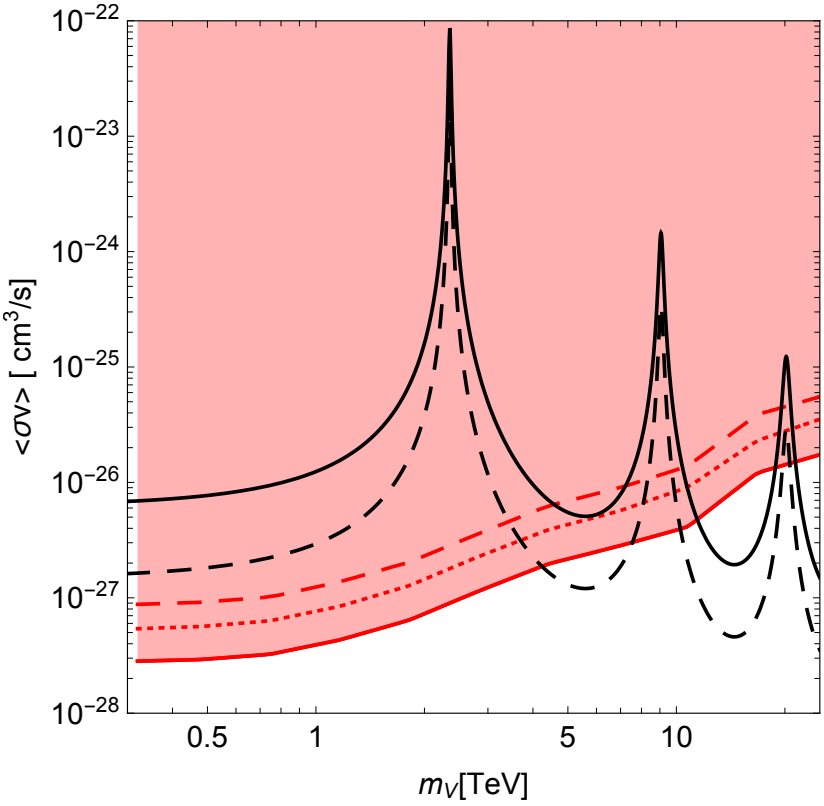

Figure 19: The upper bounds on the velocity averaged cross section into 2 photons from the H.E.S.S. collaboration [61]. The plane (dashed) black line shows the annihilation cross section with the Sommerfeld enhancement in our model (pure Wino). The red shaded region shows the constraint obtained by using the Einasto profile for the dark matter distributions in the Galactic center. The red dotted line and dashed line show the upper limits for the NFW profile and the Einasto2 profile, respectively.

The Einasto2 profile gives the weakest constraints of them, because $\rho_\odot = 0.3$ GeV/cm^3 is assumed to determine the profile parameters, while $\rho_\odot = 0.39$ GeV/cm^3 is used for the other profiles. The areas of $m_V \lesssim 4.6$ TeV and 7.2 TeV $\lesssim m_V \lesssim$10.4 TeV and 19.6 TeV $\lesssim m_V \lesssim 20.8$ TeV has already been explored. So most of the heavy Z' and W' region is limited by the H.E.S.S. experiment.

As discussed in Sec.3.5, this bound could be relaxed by about two or three orders of magnitude if the Galactic center profile is core-like. The H.E.S.S. collaboration does not give the bound for that case, so we are not sure how severe that restriction is for our model. Besides, we have to keep in mind that the bounds coming from the cusp profile may not be believable.

6.5.2 Prospects on the line cross section

The prospects from the CTA collaboration are shown in Fig.20. Here we use the upper bounds on the line cross section obtained by [101]. The definition of the line cross section

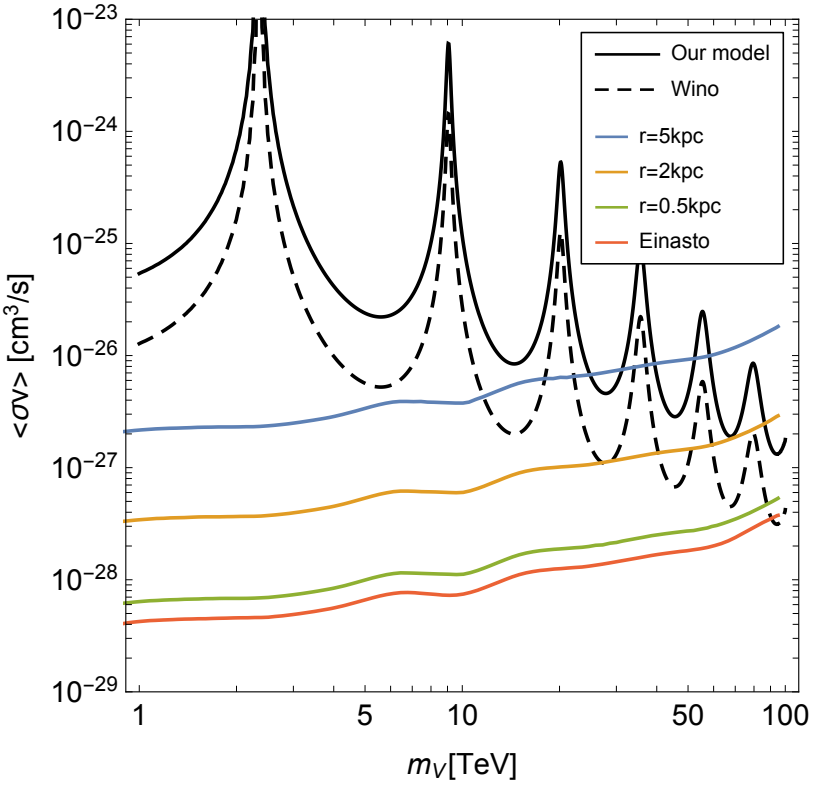

Figure 20: The black plain line and the dashed line show the velocity-averaged line cross section for our model and Wino dark matter, respectively. Each colored line gives an expected upper limit from the CTA collaborations corresponding to the dark matter profile. We use the values in [101].

is given by

$$\langle \sigma v_{\rm rel} \rangle_{\rm line} = \langle \sigma v_{\rm rel} \rangle_{\gamma\gamma} + \frac{1}{2} \langle \sigma v_{\rm rel} \rangle_{Z\gamma}. \tag{6.19}$$

They also take into account the cases of core profiles. For the core radius, $r \lesssim 5$ kpc region is considered because dark matter cores can be extended to this value by baryonic effects [102]. The strength of the restriction can vary up to a factor of 50, depending on the profile.

If the dark matter distribution at the Galactic center is the Einasto profile, the dark matter mass in our model is only allowed to be above 100 TeV. Even if we believe the conservative prospect (cored profile : $r = 5$ kpc), $m_V \lesssim 24.9$ TeV region can be searched. So the indirect detection experiments are very important in exploring our dark matter.

Chapter 7

Conclusions

We constructed a model of spin-1 dark matter that has the electroweak gauge interaction. The electroweak gauge symmetry is extended into $\mathrm{SU}(2)_0 \times \mathrm{SU}(2)_1 \times \mathrm{SU}(2)_2 \times \mathrm{U}(1)_Y$, and the discrete symmetry under the exchanging of $\mathrm{SU}(2)_0$ and $\mathrm{SU}(2)_2$ is imposed. It is not necessary to extend the fermion sector to realize the realistic fermion mass spectra through the Yukawa interactions. Since the dark matter candidate in this model couples to the electroweak gauge bosons, we do not need to rely on the Higgs portal couplings. These two features are distinctive of our model from other spin-1 dark matter models. Our model predicts spin-0 and spin-1 dark matter candidates, and the heavier one decays into the lighter one. In this paper, we focus on the spin-1 dark matter candidate.

The model predicts a heavy vector triplet ($W'^{\pm}$ and Z') in the visible sector. We found that the W' searches at the LHC give a strong constraint. That has already excluded some regions of the parameter space that can explain the measured value of the dark matter energy density by the freeze-out mechanism.

There are three scenarios that the model predicts the right amount of the dark matter relic abundance. The first scenario is that the heavy vector triplet is slightly heavier than the dark matter but has almost degenerate mass. In this case, pairs of dark matter particles can annihilate into a heavy triplet and a SM particle. This process is efficient, and the measured value of dark matter energy density is explained for $m_V \gtrsim 4$ TeV. The upper bound on the mass of the dark matter is imposed by the perturbative unitarity bound of the gauge couplings, $m_V \lesssim 19$ TeV. The HL-LHC can test this scenario up to 6 TeV. The second scenario is for $m_{W'} \simeq 2m_V$ that utilizes the W' resonance in the (co)annihilation processes of pairs of dark matter particles. In this case, the gauge couplings are well in the perturbative regime. The third scenario is for $m_{W'} \gg m_V$. In this scenario, the mass of the dark matter is almost uniquely determined with the assumption that the relic abundance explains the full of the dark matter energy density, $m_V \simeq 3$ TeV. This last scenario is similar to other $\mathrm{SU}(2)_L$-triplet dark matter models. The mass of the W' is bounded by the condition that $\Gamma_{W'} < m_{W'}$, and we find $m_{W'} \lesssim 15$ TeV in the small scalar mixing limit.

Although we do not need to rely on the Higgs portal interactions in this model, it predicts the signal for the direct detection experiments, and thus we also discussed the effects of the scalar mixing. We found that the perturbative unitarity bounds for the

scalar quartic couplings give a stronger constraint on the mixing. We also found that the model is testable at the XENONnT experiment if $|\phi_h| \gtrsim 0.03$.

We can choose light h' to avoid the perturbative unitarity bounds for the scalar quartic couplings. In this case, the stronger limit on the scalar mixing comes from the direct detection experiment, $\phi_h \lesssim 0.15$. The perturbative unitarity of the $SU(2)_0$ gauge coupling gives the upper limit on the dark matter mass, $m_V \lesssim 27.5$ TeV. Hence, for both cases, our model has the upper limit on the dark matter mass.

The indirect detection experiment gives a stringent limit on our model. Conservatively, the regions of $m_V < 4.6$ TeV and 7.2 TeV $\lesssim m_V \lesssim$10.4 TeV and 19.6 TeV $\lesssim m_V \lesssim$20.8 TeV are already restricted by the H.S.S.S. collaboration, so the $m_{Z'} > 2m_V$ scenario has already been explored. But this bound may not be believable due to the very large indeterminacy of the dark matter profile at the Galactic center. We found that the prospect of the CTA collaboration can search $m_V < 24.9$ TeV region if we use the profile that gives the weakest limit.

In this thesis, we include the Sommerfeld effect to consider the bounds from the indirect detection experiments for the small ϕ_h region. However, our dark matter can directly interact with the Higgs boson for large ϕ_h. This is an important difference from Wino dark matter. Moreover, our results for the relic abundance may be altered by the Sommerfeld effect. We leave this to future studies.

Acknowledgments

I would like to thank my supervisor Junji Hisano who provided helpful comments and suggestions. No matter how busy he was, he made time and was very attentive. Special thanks also go to Tomohiro Abe and Motoko Fujiwara, who provided technical help and sincere encouragement. They are collaborators for a central part of this thesis. Finally, I am also particularly grateful to all the members of theoretical particle physics group and my family for their encouragement and continuous support.

Appendix A

our model

A.1 Some details in the gauge sectors

The mass eigenstates are given by

$$\begin{pmatrix} V_\mu^\pm \\ W_\mu^\pm \\ W_\mu'^\pm \end{pmatrix} = \begin{pmatrix} \omega_V^0 & \omega_V^1 & \omega_V^2 \\ \omega_W^0 & \omega_W^1 & \omega_W^2 \\ \omega_{W'}^0 & \omega_{W'}^1 & \omega_{W'}^2 \end{pmatrix} \begin{pmatrix} W_{0\mu}^\pm \\ W_{1\mu}^\pm \\ W_{2\mu}^\mu \end{pmatrix} = \begin{pmatrix} \frac{1}{\sqrt{2}} & 0 & -\frac{1}{\sqrt{2}} \\ \frac{\sin\phi_\pm}{\sqrt{2}} & \cos\phi_\pm & \frac{\sin\phi_\pm}{\sqrt{2}} \\ \frac{\cos\phi_\pm}{\sqrt{2}} & -\sin\phi_\pm & \frac{\cos\phi_\pm}{\sqrt{2}} \end{pmatrix} \begin{pmatrix} W_{0\mu}^\pm \\ W_{1\mu}^\pm \\ W_{2\mu}^\mu \end{pmatrix}, \quad \text{(A.1)}$$

$$\begin{pmatrix} V_\mu^0 \\ A_\mu \\ Z_\mu \\ Z_\mu'^\pm \end{pmatrix} = \begin{pmatrix} \omega_V^0 & \omega_V^1 & \omega_V^2 & \omega_V^B \\ \omega_\gamma^0 & \omega_\gamma^1 & \omega_\gamma^2 & \omega_\gamma^B \\ \omega_Z^0 & \omega_Z^1 & \omega_Z^2 & \omega_Z^B \\ \omega_{Z'}^0 & \omega_{Z'}^1 & \omega_{Z'}^2 & \omega_{Z'}^B \end{pmatrix} \begin{pmatrix} W_{0\mu}^3 \\ W_{1\mu}^3 \\ W_{2\mu}^3 \\ B_\mu \end{pmatrix} = \begin{pmatrix} \frac{1}{\sqrt{2}} & 0 & -\frac{1}{\sqrt{2}} & 0 \\ \frac{e}{g_0} & \frac{e}{g_1} & \frac{e}{g_0} & \frac{e}{g'} \\ \omega_Z^0 & \omega_Z^1 & \omega_Z^0 & \omega_Z^B \\ \omega_{Z'}^0 & \omega_{Z'}^1 & \omega_{Z'}^0 & \omega_{Z'}^B \end{pmatrix} \begin{pmatrix} W_{0\mu}^3 \\ W_{1\mu}^3 \\ W_{2\mu}^3 \\ B_\mu \end{pmatrix}, \quad \text{(A.2)}$$

where

$$e = \left(\frac{2}{g_0^2} + \frac{1}{g_1^2} + \frac{1}{g'^2} \right)^{-1/2}, \quad \text{(A.3)}$$

$$\omega_Z^0 = \omega_Z^2 = \frac{e g_1}{\sqrt{g_0^2 + 2g_1^2} g'} \cos\phi_0 + \frac{g_0}{\sqrt{2(g_0^2 + 2g_1^2)}} \sin\phi_0, \quad \text{(A.4)}$$

$$\omega_Z^1 = \frac{e g_0}{\sqrt{g_0^2 + 2g_1^2} g'} \cos\phi_0 - \frac{\sqrt{2} g_1}{\sqrt{g_0^2 + 2g_1^2}} \sin\phi_0, \quad \text{(A.5)}$$

$$\omega_Z^B = -\frac{e\sqrt{g_0^2 + 2g_1^2}}{g_0 g_1} \cos\phi_0, \quad \text{(A.6)}$$

$$\omega_{Z'}^0 = \omega_{Z'}^2 = \frac{g_0}{\sqrt{2(g_0^2 + 2g_1^2)}} \cos\phi_0 - \frac{e g_1}{\sqrt{g_0^2 + 2g_1^2} g'} \sin\phi_0, \quad \text{(A.7)}$$

$$\omega_{Z'}^1 = -\frac{\sqrt{2} g_1}{\sqrt{g_0^2 + 2g_1^2}} \cos\phi_0 - \frac{e g_0}{\sqrt{g_0^2 + 2g_1^2} g'} \sin\phi_0, \quad \text{(A.8)}$$

$$\omega_{Z'}^B = \frac{e\sqrt{g_0^2 + 2g_1^2}}{g_0 g_1} \sin\phi_0. \quad \text{(A.9)}$$

Using $g_W = \sqrt{g_0^2 g_1^2/(g_0^2+2g_1^2)}$, the electron charge, e, is rewritten as

$$e = \left(\frac{1}{g_W^2} + \frac{1}{g'^2}\right)^{-1/2} = \frac{g_W^2 g'^2}{g_W^2 + g'^2}. \tag{A.10}$$

Here we introduce $\phi_\pm$ and ϕ_0 that satisfy

$$\frac{1}{4}\begin{pmatrix} g_1^2(v^2+2v_\Phi^2) & -\sqrt{2}g_0 g_1 v_\Phi^2 \\ -\sqrt{2}g_0 g_1 v_\Phi^2 & g_0^2 v_\Phi^2 \end{pmatrix}\begin{pmatrix} \cos\phi_\pm & -\sin\phi_\pm \\ \sin\phi_\pm & \cos\phi_\pm \end{pmatrix} = \begin{pmatrix} \cos\phi_\pm & -\sin\phi_\pm \\ \sin\phi_\pm & \cos\phi_\pm \end{pmatrix}\begin{pmatrix} m_W^2 & 0 \\ 0 & m_{W'}^2 \end{pmatrix}, \tag{A.11}$$

$$\frac{1}{4}\begin{pmatrix} \frac{g_0^2 g_1^2 g'^2}{e^2(g_0^2+2g_1^2)}v^2 & -\frac{\sqrt{2}g_0 g_1^3 g'}{e(g_0^2+2g_1^2)}v^2 \\ -\frac{\sqrt{2}g_0 g_1^3 g'}{e(g_0^2+2g_1^2)}v^2 & \frac{(g_0^2+2g_1^2)^2 v_\Phi^2 + 2g_1^4 v^2}{(g_0^2+2g_1^2)} \end{pmatrix}\begin{pmatrix} \cos\phi_0 & -\sin\phi_0 \\ \sin\phi_0 & \cos\phi_0 \end{pmatrix} = \begin{pmatrix} \cos\phi_0 & -\sin\phi_0 \\ \sin\phi_0 & \cos\phi_0 \end{pmatrix}\begin{pmatrix} m_Z^2 & 0 \\ 0 & m_{Z'}^2 \end{pmatrix}. \tag{A.12}$$

We find

$$\cos^2\phi_\pm = \frac{m_{V^\pm}^2 - m_W^2}{m_{W'}^2 - m_W^2}. \tag{A.13}$$

One can always choose $\cos\phi_\pm > 0$ as a convention, and thus

$$\cos\phi_\pm = \sqrt{\frac{m_{V^\pm}^2 - m_W^2}{m_{W'}^2 - m_W^2}}, \quad \sin\phi_\pm = \sqrt{\frac{m_{W'}^2 - m_{V^\pm}^2}{m_{W'}^2 - m_W^2}}. \tag{A.14}$$

We also find neutral gauge boson masses,

$$\begin{aligned} m_Z^2 =& \frac{1}{8}\Big\{ g_1^2 v^2 + g_0^2 v_\Phi^2 + 2g_1^2 v_\Phi^2 + v^2 g'^2 \\ & - \sqrt{(g_1^2 v^2 + g_0^2 v_\Phi^2 + 2g_1^2 v_\Phi^2 + v^2 g'^2)^2 - 4(g_0^2 g_1^2 + g_0^2 g'^2 + 2g_1^2 g'^2) v^2 v_\Phi^2}\Big\}, \end{aligned} \tag{A.15}$$

$$\begin{aligned} m_{Z'}^2 =& \frac{1}{8}\Big\{ g_1^2 v^2 + g_0^2 v_\Phi^2 + 2g_1^2 v_\Phi^2 + v^2 g'^2 \\ & + \sqrt{(g_1^2 v^2 + g_0^2 v_\Phi^2 + 2g_1^2 v_\Phi^2 + v^2 g'^2)^2 - 4(g_0^2 g_1^2 + g_0^2 g'^2 + 2g_1^2 g'^2) v^2 v_\Phi^2}\Big\}, \end{aligned} \tag{A.16}$$

and charged gauge boson masses,

$$m_W^2 = \frac{1}{8}\left\{ g_1^2 v^2 + (g_0^2+2g_1^2)v_\Phi^2 - \sqrt{-4g_0^2 g_1^2 v^2 v_\Phi^2 + [g_1^2 v^2 + (g_0^2+2g_1^2)v_\Phi^2]^2}\right\}, \tag{A.17}$$

$$m_{W'}^2 = \frac{1}{8}\left\{ g_1^2 v^2 + (g_0^2+2g_1^2)v_\Phi^2 + \sqrt{-4g_0^2 g_1^2 v^2 v_\Phi^2 + [g_1^2 v^2 + (g_0^2+2g_1^2)v_\Phi^2]^2}\right\}. \tag{A.18}$$

For $v_\Phi \gg v$, the mixing angles are given by

$$\cos\phi_\pm = \frac{g_0}{\sqrt{g_0^2+2g_1^2}} + \mathcal{O}(v_\Phi^{-2}) \simeq \frac{m_V}{m_{Z'}}, \tag{A.19}$$

$$\sin\phi_\pm = \frac{\sqrt{2}g_1}{\sqrt{g_0^2+2g_1^2}} + \mathcal{O}(v_\Phi^{-2}) \simeq \sqrt{1-\frac{m_V^2}{m_{Z'}^2}}, \tag{A.20}$$

$$\cos\phi_0 = 1 + \mathcal{O}(v_\Phi^{-4}), \tag{A.21}$$

$$\sin\phi_0 = \frac{\sqrt{2}g_0 g_1^3 g'}{e(g_0^2+2g_1^2)^2}\frac{v^2}{v_\Phi^2} + \mathcal{O}(v_\Phi^{-4}). \tag{A.22}$$

A.2 Would-be NG bosons

The mass matrices for the gauge bosons are given by

$$\mathcal{M}_C^2 = Q_W^t Q_W, \quad \mathcal{M}_N^2 = Q_Z^t Q_Z, \tag{A.23}$$

where

$$Q_W = \frac{1}{2}\begin{pmatrix} g_0 v_\Phi & -g_1 v_\Phi & 0 \\ 0 & g_1 v & 0 \\ 0 & -g_1 v_\Phi & g_0 v_\Phi \end{pmatrix}, \tag{A.24}$$

$$Q_Z = \frac{1}{2}\begin{pmatrix} g_0 v_\Phi & -g_1 v_\Phi & 0 & 0 \\ 0 & g_1 v & 0 & -g' v \\ 0 & -g_1 v_\Phi & g_0 v_\Phi & 0 \end{pmatrix}. \tag{A.25}$$

In the R_ξ gauge, the mass terms are given by

$$-\begin{pmatrix}\pi_1^+ & \pi_3^+ & \pi_2^+\end{pmatrix}\xi Q_W Q_W^t \begin{pmatrix}\pi_1^- \\ \pi_3^+ \\ \pi_2^-\end{pmatrix} - \frac{1}{2}\begin{pmatrix}\pi_1^0 & \pi_3^0 & \pi_2^0\end{pmatrix}\xi Q_Z Q_Z^t \begin{pmatrix}\pi_1^0 \\ \pi_3^0 \\ \pi_2^0\end{pmatrix}. \tag{A.26}$$

The eigenvectors of the mass matrices are

$$Q_W^t Q_W \vec{\omega}_X = m_X^2 \vec{\omega}_X, \tag{A.27}$$

$$Q_W Q_W^t \vec{\omega}_{\pi_X} = m_X^2 \vec{\omega}_{\pi_X}, \tag{A.28}$$

$$Q_Z^t Q_Z \vec{\omega}_X = m_X^2 \vec{\omega}_X, \tag{A.29}$$

$$Q_Z Q_Z^t \vec{\omega}_{\pi_X} = m_X^2 \vec{\omega}_{\pi_X}. \tag{A.30}$$

Multiplying Q_W to Eq. (A.27) and comparing it with Eq. (A.28), one can find that $Q_W\vec{\omega}_X \propto \vec{\omega}_{\pi_X}$. Note that $(Q_W\vec{\omega}_X)^t(Q_W\vec{\omega}_X) = \vec{\omega}_X^t Q_W^t Q_W \vec{\omega}_X = m_X^2$ and $\vec{\omega}_{\pi_X}^t\vec{\omega}_{\pi_X} = 1$. Similar relations are also found in the neutral sector. Finally, we find

$$Q_W\vec{\omega}_X = m_X\vec{\omega}_{\pi_X}, \tag{A.31}$$

$$Q_Z\vec{\omega}_X = m_X\vec{\omega}_{\pi_X}. \tag{A.32}$$

These relations are useful to obtain the Fermi constant and some relation among couplings. For example, we use

$$g_1 v \omega_X^1 = 2 m_X \omega_{\pi_X}^3 \tag{A.33}$$

to obtain the Fermi constant.

The mixing angles for the charged NG-bosons are given by

$$\begin{pmatrix} \vec{\omega}_{\pi_{V^\pm}} & \vec{\omega}_{\pi_W} & \vec{\omega}_{\pi_{W'}} \end{pmatrix} = \begin{pmatrix} \omega^1_{\pi_{V^\pm}} & \omega^1_{\pi_W} & \omega^1_{\pi_{W'}} \\ \omega^3_{\pi_{V^\pm}} & \omega^3_{\pi_W} & \omega^3_{\pi_{W'}} \\ \omega^2_{\pi_{V^\pm}} & \omega^2_{\pi_W} & \omega^2_{\pi_{W'}} \end{pmatrix} = \begin{pmatrix} \frac{1}{\sqrt{2}} & \frac{\sin\phi_\pi}{\sqrt{2}} & \frac{\cos\phi_\pi}{\sqrt{2}} \\ 0 & \cos\phi_\pi & -\sin\phi_\pi \\ -\frac{1}{\sqrt{2}} & \frac{\sin\phi_\pi}{\sqrt{2}} & \frac{\cos\phi_\pi}{\sqrt{2}} \end{pmatrix}, \tag{A.34}$$

where $\sin\phi_\pi$ and $\cos\phi_\pi$ satisfy

$$\frac{1}{4}\begin{pmatrix} g_1^2 v^2 & -\sqrt{2} g_1^2 v v_\Phi \\ -\sqrt{2} g_1^2 v v_\Phi & (g_0^2 + 2 g_1^2) v_\Phi^2 \end{pmatrix} \begin{pmatrix} \cos\phi_\pi & -\sin\phi_\pi \\ \sin\phi_\pi & \cos\phi_\pi \end{pmatrix} = \begin{pmatrix} \cos\phi_\pi & -\sin\phi_\pi \\ \sin\phi_\pi & \cos\phi_\pi \end{pmatrix} \begin{pmatrix} m_W^2 & 0 \\ 0 & m_{W'}^2 \end{pmatrix}. \tag{A.35}$$

Comparing Eqs. (A.34) and (A.31), we find

$$\cos\phi_\pi = \frac{g_1 v}{2 m_W} \cos\phi_\pm, \tag{A.36}$$

$$\sin\phi_\pi = \frac{g_1 v}{2 m_{W'}} \sin\phi_\pm. \tag{A.37}$$

The mixing angles for the neutral NG-bosons are given by

$$\begin{pmatrix} \vec{\omega}_{\pi_{V^0}} & \vec{\omega}_{\pi_Z} & \vec{\omega}_{\pi_{Z'}} \end{pmatrix} = \begin{pmatrix} \omega^1_{\pi_{V^0}} & \omega^1_{\pi_Z} & \omega^1_{\pi_{Z'}} \\ \omega^3_{\pi_{V^0}} & \omega^3_{\pi_Z} & \omega^3_{\pi_{Z'}} \\ \omega^2_{\pi_{V^0}} & \omega^2_{\pi_Z} & \omega^2_{\pi_{Z'}} \end{pmatrix} = \begin{pmatrix} \frac{1}{\sqrt{2}} & \frac{\sin\phi_{\pi_0}}{\sqrt{2}} & \frac{\cos\phi_{\pi_0}}{\sqrt{2}} \\ 0 & \cos\phi_{\pi_0} & -\sin\phi_{\pi_0} \\ -\frac{1}{\sqrt{2}} & \frac{\sin\phi_{\pi_0}}{\sqrt{2}} & \frac{\cos\phi_{\pi_0}}{\sqrt{2}} \end{pmatrix}, \tag{A.38}$$

where $\sin\phi_{\pi_0}$ and $\cos\phi_{\pi_0}$ satisfy

$$\frac{1}{4}\begin{pmatrix} (g_1^2 + g'^2) v^2 & -\sqrt{2} g_1^2 v v_\Phi \\ -\sqrt{2} g_1^2 v v_\Phi & (g_0^2 + 2 g_1^2) v_\Phi^2 \end{pmatrix} \begin{pmatrix} \cos\phi_{\pi_0} & -\sin\phi_{\pi_0} \\ \sin\phi_{\pi_0} & \cos\phi_{\pi_0} \end{pmatrix} = \begin{pmatrix} \cos\phi_{\pi_0} & -\sin\phi_{\pi_0} \\ \sin\phi_{\pi_0} & \cos\phi_{\pi_0} \end{pmatrix} \begin{pmatrix} m_Z^2 & 0 \\ 0 & m_{Z'}^2 \end{pmatrix}. \tag{A.39}$$

Comparing Eqs. (A.38) and (A.32), we find

$$\cos\phi_{\pi_0} = \frac{v}{2 m_Z} (g_1 \omega_Z^1 - g' \omega_Z^B), \tag{A.40}$$

$$\sin\phi_{\pi_0} = -\frac{v}{2 m_{Z'}} (g_1 \omega_{Z'}^1 - g' \omega_{Z'}^B). \tag{A.41}$$

A.3 Fermi constant

The Fermi constant is defined by the muon decay, $\mu \to \nu_\mu e \bar{\nu}_e$. There is a W' exchanging diagram as well as the W-exchanging diagram. We have to add both contributions. We

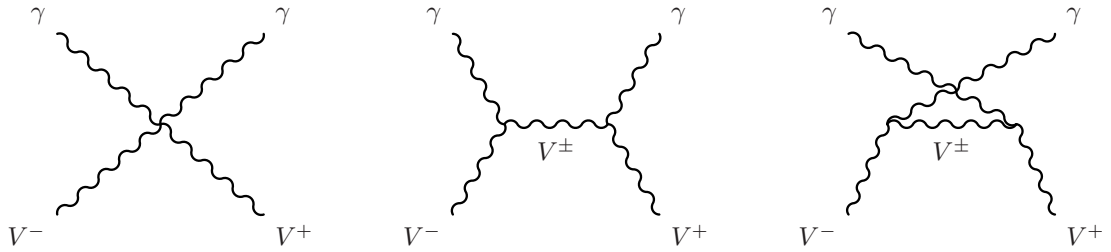

Figure 21: The tree-level diagrams which contribute to $V^-V^+ \to \gamma\gamma$ process.

can simplify the calculation by using the relation between the mixing angles in the gauge sector and NG-boson sector. The Fermi constant is given by

$$\begin{aligned}\sqrt{2}G_F \equiv& \sum_{X=W,W'} \frac{g_{X\bar{\nu_\mu}} g_{X\bar{e}\nu_e}}{4m_X^2} \\ =& \sum_{X=W,V,W'} \frac{(g_1\omega_X^1)^2}{4m_X^2} \\ =& \sum_{X=W,V,W'} \frac{(\omega_{\pi_X}^3)^2}{v^2} \\ =& \frac{1}{v^2}. \end{aligned} \tag{A.42}$$

In the last line, we used that $\sum_X \omega_{\pi_X}^j \omega_{\pi_X}^k = \delta^{jk}$. Therefore, we find

$$\sqrt{2}G_F = \frac{1}{v^2}. \tag{A.43}$$

A.4 $V^-V^+ \to \gamma\gamma$ annihilation cross section

In this section we calculate the cross section for the V^- and V^+ annihilation into two photons. The tree-level diagrams in the unitarity gauge are shown in Fig.21. The $V^-(p_-)V^+(p_+) \to \gamma(k_1)\gamma(k_2)$ amplitude for each diagram is given as follows.

$$i\mathcal{M}_4 = ie^2(g^{\mu\rho}g^{\nu\sigma} + g^{\nu\rho}g^{\mu\sigma} - 2g^{\mu\nu}g^{\rho\sigma})\epsilon_\sigma(p_-)\epsilon_\rho(p_+)\epsilon_\mu^*(k_1)\epsilon_\nu^*(k_2), \tag{A.44}$$

$$\begin{aligned} i\mathcal{M}_t =& ie[(p_- + q)^\mu g^{\alpha\sigma} + (-p_- - k_1)^\alpha g^{\mu\sigma} + (k_1 - q)^\sigma g^{\mu\alpha}] \frac{-i}{q^2 - m_V^2}\left(g_{\alpha\beta} - \frac{q_\alpha q_\beta}{m_V^2}\right) \\ & \times ie[(q - p_+)^\nu g^{\beta\rho} + (-q - k_2)^\rho g^{\beta\nu} + (k_2 + p_+)^\beta g^{\rho\nu}]\epsilon_\sigma(p_-)\epsilon_\rho(p_+)\epsilon_\mu^*(k_1)\epsilon_\nu^*(k_2), \end{aligned} \tag{A.45}$$

$$\begin{aligned} i\mathcal{M}_u =& ie[(p_- + q')^\nu g^{\alpha\sigma} + (-p_- - k_2)^\alpha g^{\nu\sigma} + (k_2 - q')^\sigma g^{\nu\alpha}] \frac{-i}{q'^2 - m_V^2}\left(g_{\alpha\beta} - \frac{q'_\alpha q'_\beta}{m_V^2}\right) \\ & \times ie[(q' - p_+)^\mu g^{\beta\rho} + (-q' - k_1)^\rho g^{\beta\mu} + (k_1 + p_+)^\beta g^{\rho\mu}]\epsilon_\sigma(p_-)\epsilon_\rho(p_+)\epsilon_\mu^*(k_1)\epsilon_\nu^*(k_2), \end{aligned} \tag{A.46}$$

where $q \equiv p_- - k_1$ and $q' \equiv p_- - k_2$.

To calculate the Sommerfeld effects, we need to know the cross section for each total spin state. In this case, the initial state (two spin-1 particles) can be total spin, $J = 0, 1, 2$. We can obtain the cross section for each total spin by replacing the initial state polarization vectors with the initial spin state matrix for the total spin, J and the z-component of the spin, J_z, as follows.

$$\epsilon_\sigma(p_-)\epsilon_\rho(p_+) \to S^{J,J_z}_{\sigma\rho}. \tag{A.47}$$

We consider the non-relativistic limit for the initial state. The polarization vectors of massive gauge bosons in the initial state are given by

$$|1,1\rangle : \epsilon_\mu = \frac{1}{\sqrt{2}}\begin{pmatrix}0\\-1\\-i\\0\end{pmatrix}, \quad |1,0\rangle : \epsilon_\mu = \begin{pmatrix}0\\0\\0\\1\end{pmatrix}, \quad |1,-1\rangle : \epsilon_\mu = \frac{1}{\sqrt{2}}\begin{pmatrix}0\\1\\-i\\0\end{pmatrix}. \tag{A.48}$$

The time-like components of these polarization vectors are 0, so $S_{00} = 0$ and $S_{\sigma 0} = 0 = S_{0\rho}$. Then the space-like components of the initial spin state matrix, $\hat{S}^{J,J_Z} \equiv S^{J,J_z}_{ij}$ $(i, j = 1, 2, 3)$ are given by

$$\hat{S}^{2,2} = \frac{1}{2}\begin{pmatrix}1 & i & 0\\ i & -1 & 0\\ 0 & 0 & 0\end{pmatrix}, \quad \hat{S}^{2,1} = \frac{1}{2}\begin{pmatrix}0 & 0 & -1\\ 0 & 0 & -i\\ -1 & -i & 0\end{pmatrix}, \quad \hat{S}^{2,0} = \frac{1}{\sqrt{6}}\begin{pmatrix}-1 & 0 & 0\\ 0 & -1 & 0\\ 0 & 0 & 2\end{pmatrix},$$
$$\hat{S}^{2,-1} = \frac{1}{2}\begin{pmatrix}0 & 0 & 1\\ 0 & 0 & -i\\ 1 & -i & 0\end{pmatrix}, \quad \hat{S}^{2,-2} = \frac{1}{2}\begin{pmatrix}1 & -i & 0\\ -i & -1 & 0\\ 0 & 0 & 0\end{pmatrix}, \tag{A.49}$$

$$\hat{S}^{1,1} = \frac{1}{2}\begin{pmatrix}0 & 0 & -1\\ 0 & 0 & -i\\ 1 & i & 0\end{pmatrix}, \quad \hat{S}^{1,0} = \frac{1}{\sqrt{2}}\begin{pmatrix}0 & i & 0\\ -i & 0 & 0\\ 0 & 0 & 0\end{pmatrix}, \quad \hat{S}^{1,-1} = \frac{1}{2}\begin{pmatrix}0 & 0 & -1\\ 0 & 0 & i\\ 1 & -i & 0\end{pmatrix}, \tag{A.50}$$

$$\hat{S}^{0,0} = \frac{-1}{\sqrt{3}}\begin{pmatrix}1 & 0 & 0\\ 0 & 1 & 0\\ 0 & 0 & 1\end{pmatrix}. \tag{A.51}$$

$\hat{S}^{J,J_z}$ is symmetric for $J = 0, 2$ and anti-symmetric for $J = 1$. Using these properties, the sum of the amplitudes in the center-of-mass frame is rewritten to the following form.

$$\mathcal{M}^{J=0,2} = 2e^2\left[4\epsilon_i^*(k_1)\hat{S}^{J,J_Z}_{ij}\epsilon_j^*(k_2) - \epsilon_i^*(k_1)\epsilon_i^*(k_2)\left(\mathrm{tr}\hat{S}^{J,J_Z} - \frac{2}{m_V^2}k_j\hat{S}^{J,J_Z}_{jk}k_k\right)\right], \tag{A.52}$$

$$\mathcal{M}^{J=1} = 0. \tag{A.53}$$

where $\epsilon_i(k)$ and k_i are the space-like components of $\epsilon_\mu(k)$ and $k_{1\mu}$, respectively. S^{2,J_z} is trace-less but $S^{0,0}$ is proportional to the unit matrix. Then, we get

$$\mathcal{M}^{J=0} = 2e^2 \left[4\epsilon_i^*(k_1)\hat{S}_{ij}^{0,0}\epsilon_j^*(k_2) - \epsilon_i^*(k_1)\epsilon_i^*(k_2)\left(\mathrm{tr}\hat{S}^{0,0} - \frac{2}{m_V^2} k_j \hat{S}_{jk}^{0,0} k_k \right) \right], \tag{A.54}$$

$$\mathcal{M}^{J=1} = 0, \tag{A.55}$$

$$\mathcal{M}^{J=2} = 2e^2 \left[4\epsilon_i^*(k_1)\hat{S}_{ij}^{2,J_z}\epsilon_j^*(k_2) + \epsilon_i^*(k_1)\epsilon_i^*(k_2)\frac{2}{m_V^2} k_j \hat{S}_{jk}^{2,J_z} k_k \right]. \tag{A.56}$$

The polarization vectors for photons in the final state are given by

$$\epsilon_i^{\pm}(k_1) = \frac{1}{\sqrt{2}} \begin{pmatrix} \mp\cos\theta \\ -i \\ \pm\sin\theta \end{pmatrix}, \quad \epsilon_i^{\pm}(k_2) = \frac{1}{\sqrt{2}} \begin{pmatrix} \pm\cos\theta \\ -i \\ \mp\sin\theta \end{pmatrix}, \tag{A.57}$$

where θ is the angle of momentum, k_1 as viewed from the z-axis. Then, we take the sum of the final state spins for the squared amplitudes and obtain

$$\sum_{final} |\mathcal{M}^{J=0}|^2 = 24e^4, \tag{A.58}$$

$$\sum_{final} |\mathcal{M}^{J=1}|^2 = 0, \tag{A.59}$$

$$\sum_{final} |\mathcal{M}^{J=2}|^2 = \begin{cases} 8e^4(1 + 6\cos^2\theta + \cos^4\theta), & \text{for } J_z = \pm 2, \\ 16e^4 \sin^2\theta(3 + \cos 2\theta), & \text{for } J_z = \pm 1, \\ 48e^4 \sin^4\theta, & \text{for } J_z = 0. \end{cases} \tag{A.60}$$

Using these values, we can calculate the cross section for each total spin

$$\sigma^{J=0} v_{\mathrm{rel}} = 6\frac{\pi\alpha^2}{m_V^2}, \tag{A.61}$$

$$\sigma^{J=1} v_{\mathrm{rel}} = 0, \tag{A.62}$$

$$\sigma^{J=2} v_{\mathrm{rel}} = \frac{32}{5}\frac{\pi\alpha^2}{m_V^2}, \qquad \text{for each } J_z = \pm 2, \pm 1, 0. \tag{A.63}$$

The spin averaged total cross section is given by

$$\begin{aligned} \sigma_{\mathrm{tot}}(\gamma\gamma) v_{rel} =& \frac{1}{9}\sigma^{J=0} v_{rel} + \frac{3}{9}\sigma^{J=1} v_{rel} + \frac{5}{9}\sigma^{J=2} v_{rel} \\ =& \frac{38}{9}\frac{\pi\alpha^2}{m_V^2}. \end{aligned} \tag{A.64}$$

Bibliography

[1] N. Aghanim *et al.* [Planck Collaboration], "Planck 2018 results. VI. Cosmological parameters," arXiv:1807.06209 [astro-ph.CO].

[2] B. W. Lee and S. Weinberg, "Cosmological Lower Bound on Heavy Neutrino Masses," Phys. Rev. Lett. **39**, 165 (1977).

[3] E. Aprile *et al.* [XENON Collaboration], "Dark Matter Search Results from a One Ton-Year Exposure of XENON1T," Phys. Rev. Lett. **121**, no. 11, 111302 (2018) [arXiv:1805.12562 [astro-ph.CO]].

[4] J. Hisano, S. Matsumoto, M. Nagai, O. Saito and M. Senami, "Non-perturbative effect on thermal relic abundance of dark matter," Phys. Lett. B **646**, 34 (2007) [hep-ph/0610249].

[5] N. Maru, N. Okada and S. Okada, "$SU(2)_L$ doublet vector dark matter from gauge-Higgs unification," Phys. Rev. D **98**, no. 7, 075021 (2018) [arXiv:1803.01274 [hep-ph]].

[6] A. Belyaev, G. Cacciapaglia, J. Mckay, D. Marin and A. R. Zerwekh, "Minimal Spin-one Isotriplet Dark Matter," Phys. Rev. D **99**, no. 11, 115003 (2019) [arXiv:1808.10464 [hep-ph]].

[7] G. Servant and T. M. P. Tait, "Is the lightest Kaluza-Klein particle a viable dark matter candidate?," Nucl. Phys. B **650**, 391 (2003) [hep-ph/0206071].

[8] S. Kanemura, S. Matsumoto, T. Nabeshima and N. Okada, "Can WIMP Dark Matter overcome the Nightmare Scenario?," Phys. Rev. D **82**, 055026 (2010) [arXiv:1005.5651 [hep-ph]].

[9] O. Lebedev, H. M. Lee and Y. Mambrini, "Vector Higgs-portal dark matter and the invisible Higgs," Phys. Lett. B **707**, 570 (2012) [arXiv:1111.4482 [hep-ph]].

[10] T. Abe, M. Kakizaki, S. Matsumoto and O. Seto, "Vector WIMP Miracle," Phys. Lett. B **713**, 211 (2012) [arXiv:1202.5902 [hep-ph]].

[11] Y. Farzan and A. R. Akbarieh, "VDM: A model for Vector Dark Matter," JCAP **1210**, 026 (2012) [arXiv:1207.4272 [hep-ph]].

[12] S. Baek, P. Ko, W. I. Park and E. Senaha, "Higgs Portal Vector Dark Matter : Revisited," JHEP **1305**, 036 (2013) [arXiv:1212.2131 [hep-ph]].

[13] J. M. Hyde, A. J. Long and T. Vachaspati, "Dark Strings and their Couplings to the Standard Model," Phys. Rev. D **89**, 065031 (2014) [arXiv:1312.4573 [hep-ph]].

[14] P. Ko, W. I. Park and Y. Tang, "Higgs portal vector dark matter for GeV scale γ-ray excess from galactic center," JCAP **1409**, 013 (2014) [arXiv:1404.5257 [hep-ph]].

[15] S. Baek, P. Ko and W. I. Park, "Invisible Higgs Decay Width vs. Dark Matter Direct Detection Cross Section in Higgs Portal Dark Matter Models," Phys. Rev. D **90**, no. 5, 055014 (2014) [arXiv:1405.3530 [hep-ph]].

[16] J. H. Yu, "Vector Fermion-Portal Dark Matter: Direct Detection and Galactic Center Gamma-Ray Excess," Phys. Rev. D **90**, no. 9, 095010 (2014) [arXiv:1409.3227 [hep-ph]].

[17] C. R. Chen, Y. K. Chu and H. C. Tsai, "An Elusive Vector Dark Matter," Phys. Lett. B **741**, 205 (2015) [arXiv:1410.0918 [hep-ph]].

[18] T. Hambye, "Hidden vector dark matter," JHEP **0901**, 028 (2009) [arXiv:0811.0172 [hep-ph]].

[19] H. Zhang, C. S. Li, Q. H. Cao and Z. Li, "A Dark Matter Model with Non-Abelian Gauge Symmetry," Phys. Rev. D **82**, 075003 (2010) [arXiv:0910.2831 [hep-ph]].

[20] J. L. Diaz-Cruz and E. Ma, "Neutral SU(2) Gauge Extension of the Standard Model and a Vector-Boson Dark-Matter Candidate," Phys. Lett. B **695**, 264 (2011) [arXiv:1007.2631 [hep-ph]].

[21] S. Bhattacharya, J. L. Diaz-Cruz, E. Ma and D. Wegman, "Dark Vector-Gauge-Boson Model," Phys. Rev. D **85**, 055008 (2012) [arXiv:1107.2093 [hep-ph]].

[22] T. Hambye and A. Strumia, "Dynamical generation of the weak and Dark Matter scale," Phys. Rev. D **88**, 055022 (2013) [arXiv:1306.2329 [hep-ph]].

[23] H. Davoudiasl and I. M. Lewis, "Dark Matter from Hidden Forces," Phys. Rev. D **89**, no. 5, 055026 (2014) [arXiv:1309.6640 [hep-ph]].

[24] S. Baek, P. Ko and W. I. Park, "Hidden sector monopole, vector dark matter and dark radiation with Higgs portal," JCAP **1410**, 067 (2014) [arXiv:1311.1035 [hep-ph]].

[25] V. V. Khoze and G. Ro, "Dark matter monopoles, vectors and photons," JHEP **1410**, 061 (2014) [arXiv:1406.2291 [hep-ph]].

[26] S. Fraser, E. Ma and M. Zakeri, "$SU(2)_N$ model of vector dark matter with a leptonic connection," Int. J. Mod. Phys. A **30**, no. 03, 1550018 (2015) [arXiv:1409.1162 [hep-ph]].

[27] A. Karam and K. Tamvakis, "Dark matter and neutrino masses from a scale-invariant multi-Higgs portal," Phys. Rev. D **92**, no. 7, 075010 (2015) [arXiv:1508.03031 [hep-ph]].

[28] J. L. Diaz-Cruz and E. Ma, "Neutral SU(2) Gauge Extension of the Standard Model and a Vector-Boson Dark-Matter Candidate," Phys. Lett. B **695**, 264 (2011) [arXiv:1007.2631 [hep-ph]].

[29] B. Barman, S. Bhattacharya, S. K. Patra and J. Chakrabortty, "Non-Abelian Vector Boson Dark Matter, its Unified Route and signatures at the LHC," JCAP **1712**, 021 (2017) [arXiv:1704.04945 [hep-ph]].

[30] B. Barman, S. Bhattacharya and M. Zakeri, "Multipartite Dark Matter in $SU(2)_N$ extension of Standard Model and signatures at the LHC," JCAP **1809**, 023 (2018) [arXiv:1806.01129 [hep-ph]].

[31] B. Barman, S. Bhattacharya and M. Zakeri, "Non-Abelian Vector Boson as FIMP Dark Matter," JCAP **2002**, 029 (2020) [arXiv:1905.07236 [hep-ph]].

[32] P.A. Zyla *et al.* [Particle Data Group], "Review of Particle Physics," PTEP **2020**, no.8, 083C01 (2020)

[33] N. Cabibbo, "Unitary Symmetry and Leptonic Decays," Phys. Rev. Lett. **10**, 531-533 (1963)

[34] M. Kobayashi and T. Maskawa, "CP Violation in the Renormalizable Theory of Weak Interaction," Prog. Theor. Phys. **49**, 652-657 (1973)

[35] C. Abel *et al.* [nEDM], "Measurement of the permanent electric dipole moment of the neutron," Phys. Rev. Lett. **124**, no.8, 081803 (2020) [arXiv:2001.11966 [hep-ex]].

[36] F. Capozzi, E. Di Valentino, E. Lisi, A. Marrone, A. Melchiorri and A. Palazzo, "Global constraints on absolute neutrino masses and their ordering," Phys. Rev. D **95**, no.9, 096014 (2017) [arXiv:2003.08511 [hep-ph]].

[37] E. Corbelli and P. Salucci, "The Extended Rotation Curve and the Dark Matter Halo of M33," Mon. Not. Roy. Astron. Soc. **311** (2000), 441-447 [arXiv:astro-ph/9909252 [astro-ph]].

[38] V. C. Rubin, W. K. Ford, Jr., N. Thonnard and D. Burstein, "Rotational properties of 23 SB galaxies," Astrophys. J. **261** (1982), 439

[39] A. Borriello and P. Salucci, "The Dark matter distribution in disk galaxies," Mon. Not. Roy. Astron. Soc. **323** (2001), 285 [arXiv:astro-ph/0001082 [astro-ph]].

[40] M. Persic, P. Salucci and F. Stel, "The Universal rotation curve of spiral galaxies: 1. The Dark matter connection," Mon. Not. Roy. Astron. Soc. **281** (1996), 27 [arXiv:astro-ph/9506004 [astro-ph]].

[41] P. Salucci, A. Lapi, C. Tonini, G. Gentile, I. Yegorova and U. Klein, "The Universal Rotation Curve of Spiral Galaxies. 2. The Dark Matter Distribution out to the Virial Radius," Mon. Not. Roy. Astron. Soc. **378** (2007), 41-47 [arXiv:astro-ph/0703115 [astro-ph]].

[42] P. J. E. Peebles, "Large scale background temperature and mass fluctuations due to scale invariant primeval perturbations," Astrophys. J. Lett. **263** (1982), L1-L5

[43] M. Davis, G. Efstathiou, C. S. Frenk and S. D. M. White, "The Evolution of Large Scale Structure in a Universe Dominated by Cold Dark Matter," Astrophys. J. **292** (1985), 371-394

[44] A. Jenkins *et al.* [VIRGO Consortium], "Evolution of structure in cold dark matter universes," Astrophys. J. **499** (1998), 20 [arXiv:astro-ph/9709010 [astro-ph]].

[45] D. Clowe, M. Bradac, A. H. Gonzalez, M. Markevitch, S. W. Randall, C. Jones and D. Zaritsky, "A direct empirical proof of the existence of dark matter," Astrophys. J. Lett. **648** (2006), L109-L113 [arXiv:astro-ph/0608407 [astro-ph]].

[46] K. Kadota, T. Sekiguchi and H. Tashiro, "A new constraint on millicharged dark matter from galaxy clusters," [arXiv:1602.04009 [astro-ph.CO]].

[47] K. Griest and D. Seckel, "Three exceptions in the calculation of relic abundances," Phys. Rev. D **43**, 3191-3203 (1991)

[48] K. Saikawa and S. Shirai, "Precise WIMP Dark Matter Abundance and Standard Model Thermodynamics," JCAP **08**, 011 (2020) [arXiv:2005.03544 [hep-ph]].

[49] D. S. Akerib *et al.* [LUX-ZEPLIN], "Projected WIMP sensitivity of the LUX-ZEPLIN dark matter experiment," Phys. Rev. D **101**, no.5, 052002 (2020) [arXiv:1802.06039 [astro-ph.IM]].

[50] H. Zhang *et al.* [PandaX], "Dark matter direct search sensitivity of the PandaX-4T experiment," Sci. China Phys. Mech. Astron. **62**, no.3, 31011 (2019) [arXiv:1806.02229 [physics.ins-det]].

[51] C. E. Aalseth *et al.* [DarkSide-20k], "DarkSide-20k: A 20 tonne two-phase LAr TPC for direct dark matter detection at LNGS," Eur. Phys. J. Plus **133**, 131 (2018) [arXiv:1707.08145 [physics.ins-det]].

[52] J. I. Read, "The Local Dark Matter Density," J. Phys. G **41**, 063101 (2014) [arXiv:1404.1938 [astro-ph.GA]].

[53] J. Bovy, C. Allende Prieto, T. C. Beers, D. Bizyaev, L. N. da Costa, K. Cunha, G. L. Ebelke, D. J. Eisenstein, P. M. Frinchaboy and A. E. G. Perez, *et al.* "The Milky Way's circular velocity curve between 4 and 14 kpc from APOGEE data," Astrophys. J. **759**, 131 (2012) [arXiv:1209.0759 [astro-ph.GA]].

[54] N. Bozorgnia, F. Calore, M. Schaller, M. Lovell, G. Bertone, C. S. Frenk, R. A. Crain, J. F. Navarro, J. Schaye and T. Theuns, "Simulated Milky Way analogues: implications for dark matter direct searches," JCAP **05**, 024 (2016) [arXiv:1601.04707 [astro-ph.CO]].

[55] J. Hisano, K. Ishiwata, N. Nagata and M. Yamanaka, "Direct Detection of Vector Dark Matter," Prog. Theor. Phys. **126**, 435-456 (2011) [arXiv:1012.5455 [hep-ph]].

[56] J. F. Navarro, C. S. Frenk and S. D. M. White, "The Structure of cold dark matter halos," Astrophys. J. **462**, 563-575 (1996) [arXiv:astro-ph/9508025 [astro-ph]].

[57] J. Einasto, Trudy Astrofizicheskogo Instituta Alma-Ata **5**, 87-100 (1965)

[58] R. Catena and P. Ullio, "A novel determination of the local dark matter density," JCAP **08**, 004 (2010) [arXiv:0907.0018 [astro-ph.CO]].

[59] B. Fuchs, C. Dettbarn, H. W. Rix, T. C. Beers, D. Bizyaev, H. Brewington, H. Jahreiss, R. Klement, E. Malanushenko and V. Malanushenko, *et al.* "The kinematics of late type stars in the solar cylinder studied with SDSS data," Astron. J. **137**, 4149-4159 (2009) [arXiv:0902.2324 [astro-ph.GA]].

[60] R. Abuter *et al.* [GRAVITY], "Detection of the gravitational redshift in the orbit of the star S2 near the Galactic centre massive black hole," Astron. Astrophys. **615**, L15 (2018) [arXiv:1807.09409 [astro-ph.GA]].

[61] H. Abdallah *et al.* [HESS], "Search for γ-Ray Line Signals from Dark Matter Annihilations in the Inner Galactic Halo from 10 Years of Observations with H.E.S.S.," Phys. Rev. Lett. **120**, no.20, 201101 (2018) [arXiv:1805.05741 [astro-ph.HE]].

[62] M. Ackermann *et al.* [Fermi-LAT], "Updated search for spectral lines from Galactic dark matter interactions with pass 8 data from the Fermi Large Area Telescope," Phys. Rev. D **91**, no.12, 122002 (2015) [arXiv:1506.00013 [astro-ph.HE]].

[63] J. F. Navarro, A. Ludlow, V. Springel, J. Wang, M. Vogelsberger, S. D. M. White, A. Jenkins, C. S. Frenk and A. Helmi, "The Diversity and Similarity of Cold Dark Matter Halos," Mon. Not. Roy. Astron. Soc. **402**, 21 (2010) [arXiv:0810.1522 [astro-ph]].

[64] A. Burkert, "The Structure of dark matter halos in dwarf galaxies," IAU Symp. **171**, 175 (1996) [arXiv:astro-ph/9504041 [astro-ph]].

[65] P. Salucci and A. Borriello, "Cold dark matter halos must burn," [arXiv:astro-ph/0106251 [astro-ph]].

[66] G. Gilmore, M. I. Wilkinson, R. F. G. Wyse, J. T. Kleyna, A. Koch, N. W. Evans and E. K. Grebel, "The Observed properties of Dark Matter on small spatial scales," Astrophys. J. **663**, 948-959 (2007) [arXiv:astro-ph/0703308 [astro-ph]].

[67] S. H. Oh, W. J. G. de Blok, F. Walter, E. Brinks and R. C. Kennicutt, Jr, "High-resolution dark matter density profiles of THINGS dwarf galaxies: Correcting for non-circular motions," Astron. J. **136**, 2761 (2008) [arXiv:0810.2119 [astro-ph]].

[68] W. J. G. de Blok, "The Core-Cusp Problem," Adv. Astron. **2010**, 789293 (2010) [arXiv:0910.3538 [astro-ph.CO]].

[69] V. Silveira and A. Zee, "SCALAR PHANTOMS," Phys. Lett. B **161**, 136-140 (1985)

[70] J. McDonald, "Gauge singlet scalars as cold dark matter," Phys. Rev. D **50**, 3637-3649 (1994) [arXiv:hep-ph/0702143 [hep-ph]].

[71] C. P. Burgess, M. Pospelov and T. ter Veldhuis, "The Minimal model of nonbaryonic dark matter: A Singlet scalar," Nucl. Phys. B **619**, 709-728 (2001) [arXiv:hep-ph/0011335 [hep-ph]].

[72] E. Aprile *et al.* [XENON Collaboration], "Physics reach of the XENON1T dark matter experiment," JCAP **1604**, 027 (2016) [arXiv:1512.07501 [physics.ins-det]].

[73] M. Escudero, A. Berlin, D. Hooper and M. X. Lin, "Toward (Finally!) Ruling Out Z and Higgs Mediated Dark Matter Models," JCAP **12**, 029 (2016) [arXiv:1609.09079 [hep-ph]].

[74] G. Arcadi, M. Dutra, P. Ghosh, M. Lindner, Y. Mambrini, M. Pierre, S. Profumo and F. S. Queiroz, "The waning of the WIMP? A review of models, searches, and constraints," Eur. Phys. J. C **78**, no.3, 203 (2018) [arXiv:1703.07364 [hep-ph]].

[75] J. Hisano, K. Ishiwata and N. Nagata, "QCD Effects on Direct Detection of Wino Dark Matter," JHEP **1506**, 097 (2015) [arXiv:1504.00915 [hep-ph]].

[76] M. Farina, D. Pappadopulo and A. Strumia, "A modified naturalness principle and its experimental tests," JHEP **08**, 022 (2013) [arXiv:1303.7244 [hep-ph]].

[77] N. Nagata and S. Shirai, "Electroweakly-Interacting Dirac Dark Matter," Phys. Rev. D **91**, no.5, 055035 (2015) [arXiv:1411.0752 [hep-ph]].

[78] T. Flacke, D. W. Kang, K. Kong, G. Mohlabeng and S. C. Park, "Electroweak Kaluza-Klein Dark Matter," JHEP **04**, 041 (2017) [arXiv:1702.02949 [hep-ph]].

[79] E. Ma, "$[SU(2)]^3$ dark matter," Phys. Lett. B **780**, 533 (2018) [arXiv:1712.08994 [hep-ph]].

[80] C. T. Hill, S. Pokorski and J. Wang, "Gauge Invariant Effective Lagrangian for Kaluza-Klein Modes," Phys. Rev. D **64**, 105005 (2001) [hep-th/0104035].

[81] N. Arkani-Hamed, A. G. Cohen and H. Georgi, "(De)constructing dimensions," Phys. Rev. Lett. **86**, 4757 (2001) [hep-th/0104005].

[82] H. Georgi, "A Tool Kit for Builders of Composite Models," Nucl. Phys. B **266**, 274 (1986).

[83] K. Hally, H. E. Logan and T. Pilkington, "Constraints on large scalar multiplets from perturbative unitarity," Phys. Rev. D **85**, 095017 (2012) [arXiv:1202.5073 [hep-ph]].

[84] G. Aad *et al.* [ATLAS Collaboration], "Search for a heavy charged boson in events with a charged lepton and missing transverse momentum from *pp* collisions at $\sqrt{s} = 13$ TeV with the ATLAS detector," Phys. Rev. D **100**, no. 5, 052013 (2019) [arXiv:1906.05609 [hep-ex]].

[85] A. M. Sirunyan *et al.* [CMS Collaboration], "Search for high-mass resonances in final states with a lepton and missing transverse momentum at $\sqrt{s} = 13$ TeV," JHEP **1806**, 128 (2018) [arXiv:1803.11133 [hep-ex]].

[86] The ATLAS collaboration [ATLAS Collaboration], "Prospects for searches for heavy Z' and W' bosons in fermionic final states with the ATLAS experiment at the HL-LHC," ATL-PHYS-PUB-2018-044.

[87] R. Barbieri, A. Pomarol, R. Rattazzi and A. Strumia, "Electroweak symmetry breaking after LEP-1 and LEP-2," Nucl. Phys. B **703**, 127 (2004) [hep-ph/0405040].

[88] G. Aad *et al.* [ATLAS Collaboration], "Combined measurements of Higgs boson production and decay using up to 80 fb^{-1} of proton-proton collision data at $\sqrt{s} =$ 13 TeV collected with the ATLAS experiment," Phys. Rev. D **101**, no. 1, 012002 (2020) [arXiv:1909.02845 [hep-ex]].

[89] T. Hahn and M. Perez-Victoria, "Automatized one loop calculations in four-dimensions and D-dimensions," Comput. Phys. Commun. **118**, 153 (1999) [hep-ph/9807565].

[90] M. Cirelli, N. Fornengo and A. Strumia, "Minimal dark matter," Nucl. Phys. B **753**, 178 (2006) [hep-ph/0512090].

[91] M. Aaboud *et al.* [ATLAS Collaboration], "Search for long-lived charginos based on a disappearing-track signature in pp collisions at $\sqrt{s} = 13$ TeV with the ATLAS detector," JHEP **1806**, 022 (2018) [arXiv:1712.02118 [hep-ex]].

[92] G. Bélanger, F. Boudjema, A. Goudelis, A. Pukhov and B. Zaldivar, "micrOMEGAs5.0 : Freeze-in," Comput. Phys. Commun. **231**, 173 (2018) [arXiv:1801.03509 [hep-ph]].

[93] J. Hisano, S. Matsumoto, M. M. Nojiri and O. Saito, "Direct detection of the Wino and Higgsino-like neutralino dark matters at one-loop level," Phys. Rev. D **71**, 015007 (2005) [hep-ph/0407168].

[94] J. Hisano, K. Ishiwata and N. Nagata, "A complete calculation for direct detection of Wino dark matter," Phys. Lett. B **690**, 311 (2010) [arXiv:1004.4090 [hep-ph]].

[95] A. Alloul, N. D. Christensen, C. Degrande, C. Duhr and B. Fuks, "FeynRules 2.0 - A complete toolbox for tree-level phenomenology," Comput. Phys. Commun. **185**, 2250 (2014) [arXiv:1310.1921 [hep-ph]].

[96] J. Hisano, S. Matsumoto and M. M. Nojiri, "Unitarity and higher order corrections in neutralino dark matter annihilation into two photons," Phys. Rev. D **67**, 075014 (2003) [hep-ph/0212022].

[97] J. Hisano, S. Matsumoto and M. M. Nojiri, "Explosive dark matter annihilation," Phys. Rev. Lett. **92**, 031303 (2004) [hep-ph/0307216].

[98] J. Hisano, S. Matsumoto, M. M. Nojiri and O. Saito, "Non-perturbative effect on dark matter annihilation and gamma ray signature from galactic center," Phys. Rev. D **71**, 063528 (2005) [hep-ph/0412403].

[99] N. Arkani-Hamed, D. P. Finkbeiner, T. R. Slatyer and N. Weiner, "A Theory of Dark Matter," Phys. Rev. D **79**, 015014 (2009) [arXiv:0810.0713 [hep-ph]].

[100] K. Blum, R. Sato and T. R. Slatyer, "Self-consistent Calculation of the Sommerfeld Enhancement," JCAP **1606**, 021 (2016) [arXiv:1603.01383 [hep-ph]].

[101] L. Rinchiuso, O. Macias, E. Moulin, N. L. Rodd and T. R. Slatyer, "Prospects for Heavy WIMP Dark Matter with CTA: the Wino and Higgsino," [arXiv:2008.00692 [astro-ph.HE]].

[102] P. Mollitor, E. Nezri and R. Teyssier, "Baryonic and dark matter distribution in cosmological simulations of spiral galaxies," Mon. Not. Roy. Astron. Soc. **447**, no.2, 1353-1369 (2015) [arXiv:1405.4318 [astro-ph.GA]].